Dissertation

submitted to the

Combined Faculty of Natural Sciences and Mathematics

of the Ruperto Carola University Heidelberg, Germany

for the degree of

Doctor of Natural Sciences

Presented by

M. Sc. Tobias Dahm

born in Landshut

Oral examination: 20.03.2020

Sequential transmigration of polymorphonuclear cells and naïve CD3+ T lymphocytes across the blood-cerebrospinal-fluid barrier *in vitro* following infection with Echovirus 30

Referees:

Prof. Dr. med. Hans-Georg Kräusslich

Prof. Dr. med. Horst Schroten

This thesis is dedicated to

My family

TABLE OF CONTENTS

LIST OF TABLES & FIGURES

Zusammenfassung

Trotz signifikanter Fortschritte beim Verständnis der Pathogenese der viralen Meningitis nimmt die Krankheitslast der Infektion mit Non-Polio Enteroviren weltweit zu. Die vorliegende Dissertation möchte dazu beitragen, dieses Verständnis weiter zu vertiefen, um vielleicht zukünftig eine erfolgreiche Eindämmung der Krankheit zu ermöglichen.

Die virale Meningitis kann durch die Infektion mit Echovirus (E) 30 (E-30) nach Überwindung der Blut-Liquor Schranke verursacht werden. Als Folge der Infektion des Zentralnervensystems kommt es dann zur Neuroinflammation. Klinische Analysen deuteten auf eine Pleozytose im Liquor von zunächst überwiegend polymorphonukleären Granulozyten (PMN) in der frühen Phase der Infektion hin, gefolgt von mononukleären Zellen. Im Rahmen dieser Dissertation wurde ein humanes *in vitro* Modell der Blut-Liquor Schranke aus humanen Epithelzellen des Plexus choroideus benutzt, um die sequentielle Transmigration von polymorphonukleären Granulozyten und $CD3^+$ T-Lymphozyten nach einer Infektion mit E-30 Bastianni näher zu untersuchen. Die Versuchsergebnisse zeigten, dass die Migration von PMN durch humane Plexus choroideus Papillom (HIBCPP)-Zellen durch die Präsenz von $CD3^+$ T-Lymphozyten signifikant erhöht wird. Im Gegensatz dazu war die Zugabe von PMN nicht in der Lage, die Migration von T-Lymphozyten zu fördern. Die Infektion der Epithelzellen mit E-30 Bastianni führte außerdem zu einer Hochregulation von CXCL 3 und CXCL 11. Diese und auch weitere Chemokine wurden hauptsächlich auf der basolateralen HIBCPP-Zellseite sezerniert, wohingegen IL-7 vor allem apikal abgegeben wurde.

Im nächsten Schritt konnte durch die Verwendung dreier klinischer Ausbruchsstämme und dem prototypischen Stamm E-30 Bastianni eine stammabhängige Wirkung auf die epitheliale Zellbarrierefunktion und Morphologie der Zellen gezeigt werden. Die Stämme 13-759 und 14-397 hatten keine signifikante Auswirkung auf die Barriere-Integrität der HIBCPP Zellen. E-30 Bastianni und der Ausbruchstamm 13-311 verursachten eine signifikante Abnahme des transepithelialen elektrischen Widerstands der Epithelzellbarriere. Zugleich waren diese beiden Stämme die einzigen Varianten, die eine sichtbare Veränderung der Tight Junction-Proteine ZO1 und Occludin sowie des Adherence Junction-Proteins E-Cadherin verursachten. Trotz dieser disruptiven Auswirkungen auf die Morphologie der epithelialen Zellbarriere erfolgte die Migration von PMN und $CD3^+$ T-Lymphozyten sowohl über den trans- als auch

über den parazellulären Weg. Die Analyse mittels Elektronenmikroskopie und Immunfluoreszenz zeigte, dass beide Zelltypen sowohl trans- als auch parazellulär die epitheliale Zellbarriere überquerten. Weitere Analysen der genetischen Zusammensetzung identifizierten Unterschiede zwischen den Stämmen. Diese Unterschiede konnten aber nicht mit den spezifischen Unterschieden, die in den Infektionsexperimenten beobachtet wurden, in Verbindung gebracht werden.

Insgesamt zeigten wir eine erhöhte PMN-Migration in der Anwesenheit von $CD3^+$ T-Lymphozyten über die infizierte Epithelzellschicht und einem spezifisches Chemokin-Freisetzungsmuster. Weiterhin konnten wir E-30-Stamm-spezifische Effekte auf die Integrität der menschlichen epithelialen Zellbarriere zeigen. Die Stämme verursachten morphologische Veränderungen an den junktionalen Proteinen, trotzdem erfolgte die Migration der Leukozyten sowohl trans- als auch parazellulär. Im Rahmen dieser Dissertation konnten E-30 stammspezifische Effekte auf die epithelialen Zellbarrieren festgestellt werden, die zum weiteren Verständnis der Immunzellen-Migration bei viraler Meningitis beitragen.

Summary

Despite significant advances in the understanding of the pathogenesis of viral meningitis, infection with non-polio enteroviruses (NPEV) has an increasing disease burden worldwide. This dissertation hopes to contribute to further deepening the understanding of the disease for a successful containment of the disease in the future.

Viral meningitis can be caused by infection with Echovirus (E) 30 (E-30) of the central nervous system (CNS) at the level of the blood-cerebrospinal fluid barrier (BCSFB). This infection causes neuroinflammation resulting in immune cell migration. Clinical analysis suggests that in the cerebrospinal fluid a pleocytosis of predominantly polymorphonuclear granulocytes (PMN) occurs in the early phase of infection, followed by a monocuclear cell population. Within the scope of this thesis we analysed the sequential transmigration of PMN and $CD3^+$ T-lymphocytes across an E-30 Bastianni- infected human BCSFB *in vitro*. The results show that migration of PMN through human choroid plexus papilloma (HIBCPP) cells was significantly increased when $CD3^+$ T-lymphocytes were present. In contrast, PMN were not able to promote T-lymphocyte migration. Chemokine expression was affected by E-30 infection with an upregulation of CXCL 3 and CXCL 11. The secretion of these and other chemokines was mainly directed towards the basolateral HIBCPP cell side, except for IL-7 where apical secretion was dominant.

In the next step we were utilizing three clinical outbreak strains and the prototypic E-30 Bastianni strain and we were able to show strain dependent effect on the epithelial cell barrier function and morphology. The strains 13-759 and 14-397 did not cause significant effects on the barrier integrity of the HIBCPP cells. E-30 Bastianni and outbreak strain 13-311 caused significant decrease in the transepithelial electrical resistance of the epithelial cell barrier. These two strains were the only variants causing visible alteration of the tight junction proteins ZO1 and Occludin and the adherence junction protein E-cadherin. Despite these disruptive effects on the morphology of the epithelial cell barrier, migration of PMN and $CD3^+$ T lymphocytes occurred both via the trans- and paracellular route. Analysis applying electron microscopy and immunofluorescence detected both cell types during and just following their migration across the epithelial cell barrier moving both between and through the HIBCPP cells. Further analysis of the genetic composition identified differences

between the strains, but these could not be linked to the differences observed during the infection experiments.

Overall, we showed enhanced PMN migration across the infected epithelial cell layer in the presence of $CD3^+$ T-lymphocytes and an intriguing chemokine release pattern. Further, we were able to show E-30 strain specific effects on human epithelial cell barrier integrity. The strains caused particular morphological changes to the junctional proteins, however, migration of leukocytes occurred both trans and paracellularly. We were able to identify E-30 strain-specific effects on the epithelial cell barrier and contribute to the understanding of immune cell migration in viral meningitis.

1. Introduction

1.1. Physiological barriers of the brain

The human brain is surrounded by protective meninges tissue, which are composed of three major layers: the dura mater, the arachnoid layer and the pia mater (Fig. 1). Their main junctions include protection of the brain and spinal cord from mechanical injury or shock, creating a space for cerebrospinal fluid (CSF) flow and to allow blood flow to the skull and hemispheres. The outermost layer, the dura mater, is also the sturdiest layer and is composed of two major compartments. A thick and tough layer surrounding the skull is called the endosteal layer. This endosteal layer is nearly completely covered in the meningeal layer. The connection is only interrupted in some parts of the hemisphere, the falx cerebri and the tentorium cerebelli, where in the freed space sinuses may form (Fig. 2). The middle layer, arachnoid layer, consists of tight interconnected collagen strands able to soften possible physical shock. The arachnoid can be separated into three layers, the arachnoid membrane, the arachnoid trabeculae and the subarachnoid space. The subarachnoid space found between the arachnoid and the pia mater allows circulation of CSF. As the arachnoid covers the whole brain, it is often considered as one of the major brain barriers [1]. The other major barriers are the blood-brain barrier (BBB) and the blood-cerebrospinal fluid barrier (BCSFB).

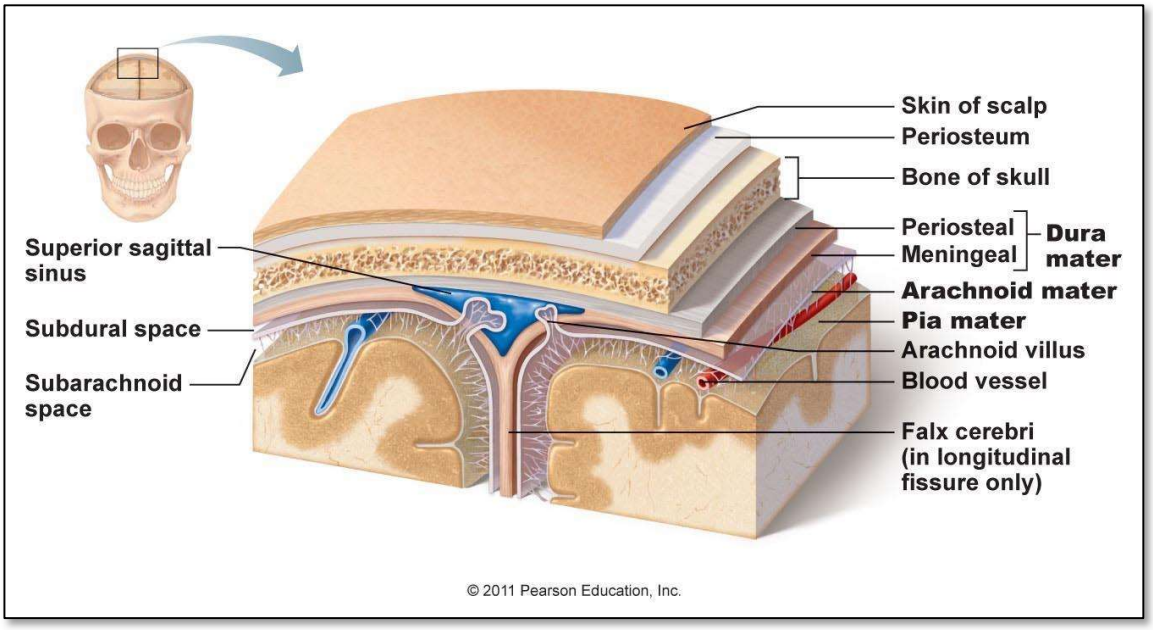

Figure 1. Representation of the human meninges tissue [2]. Showing the different layers and their order around the human brain from the outermost to the innermost.

Most of our knowledge on the physiological barriers of the brain has been built up on experimental studies carried out in the early 20s century by Paul Ehrlich and his colleague Edwin Goldman [3, 4]. They have been demonstrating that a selective barrier surrounding the nervous system hindered dye, which otherwise stained all remaining organs, from moving from the vascular circulation in the spinal cord or brain. In accordance, when the dye was introduced into the cerebrospinal fluid, it was not detected elsewhere in the organism apart from the brain.

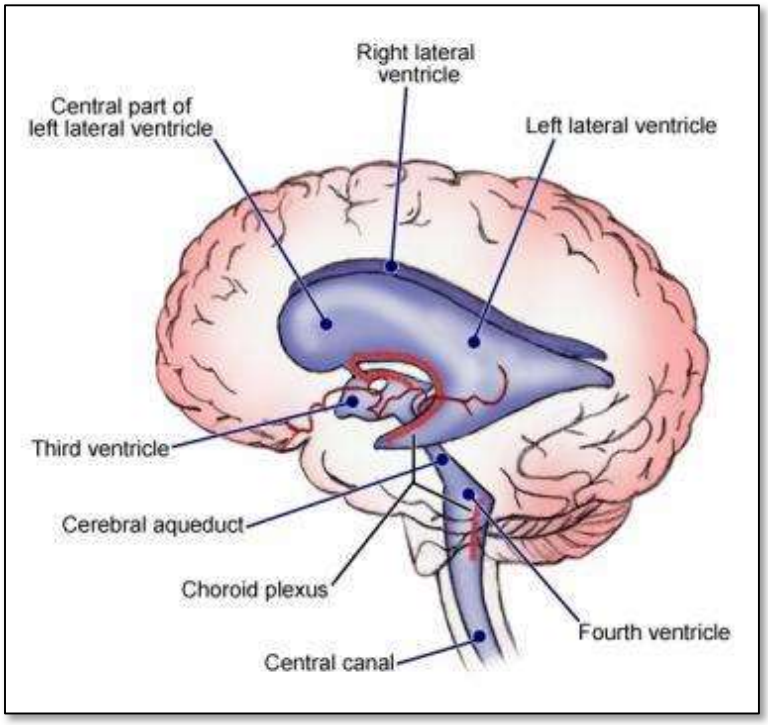

Figure 2. Human Brain with focus on choroid plexus [5]. Sagittal plane to visualize the build-up of the human brain with a focus on the four ventricles and choroid plexus. The ventricles and subarachnoid space are filled with CSF produced by the choroid plexus

These findings were the foundation for the discovery of the BBB, which in combination with further dye injections also led to the identification of the other major brain-barriers such as the blood-cerebrospinal fluid barrier (BCSFB). The BBB acts as a division between the interstitial fluid of the parenchyma and the blood and limits the diffusion of water-soluble compounds from the brain tissue to the blood [6]. Its large surface area allows selective movement of materials between the vascular system and the brain. The exchange of materials at the BBB is largely controlled by endothelial cells of the brain capillaries, which form a tightly connected network with other cells such as pericytes and astrocytes. The endothelial cells form a basal membrane, in which pericytes are found embedded in the astrocyte end feet. The glial cells have a crucial role during formation and maintenance of junctional proteins, however no substantially involvement in the barrier function has been discovered. The tight and highly selective barrier is formed between the endothelial cells of the mammalian brain. The polar cells form protein connections at both the basolateral and the luminal side and in combination with specialised transporters create a diffusion barrier.

The cellular composition and build-up of the BBB allows a steady and uninterrupted supply of oxygen and other necessary compounds, while hindering pathogen entry and keeping a tight control on movement of substances across the membrane. The BCSFB has similar characteristics in terms of build-up and function to the BBB and will be discussed in detail in the next section.

1.1.1. The blood-cerebrospinal fluid barrier

The BCSFB mainly consists of the choroid plexus (CP). The CP is a strongly vascularized tissue with a sheet like structure located in the cerebral ventricles of the brain [7] [8]. There are a total of four CPs, which are spread across the lateral ventricles and the 3rd and 4th ventricle (Fig. 2). At the border between the ventricles and the CP, the ependymal cells undergo a transformation into specialized CP epithelial cells [7].

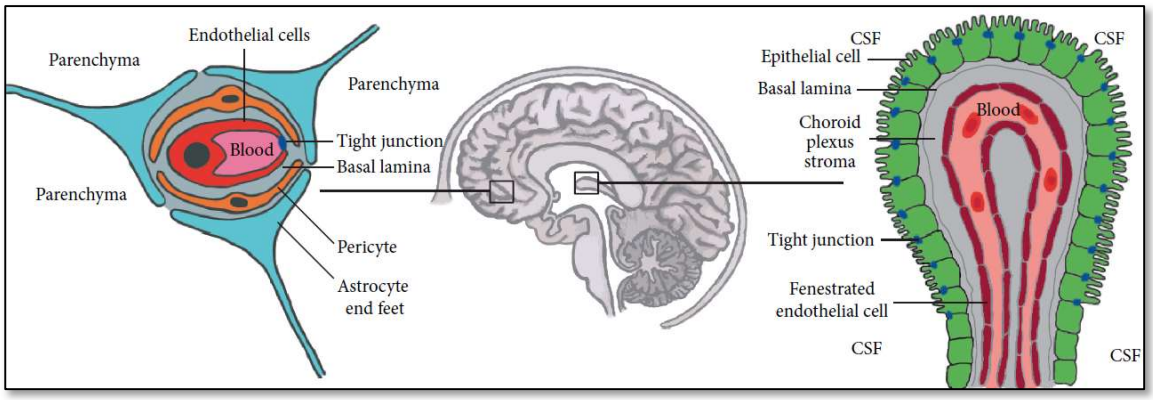

Figure 3. Brain barriers. (On the left) Representation of the BBB. This barrier is made up of pericytes, astrocytes and capillary endothelial cells and creates a fence-like structure between the cerebral blood vessels and the brain parenchyma. The main role in creation of the barrier function and limitation to material exchange is carried out by the endothelial cells which are connected through luminal tight junctions. (Centre) Midsagittal plane of a human brain. (On the right) Representation of the BCSFB which consists of polar choroid plexus epithelial cells tightly connected through tight junctions at the apical cell side. The barrier lays between the fenestrated blood vessels of the choroid plexus and the CSF. Modified from Dahm et al., 2016 [9].

The BCSFB consists of two major cell types, the endothelial and the epithelial cells. In contrast to the BBB, where the endothelial cells form the basis for a tight and selective barrier, at the CP the endothelial cells are fenestrated, permeable to blood components and are similar to the peripheral endothelium (Fig.3) [10]. The endothelial cells of the BBB are firmly connected through elaborate interconnecting tight junctions which regulate passage of molecules and cells into the CNS. This highly developed system, in combination with low

pinocytotic activity and no fenestration, allows precise control on transport of toxic waste materials out and useful nutrients into the CNS.

At the level of the BCSFB the polar epithelial cells are tightly connected through TJs and are arranged in numerous microvilli protruding into the cerebrospinal fluid space. The polar cells have specialized transporters oriented either to the basolateral or the luminal side; in combination with the cell-to-cell connections they form a barrier with a low pinocytotic activity [8, 11, 12]. Additional to the barrier function of the BSCFB, the CP is also the site of cerebrospinal fluid (CSF) production. The actively secreted liquid has a consistent composition and submerges the brain and spinal cord, which protects the sensitive organs from physical shock [7]. To maintain a homogenous environment in terms of ionic, nutritional, metabolic and hormonal balance, the specialized transporters carry (micro)nutrients, ions and hormones from the blood into the CSF; on the other hand they expel toxic or harmful material back into the blood [7, 8, 12-14]. The homogenous environment is especially important for the functionality of nerve cells [15].

1.1.2. Structure and function of junction proteins

The barrier function of the brain barriers is mainly dependent on the functionality and integrity of the cell-to-cell contacts. These contacts, the so-called tight and adherens junctions, are made of junctional proteins situated along the apical and basolateral cell compartments. When intact, these multifunctional protein complexes connect neighbouring cells tightly, which hinders paracellular diffusion and ion flux. This is evident due to high electrical resistance.

The Tight Junctions (TJ) at the apical cell side are considered to have two major functions: to act as a “gate”, forming a barrier to ions, water, immune cells and other soluble compounds; but also to act as a “fence”, stopping interchanging of proteins between the apical and the basolateral cell side [16, 17]. Important members of the junctional proteins are the transmembrane proteins Occludin and the claudin family. To increase stability, these transmembrane proteins are connected to the actin cytoskeleton [18]. The movement of regulatory proteins such as the protein kinases and transcription factors is also controlled by ZO [19]. Also, the ZO family proteins are tightly connected to the actin filament through either carboxy or amino termini [20-22]. This recruitment of regulatory proteins allows

structural, regulatory and transmembrane proteins to be in close proximity of each other, which assists the progress of complex structure formation necessary to construct and maintain the barrier [19]. The paracellular permeability between barrier cells is in part controlled by the extracellular loops of Occludin which also interacts with claudins and other junctional proteins [16]. A range of claudins exists, however, only claudin 1, 2 and 11 are expressed alongside Occludin in the human epithelial cells of the CP [23, 24].

Further stability of the cell-to-cell connections is ensured through adherens junctions located at the basolateral cell compartments. To enforce the structural and mechanical cohesion, the actin filaments of two adjacent cells are connected and create a large actin network which further enhances the barrier integrity. These are also essential for the development of TJs [25]. Occludin and proteins from the claudin family, usually associated with TJs, may further enhance the stability through connections to the actin cytoskeleton and Adherense Junctions (AJ). These important connections are formed through the cytoplasmic adapter molecules, zonula occludens (ZO) 1, 2 and 3 [18]. The cadherins, transmembrane proteins which use their cytoplasmic domain to interact with cytoplasmic proteins such as α-actin or catenin, are important adherens junction proteins. The downregulation of the homophilic E-cadherin in epithelial cells has been associated with a decrease of barrier function [23].

1.1.3. Models to study CNS infections at the level of the brain barriers

The understanding of infection mechanisms at the level of the brain barriers has been an important field of research. Laboratory methods to study this phenomenon can be divided into *in vivo and in vitro* models. *In vitro* models exist as static or under flow conditions. The aim is to mimic *in vivo* conditions whilst maintaining the easier handling and broader range of possible manipulations. Therefore, one can choose either of the single culture models. For the BBB, these are often based on immortalized or primary brain microvascular endothelial cells; and for the BCSFB primary immortalized cells of the choroid plexus are used [9]. The involvement and cooperation of several different cell types at the BBB can be reproduced with the application of cocultures. Here often astrocytes or/and pericytes in combination with glia cells are grown together (Fig.4) [26, 27]. For example, HIV-associated encephalitis has been investigated in a coculture model combining brain endothelial cells and astrocytes.

The endothelial cells formed a monolayer with cell-to-cell connections and the astrocytes expressed the intermediate filament (IF) protein [28].

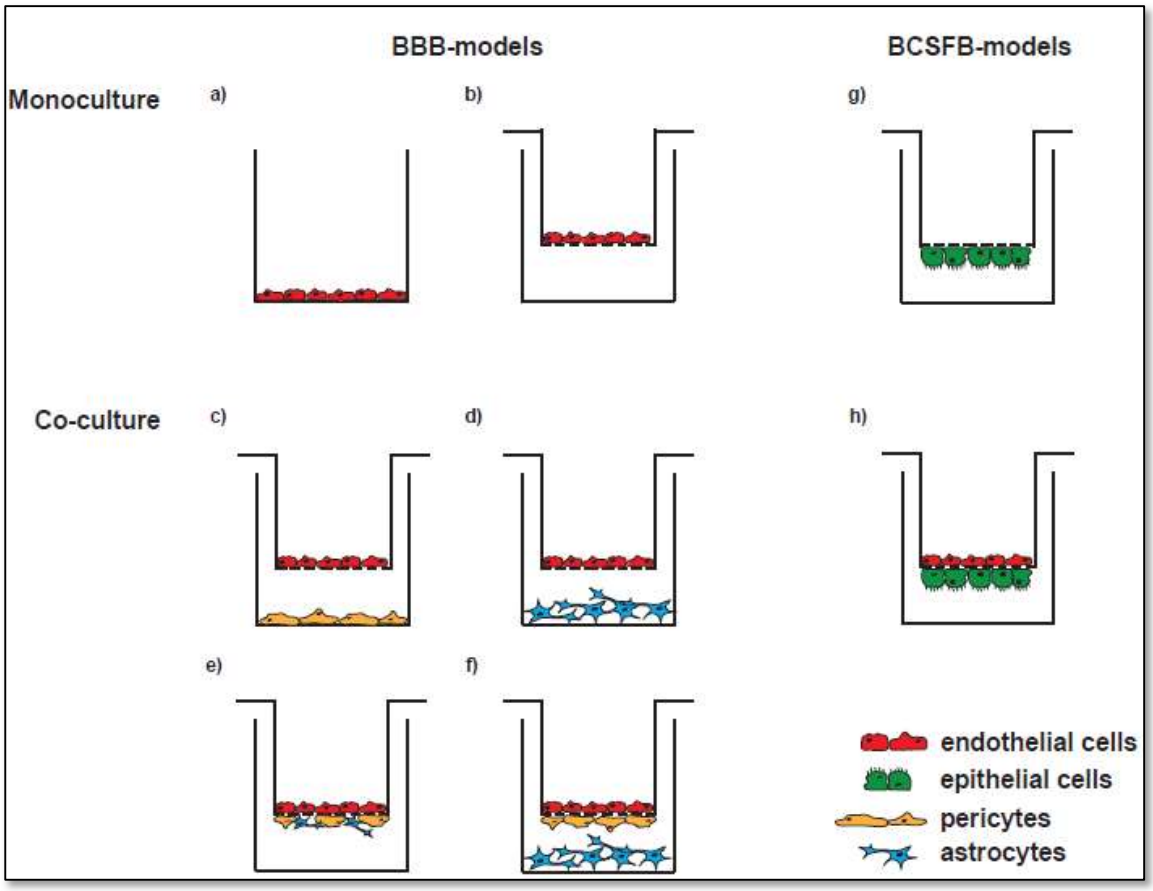

Figure 4. Different in vitro set ups that are used to study the BBB and BCSFB. For the BBB the different models are compiled around endothelia cells, whereas for the models of the BCSFB epithelial cells from the choroid plexus are used. Models may exist with either endothelial or epithelial cells. These are called monoculture *in vitro* models (a, b and g). Co-culture models with a combination of endothelial and epithelial cells (h), endothelial cells with astrocytes or pericytes (c and d). Or triple-culture models where endothelial cells are seeded with astrocytes and pericytes (e and f). There are also various ways of seeding the different cell types. A method where the cell types are in physical contact with one another (e, f and h) or with no contact (c and d). Here, the models in a and b are drawn with epithelial cells, however these may also exist with monocultures of endothelial cells. For further approach to in vivo conditions, chemical stimuli, immune cells or dyes may be added to filter insert and /or wells. Modified from Dahm et al., 2016 [9].

As other cell types have not shown much involvement at the level of the BCSFB, the study of *in vitro* is carried out in single culture models. Both immortalized and primary cells, mainly based on murine (Z310) or porcine donors (PCP-R), have been applied [29, 30]. Limitations occur when relating findings from these models back to human infection of the CNS [9]. Therefore, the application of an immortalized human choroid plexus papilloma cell line (HIBCPP) in recent years has advanced the understanding of infection at the level of the

BCSFB in humans [31, 32]. These models have been used to study the infection of the CNS at the level of the BCSFB by a range of bacterial and viral pathogens [33-37]. In particular, the involvement of the BCSFB during viral meningitis has been investigated thoroughly over recent years. Applying the human *in vitro* model of the BCSFB to investigate viral infection, Schneider et al. identified a time contingent enhanced expression of CXCL 1, CXCL 2 and CXCL 3; in addition, one could observe an overall increased migration of $CD3^+$ T lymphocytes and PMN across the barrier. This led to more tailored investigations into the cytokine and chemokine profile of the epithelial cells of the CNS during enteroviral infection. Predominant polar secretion towards the basolateral side of CXCL 3, CXCL 10, M-CSF, CCL 20 and IL-8 was recorded [9].

1.1.4. Viral meningitis

Despite improved available vaccinations and enhanced preventive measures, meningitis remains a disease associated with a high morbidity [38]. Viral meningitis is the infection and inflammation of the meninges through a viral pathogen and occurs with an incidence of 20-30 / 100.000 per year [39, 40]. Most of the viral meningitis cases recorded worldwide are due to an infection with non-polio enteroviruses (NPEV) and in total are more than 3 times more frequent than cases of bacterial meningitis. The infection is more likely to be found in young children and is transmitted via the oral-faecal route [41, 42]. In most cases the early phase of the infection shows low severity, however as the infection progresses the virus may cause severe infection to the CNS [43]. In temperate climates a seasonal dependency of infection rates rising in summer and autumn and falling in winter and spring has been recorded, whereas in tropical climate zones the infection rates remain steady throughout the year. The most common route of infection in humans is through the oral-faecal route whereas infection caused by pathogens entering the body through the airways is much less common. The early stages of the infection are often mild, however complications leading to severe damage to the CNS and possible death of the patients may occur [9, 44].

1.1.5. Epidemiology and seasonal outbreaks of echovirus 30

Worldwide enterovirus epidemics are in part caused by frequent genetic recombinations, which are also the reason for severe seasonal outbreaks [45-47]. When looking at infections of the CNS, particularly E 30 has been identified as a major cause of outbreaks recorded in Europe. However, in recent years a rise in outbreaks has also been detected and recorded in Asia and South America [48, 49]. Through genome sequencing it was possible to identify that this strain has been circulating in Europe since 2012 and is causing seasonal outbreaks.

1.1.6. Life Cycle of echovirus 30

The overall structure of Echovirus, in particular the formation of structural proteins, is closely linked to the host and mode of replication. The virus enters the human body through the nasopharynx, where viral replication starts. The replication cycle begins when the binding of the virus to a cell receptor causes internalization of the virus. Once inside the host cell, the virion releases the viral RNA genome which leads to its translation into a polyprotein. The viral protease further processes the polyprotein to cause the release of viral proteins. The resulting RNA molecules may repeat the replication cycle or be combined into viral capsid proteins. These newly formed viral particles may then be released upon cell lysis and cause further infection in the host [50, 51]. The infectious particles may spread further to the gastrointestinal tract or lymph nodes, where they replicate and cause infection. In the small intestine, the virus replicates and spreads via the bloodstream to further organs such as the bone marrow, spleen and CNS [52]. Due to the ability of the virus to spread and infect other host organs, the initial silent infection may quickly develop more negative effects.

1.1.7. NPEV homology modelling and phylogenetic studies

Enterovirus is the most dominant subgroup of the Picornaviridae family with a total of 29 subgroups. The different subgroups and individual serotypes show varying circulation patterns and infections manifest in a range of illnesses. Large scale outbreaks are often associated with variation in the genotype despite being the same subtype [53]. The different subtypes are divided between them according to neutralization of specific antisera.

1.2. Immune response to viral meningitis

1.2.1. Cytokines and chemokines in viral meningitis

Many biological processes rely on signalling from chemical stimulus. Especially immune responses are often triggered and directed through chemokines and cytokines release. The overall role of chemokines and cytokines during an infection with a viral agent has been studied from many different points of view. This has led to a better understanding of the involvement of distinct inflammatory and non-inflammatory cytokines in leukocyte trafficking and migration during a viral infection of the CNS. Cytokines are involved in almost all biological processes and maintain an important regulatory element. Most are short (5-10kDa) polypeptide messenger molecules but some may also be glycoproteins [54-56]. They can be divided into four major subgroups depending on their structural organization of conserved cysteine residues in the amino terminus. Cytokines/chemokines have been studied intensely due to their significant involvement during inflammation, especially when investigating innate immune cell access into the CNS following an infection

Involvement of CXCL10, IL-1β, CCL2 and CXCL12 has been shown during viral meningitis, amongst others being caused by echovirus 30, and encephalitis [57-60]. Further investigations showed that even IL-6 and TNF- α, which are usually more linked to bacterial meningitis, are present in the CNS during an aseptic viral meningitis [61]. Throughout the life cycle of T-lymphocytes their chemokine receptor expression patterns undergo constant changes, which influence the migration destinations [62]. Also, an important chemokine receptor interaction in relation to viral CNS infection is CXCL12. Interacting with its receptors CXCR4 and CXCR7 it has a vital role in the overall immune surveillance of the CNS through enhancing inter leukocyte interaction [63]. This chemokine, applied in an *in vitro* model of the human BCSFB, has shown to increase the migration of T lymphocytes [36]. The importance of CXCL12 levels has also been shown in murine West-Nile virus (WNV) models. Here, high levels of CXCL12 cause high concentration of leukocytes in the perivascular space and upon downregulation of the chemokine, the cells penetrated the brain barrier into the infected CNS [64].

The importance of CXCL12 during maintenance of the BBB has been studied in an *in vivo* mouse experimental autoimmune encephalomyelitis model. During disease progression it has been noted that the polar secretion of CXCL12 gets altered. This leads to a concentration

of $CXCR4^+$ cells in the brain parenchyma. This cell accumulation might further enhance the negative effects of the infection. Further, it was also shown that other parts of the immune system are influenced by an alteration in the communication of CXCL12 with its receptor. TH1 inflammatory chemokines were overexpressed due to a lack of receptor-ligand interaction of CXCR4 and CXCL12 [65]. The importance of the ligand-receptor interaction can also be seen during HIV-mediated CNS pathology. In this disease progression, $CD14^+$ and $CD16^+$ monocytes are attracted to the infected CNS through the consistently high expression of CCL2 during HIV infection. The intrusion of infected monocytes into the CNS leads to the production and release of an array of proinflammatory cytokines such as IL-6 and TNF- α. These cytokines with their proinflammatory infect add to the disruption of the BBB [66].

The importance of shifting from proinflammatory to anti-inflammatory cytokines has been observed in E-30 infection. After infection the highly expressed proinflammatory cytokines, IL-6, IL-8 and TNF- α were replaced by anti-inflammatory cytokines such as IL-10 and TNF- β1 [67]. This goes in line with high levels of IL-8 and CXCL10 measured in the CSF of children suffering from brainstem encephalitis caused by the infection with EV71 [68].

1.2.2. Immune cell migration in viral meningitis

Once a pathogen has been recognized by cells of the human immune system, a cascade of events leads to the elimination of the pathogen. From the blood stream immune cells cross one of the protective barriers of the CNS. This occurs to a large extent at the BCSFB, where cells move through the fenestrated endothelial cells and either para- or transcellularly across the epithelial cell layer. The migration and transmigration into the CNS of the different cell populations is tightly controlled through cytokines and chemokines. During brain stem encephalitis caused by enterovirus 71, for example, the immune response has shown to be controlled by T lymphocytes, which use CXCL10 to regulate the host response [59].

During viral infection of the CNS mainly the influx of macrophages and T-lymphocytes can be noted, whereas the migration of PMN occurs at a lower rate. However, during the early phase of NPEV meningitis the population of migrating cells within the CNS is dominated by PMNs. This early migration of PMN is then followed by pleocytosis with mainly mononuclear cells. Particularly $CD4^+$ T-lymphocytes make up this population at later stages of the infection. The migration of monocytes and lymphocytes, which appears as the CNS infection

is more pronounced, is believed to be facilitated by the earlier PMN migration [69]. PMNs also play an important role during the viral clearance of WNV-infected CNS. Following WNV-infection, the stimulation by CCL7 triggers PMN and $CD8^+$ T cells migration to the site of infection [70]. At the site of the BCSFB the importance of CCL 12 during the migration of CVB3-infected $nestin^+$ myeloid cells has been shown [71]. Furthermore, B cells have been proposed to enhance further spread of the infection. The “Trojan horse” mechanism, where virus particle travel around the host inside infected immune cells, is suggested to allow viral particles to move around the host [72].

2. Hypothesis and Aims

The pathogenesis of meningitis by echovirus-30 has not been entirely deciphered yet. The BCSFB seems to play an important role as a major entry site for various viruses and immune cells. Furthermore, the immune response and in particular the sequential transmigration of leucocytes has not yet been studied in the context of E-30 CNS infection. Despite knowledge of the predominance of PMNs in CSF pleocytosis in early stages of NPEV meningitis, which is followed by an influx of $CD3^+$ T lymphocytes into the CSF, the sequential immune cell migration into the CNS during E-30 infection has not been dissolved yet. For this purpose, a previously established human *in vitro* model of the BCSFB, based on human choroid plexus papilloma (HIBCPP) cells, has been applied. The polar HIBCPP cells were grown on inverted cell culture inserts, which enabled the infection and addition of leucocytes to the physiologically relevant basolateral cell (blood) side.

The BCSFB has been identified as the main entrance site of Non-polio-enteroviruses (NPEV) into the CNS in both murine *in vivo* models as well as human *in vitro* models. Previous work carried out in the laboratory had confirmed the ability of echovirus 30 (E-30) Bastianni, the prototypic enterovirus reference strain, to infect human plexus epithelial cells, replicate and cause the synthesis and release of specific chemokines from the plexus epithelial cells. Building up on this, we wanted to investigate the link between different cell populations migrating in sequence. In particular, possible interactions or effects on migration of PMN and $CD3^+$ T lymphocytes in the presence of E-30 Bastianni were investigated. The effects of specific chemokines, namely IL-8 and CXCL 12, on their respective immune cells, PMN and $CD3^+$ T lymphocytes, in relation to migration rates were examined *in vitro*. Furthermore, we were interested in the analysis of specific chemical patterns during the infection process and to determine whether the release occurs from the basolateral or apical epithelial cell side.

Seasonal outbreaks of E-30 may be in part due to mutations in the genome; the most important mutations, in this aspect, are found within the VP1 region [73]. Motivated by the recent important seasonal outbreaks of E-30 infections in Europe, we compared the effect of three clinical outbreak strains (13-311, 13-759 and 14-397), isolated in Germany in 2013, to E-30 Bastianni. Possible strain dependent effects on junctional protein morphology and barrier integrity of HIBCPP cells were investigated by means of molecular techniques such as immunofluorescence analysis, genome sequencing, homology studies, PCR and both

transepithelial electrical resistance (TEER) and paracellular dextran flux measurements. In previous studies on infected porcine cells, both para- and transcellular migration of immune cells has been observed. We assume that the migration pathways of leucocytes across the E-30-infected BCSFB may vary depending on the integrity of the barrier. Therefore, we applied immunofluorescent evaluations, transmission electron microscopy (TEM) and focal ion beam (FIB) microscopy to determine the pathway of PMN and T lymphocytes across infected and uninfected HIBCPP cells. The focus of this work was to expand our understanding of enteroviral meningitis and further proof the suitability of the HIBCPP cell model to study the effects of infection with E-30 on the BCSFB.

3. Materials

3.1. Cells

3.1.1. Cell lines

As a model of the human BCSFB, human choroid plexus papilloma (HIBCPP) cells were used [74]. The choroid plexus papilloma cells show the characteristic properties, being a high TEER (when seeded on membranes), intact cell-to-cell TJ and AJ and a low permeability to macromolecules [31], which are necessary to mimic the *in vivo* conditions.

For virus propagation and control experiments, we also used human rhabdomyosarcoma (RD) cells. These are commonly used with non-polio enteroviruses (NPEV).

3.1.2. Primary cells

To investigate leucocyte transmigration, human naive $CD3^+$ T lymphocytes and polymorphonuclear neutrophils (PMN) were isolated from EDTA-anticoagulated peripheral blood of healthy adult volunteers after informed consent was taken. Approval was provided by the local ethics committee of the Medical Faculty of Mannheim, Heidelberg University (2009-327N-MA). T lymphocytes were kept in culture for up to five days, whereas the PMN were used on the day of isolation.

3.2. Echovirus 30 strains

The national reference centre for poliomyelitis and enterovirus (NRC PE) at the Robert-Koch Institute (RKI), Berlin, Germany, provided all four Echovirus 30 (E-30) strains for the experimental procedures. The clinical prototype strain Bastianni was isolated in 1958 from a patient suffering from aseptic meningitis [75]. The outbreak strains 13-311, 13-759 and 14-397 were isolated in 2013 during a German outbreak of NPEV meningitis. All viral strains were propagated and titrated prior to infection studies (Method under section 4.3 Virus).

3.3. Cell culture media and supplements

Name	Origin
DMEM/F12 1:1 (1X) liquid + L-Glutamine + Hepes (15nM)	Gibco/Life Technologies, Paisley, UK
DMEM/F12 1:1 (1X) liquid + L-Glutamine + Hepes (15nM) + Phenol red	Gibco/Life Technologies, Paisley, UK
RPMI 1640	Gibco/Life Technologies, Paisley, UK
RPMI 1640 + Phenol red	Gibco/Life Technologies, Paisley, UK
Foetal calf serum (FCS)	PAA, Pasching, Austria
Penicillin/Streptomycin	MP Biomedicals, Illkirch, France
DMSO	Sigma Aldrich, Steinheim, Germany
Trypsin 0,25% with EDTA Na liquid	Gibco/Life Technologies, Paisley, UK
Trypan blue	Sigma Aldrich, Steinheim, Germany
Human insulin	Sigma Aldrich, Steinheim, Germany
Bovine Serum Albumin (BSA)	PAA, Pasching, Austria
HBSS (1x) Ca/Mg	Life Technologies, Paisley, UK
HBSS (1x) without Ca/Mg	Life Technologies, Paisley, UK
Ammonium chloride	Sigma-Aldrich, Steinheim, Germany
Biocoll	Biochrom KG, Berlin, Germany
Polymorphprep	Axis-Shield, Dundee, Scotland

3.4. Buffers and solutions

Name	Composition	Origin
DPBS	1x liquid -/- Mg/Ca	Gibco/ Life Technologies, Paisley, UK
Fixing solution	4 % formaldehyde(v/v)	Neolab, Heidelberg, Germany
T lymphocyte isolation buffer	PBS (-/-) + 2mM EDTA + 2% FCS	Gibco/ Life Technologies, Paisley, UK Gibco/ Life Technologies, Paisley, UK PAA, Pasching, Austria
Permeabilised solution	DMEM/F12 1:1 1x liquid + L-Glut + 15mM Hepes w/o phenol red 1 % BSA (w/v) 0.5 % Triton X100 (v/v)	Gibco/ Life Technologies, Paisley, UK PAA, Pasching, Austria Sigma Aldrich, Steinheim, Germany
TAE buffer	20 ml 50x TAE buffer 980 ml dist. H_2O	Biorad, Munich, Germany
Washing buffer (IF)	DPBS 1x liquid -/- Mg/Ca 1 % BSA	Gibco/ Life Technologies, Paisley, UK PAA, Pasching, Austria
Erythrocytes lyses buffer	dH_2O + 4.15g ammonium perchlorate + 0.5g potassium bicarbonate + 0.4% EDTA	

Name	Composition	Origin
NuPAGE MOPS Running buffer 20x		Life Technologies, Paisley, UK
NuPAGE Transfer buffer 20x		Life Technologies, Paisley, UK
Tween 20 (10%)		BioRad, Munich, Germany
Immobilon Western Chemiluminescent HRP Substrate		Millipore, Darmstadt, Germany
Glutaraldehyde, 25 % EM-grade		Polyscience, Niles, USA
Triton X- 100		Sigma-Aldrich, Steinheim, Germany

3.5. Antibodies (Primary and Secondary)

Name	Working dilution	Origin
Anti- actin (mouse)	1:20.000	Sigma Aldrich, Steinheim, Germany
Phalloidin Alexa Fluor 660	1:60	Molecular Probes, Eugene, Oregon, USA
Anti- ZO1 (rabbit)	1:250	Invitrogen, Carlsbad, California, USA
Anti- Occludin (rabbit)	1:250	Invitrogen, Carlsbad, California, USA
Anti- E-cadherin (rabbit)	1:250	Invitrogen, Carlsbad, California, USA
Anti- enterovirus VP1 (clone 5-D8/1) (mouse)	1:250	Dako, Santa Clara, USA

Name	Working dilution	Origin
Chicken anti-Rabbit Alexa Fluor 594	1:500	Molecular Probes, Eugene, Oregon, USA
Chicken anti-Rabbit Alexa Fluor 488	1:500	Molecular Probes, Eugene, Oregon, USA

3.6. Fluorescent dyes

Name	Origin
4'-6-diamidino-2-phenylindole dihydrochloride (DAPI) (1:50.000)	Calbiochem, Darmstadt, Germany
CellTrace Calcein green, AM	Life Technologies, UK
CellTrace Calcein red-orange, AM	Life Technologies, UK

Name	Origin
Dextran- TexasRed	Life Technologies, UK

3.7. Chemical solutions and chemokines

Name	Origin
ß-mercaptoethanol	Sigma Aldrich, Steinheim, Germany
ProLong Gold Antifade	Molecular Probes, Eugene, Oregon, USA
RNase/DNase free water	Sigma Aldrich, Steinheim, Germany
IL-8 (recombinant human)	R & D Systems, USA
CXCL 12 (recombinant human)	Preprotech, Germany

3.8. Kits and assays

Name	Origin
Cytokine Multiplex Array (23 plex) **Eotaxin, G.CSF, GM-CSF, INF alpha2, INF-gamma, IL-10, MCP-3, IL-12 p40, IL-12 p70, IL-13, IL-17a, IL-1 ra, IL-1 alpha, IL-1 beta, IL-4, IL-6, IL-7, IL-8, IP-10, MCP1, MIP-1 alpha, MIP-1 beta, RANTES, TNF-alpha**	Millipore, St. Charles, MO, USA
Cytokine Multiplex Array (5 plex) **CXCL 11, CCL 19, CCL 29, CXCL 9, M.CSF**	Millipore, St. Charles, MO, USA
Dynabeads untouched naive T-cells	Invitrogen Dynal AS, Oslo, Norway
LIVE/DEAD Viability Kit for mammalian cells	Molecular Probes, Eugene, Oregon, USA
RNA easy Micro Kit	Qiagen, Hilden, Germany
QIAShredder	Qiagen, Hilden, Germany
Taq DNA Polymerase Kit (1000 U)	Qiagen, Hilden, Germany
Cytotoxicity Detection Kit (LDH)	Roche, Mannheim, Germany
Viral RNA Mini Kit	Qiagen, Hilden, Germany
SuperScript III reverse Transcriptase	Invitrogen, Karlsruhe, Germany
Phusion High-Fidelity PCR Master Mix	New England Biolabs, Ipswich, USA
Gel extraction kit	Qiagen, Hilden, Germany

3.9. Western blot

Name	Composition	Origin

Name	Composition	Origin
NP40 lysis buffer	1 x 10x RIPA buffer 1 x 10x Protease Inhibitor Cocktail 1 mM Na_3VO_4 dist. H_2O	Millipore, Billerica, MA, USA Sigma Aldrich, Steinheim, Germany Sigma Aldrich, Steinheim, Germany
MOPS running buffer	20 ml 20x NuPAGE SDS MOPS 380 ml dist. H_2O	Novex, Life Technologies, Carlsbad, CA, USA
TBST- buffer	50 ml 20x TBS buffer (200nM Tris, 3M NaCl, pH 7.6 (HCl) 10ml Tween 20 (10%) 960 ml dist. H_2O	Carl Roth, Karlsruhe, Germany Applichem, Darmstadt, Germany Applichem, Darmstadt, Germany
Transfer buffer	50 ml 20x NuPAGE transfer buffer 200 ml Methanol 750 ml dist. H_2O	
Gene Ruler 100 bp DNA ladder		Fermentas, St. Leon-Rot, D
4x loading buffer		Novex, Life Technologies, Carlsbad, CA, USA
NOvex Sharp Protein Standard		Novex, Life Technologies, Carlsbad, CA, USA
HiMark Pre-Stained Protein Standard		Novex, Life Technologies, Carlsbad, CA, USA
100x reducing agent		Novex, Life Technologies, Carlsbad, CA, USA
TAE buffer	20 ml 50x TAE buffer 980ml dH_2O	BioRad, Munich, Germany
Immobilon Western Chemiluminescent HRP		Millipore, Billerica, USA

3.10. PCR and quantitative PCR

Gene	Forward Primer (5‘-3‘)	Reverse Primer (5‘-3‘)	Reference
CXCL 3	CGCCCAAACCGAAGTCATAG	5‘GCTCCCCTTGTTCAGTATCTTTT	[76]
M-CSF	AGACCTCGTGCCAAATTACATT	AGGTGTCTCATAGAAAGTTCGGA	[76]
CXCL 11	AGAGGACGCTGTCTTTGCAT	5‘-GTCCTTTCACCCACCTTTCA	[77]
IL-7	GTCGTCCGCTTCCAATAACC	TCGCGAATTTCCGAATCACC	This work [78]
GAPDH	TGTTGCCATCAATGACCCCTT	CTCCACGACGTACTCAGCG	[34]
ZO1	GCCAAGCAATGGCAGTCTC	CTGGGCCGAAGAAATCCCATC	This work [78]
Occudin	AGGAACACATTTATGATGAGCAG	GAAGTCATCCACAGGCGAA	This work [78]
E-cadherin	CCTGCCAATCCCGATGA	TGCCCCATTCGTTCAAGTA	This work [78]
VP1 (qPCR)	GACATGGTGCTGAAGAGTCTATTGA	GCTCCGCAGTTAGGATTAGCC	This work [37]

3.11. Software and databases

Name	Origin
Basic local alignment search tool (BLAST)	National Centre for Biotechnology Information (NCBI)
GenBank	NCBI
ClustalW	Molecular Evolutionary Genetics Analysis (MEGA)

3.12. Laboratory equipment

Description	Model	Origin
Pipettes	0,1 – 1000 µl	Eppendorf
Pipetboy	Pipetboy Comfort	IBS Inegra Bioscience
Sterile bench	Hera Save	Thermo Fischer
Voltohmeter + Electrode	Millicell-ERS MERSSTX 01	Millipore
Vortex	Analog Vortex Mixer	VWR
Scale	CPA 623s, Extended ED2245	Satorius
Water bath	SW22	Julabo
Rolling mixer	Assistant 348 RM5.40	Karl Hecht KG
Gel electrophoresis instrument	XCell SureLook electrophoresis Novex Mini Cell	Invitrogen
Microwave	MWG758	Clatronic
PCR cycler	2720 Thermocycler MX3005P	Applied Biosystems
Light microscope	Axlovert 40C	Zeiss
Fluorescent microscope	ApoTome/Lens 636/1.4/ Zen software	Zeiss
Heating block	Thermomixer compact	Eppendorf
Gel chamber	SUB-Cell GT	BioRad
Magnetic stirrer	VMS-C4-2	VWR
Incubator	Hera Cell 240	Thermo Fischer
Autoclave	5075 ELV	Systec
Blotting instruments	TE22 Mighty Small Transfer	Hoefer
Chemiluminescent detector	Chemi Smart 5100	Vilber Lourmat
Gel documentation instrument	Biovision- 3026 WL/26MX	Vilber Lourmat
Cell counter (manual)	0,0025 mm^2	Neubauer
Centrifuge	Micro 200R Rotor 2424A Rotana 460R Rotor 5624	Hettich Hettich

Description	Model	Origin
	Picofuge II Microfuge	Stratagene

3.13. Consumables

Name	Origin
TipOne 1000 µl XL Graduated Tip (sterile)	Starlab, Germany
TipOne 200 µl Graduated Tip (sterile)	Starlab, Germany
TipOne 100 µl Graduated Tip (sterile)	Starlab, Germany
TipOne 10/20 µl Graduated Tip (sterile)	Starlab, Germany
TipOne 200 µl Bevelled Graduated Tip (sterile)	Starlab, Germany
TipOne RPT 200 µl Graduated Tip (sterile)	Starlab, Germany
TipOne RPT 100 µl Graduated Tip (sterile)	Starlab, Germany
TipOne RPT 10 µl Graduated Tip (sterile)	Starlab, Germany
12-well cell culture plate	Starlab, Germany
24-well cell culture plate	Starlab, Germany
48-well cell culture plate	Starlab, Germany
T 75 cm^2 tissue culture flasks	Greiner, Germany
24-well cell culture inserts (6x10^5 pores/cm^2, 0.33cm^2)	Millipore, Germany
Safe lock tube 0,5 ml, 1,5 ml, 2 ml	Eppendorf, Germany
Cryo tube 1 ml, 2 ml	Nunc, Denmark
Microscope slide 76 x 26 mm	Langenbrick, Germany
Cover slips 24 x 50 mm	VWR, Germany
NuPAGE Novex 4-12 % Bis-tris gel 1,5 mm	BioRad, Germany
Nitrocellulose Transfer Membrane 0,45 µm	BioRad, Germany
Leucosept tubes	Greiner, Germany
Mx3000P Optical Strip Caps	Agilent Technologies, Germany
Mx3000P Strip tubes	Agilent Technologies, Germany
Chromatography paper Whatman 3 mm	Maidstone, UK

4. Methods

4.1. Cell Culture

4.1.1. Human choroid plexus papilloma cells

HIBCPP cells were incubated in T-75 cell culture flasks at 37°C and 5 % CO_2 until they reached 80-90 % confluence. The cell layer was washed with prewarmed DPBS and after discharging the cell debris, warm Trypsin was added to the cell layer. The flasks were incubated at 37°C for about 15-25 min. At regular intervals of 5 min, it was verified, whether all cells had rounded of and detached from the flask surface. The reaction was stopped by addition of 10 % HIBCPP cell culture media. The suspended cells were centrifuged for 10 min at 500 rpm at room temperature (RT) and the supernatant discharged. The cell pellet was thoroughly resuspended in an exact volume of 10 % media. The viable cell concentration was determined through trypan blue staining and subsequent application onto a Neubauer cell counter (Fig. 5).

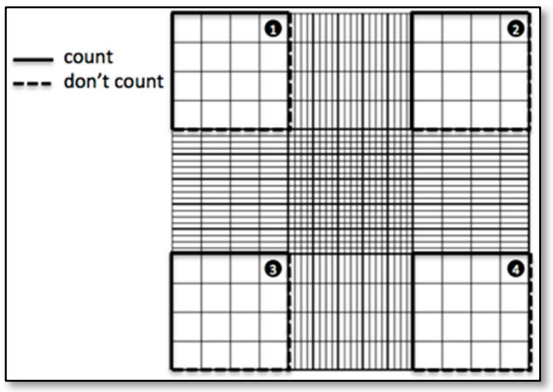

Figure 5. Representation of a Neubauer cell counter. Indicated are the 4 squares from which cells were counted. Cells touching the dotted lines were not taken into consideration, whereas cells found on the solid lines were used to determine cell concentration. (https://www.hemocytometer.org/hemocytometer-protocol/)

To calculate the cell concentration within the suspension, all cells within the indicated squares (Numbers 1, 2, 3 and 4) and on the edges with continuous lines (Fig. 5), were counted and the following formula was applied:

$$Cell\ concentration = \frac{(combined\ cells\ counted\ in\ 1{,}2{,}3\ \&4 * 10^4 * dilution\ factor)}{4}$$

Figure 6. Calculation to determine cell concentration. The sum of the cells counted within the 4 indicated squares was multiplied with the area within the chamber (10^4) and with the dilution factor used. The product of the equation was divided by the number of chambers counted.

4.1.2. Human rhabdomyosarcoma cells

RD cells were also grown in T-75 flasks and the same 10 % cell culture media as for HIBCPP cells was used. The cells were incubated at 37°C and 5 % CO_2, until the layer was about 80-90 % confluent. The cell layer was washed with prewarmed DPBS and after discharging the cell debris, warm Trypsin was added to the cell layer. The flasks were incubated at 37°C for about 5-10 min. At regular intervals, every 2 min, it was verified, whether all cells had rounded of and detached from the flask surface. The reaction was stopped by addition of 10 % HIBCPP cell culture media. The washing and counting procedures were kept the same to the HIBCPP cells as described in section 4.1.1 Human choroid plexus papilloma cells.

4.1.3. Seeding of human choroid plexus epithelial cells

All transmigration and infection experiments were carried out with inverted HIBCPP cell cultures on 24-well filter inserts (5.0 µm pore diameter, $6.0x10^5$ pores/ cm^2, surface area 0.33 cm^2). Empty filter inserts were placed upside down in 12-well plates and warm media was added. To allow appropriate attachment of the cells, 70 µl of the cell suspension, containing app. 70.000 cells, was added on top of the moist inverted filter inserts. The plates were incubated at 37°C for 24 hours, after which the filter inserts were turned and placed into media filled 24-well plates and warm fresh media was added into the filter inserts. Fresh 10 % HIBCPP media was added at regular intervals of two days and the old media discharged. In detail description and video guidance of seeding HIBCPP cells on inverted cell culture inserts has been published (Fig. 7) [79]. A day prior to the planned experimental start, the filters were placed in 1 % HIBCPP cell culture media to stimulate further tightening of the cell layer through serum starvation. The day of the experiment, the filters were

measured again and only filters with appropriate (ensuring barrier integrity and functionality) TEER levels of 215 to 675 Ω x cm² were chosen for the experiments.

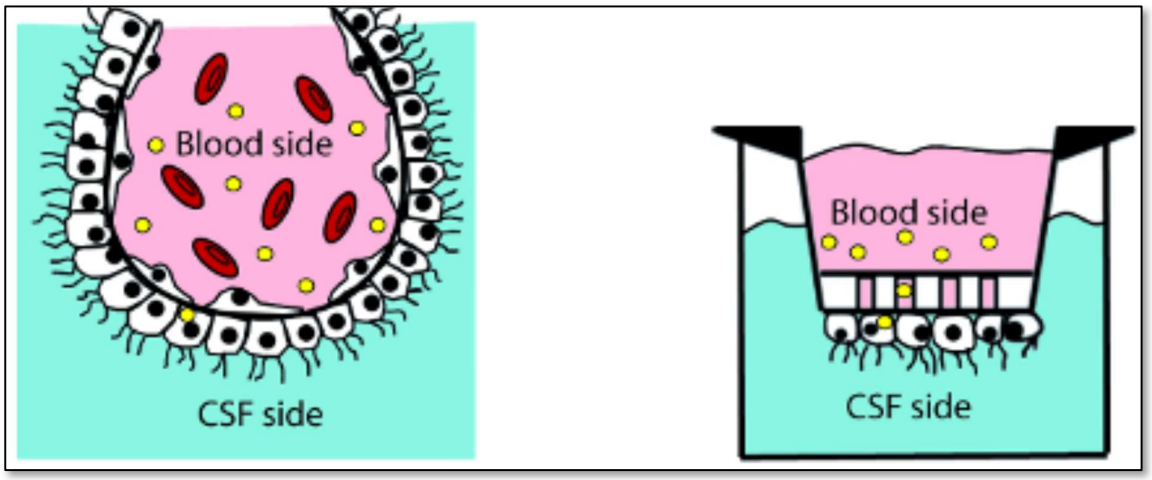

Figure 7. BCSFB in vivo and a schematic illustration of the inverted HIBCPP cell culture model. The HIBCPP cells are seeded on the outside of the filter membrane to mimic in vivo conditions. The erythrocytes (red biconcave disk shape), pathogens (yellow) or other materials can be added to the basolateral HIBCPP cell side, which allows evaluation of pathogenesis and immune cell migration from the blood into the CNS. Modified from Dinner et al., 2016 [79].

4.2. Evaluation of barrier integrity

4.2.1. Measurement of transepithelial electrical resistance

Measuring the resistance against an electic current passed across the cell layer gives an indication of the membrane potential and tightness of the cell-to-cell junctions. This relies on the prinicple that more densly grown and better connected cells (particularly through TJ) cause a higher electrical resistance. Evaluation of the optimum TEER range for our experimental procedures was achieved before the start of this work by the laboratory [31, 33, 34]. The initial cells added, time left to grow and media composition was varied and different HIBCPP cells growth patterns observed. The optimum number (about 70.000 cells) of HIBCPP cells added to the filters and the time required to reach a confluent cell layer was adopted.

The TEER was measured using the tissue voltohmmeter MILLIcell ERS-2. In principle, the tip of the shorter electrode was placed within the filter insert and the tip of the longer electrode in the well compartment (Fig. 8). Due to the silver/silver chloride pellet on each electrode tip, the current can be measured and quantified. The electrode was kept in 80 % alcohol for 10 min before use and then washed off in warm and steril media. The measured values, presented in Ω, were recorded and after substraction of the blank (measurement of the electrical resistance of an empty filter placed in media) filters with a predefined range of 215 to 675 Ω x cm^2 were used for the experiment. Electrical resistance in Ω x cm^2 was calculated to allow comparison between different size filter inserts (Fig. 8).

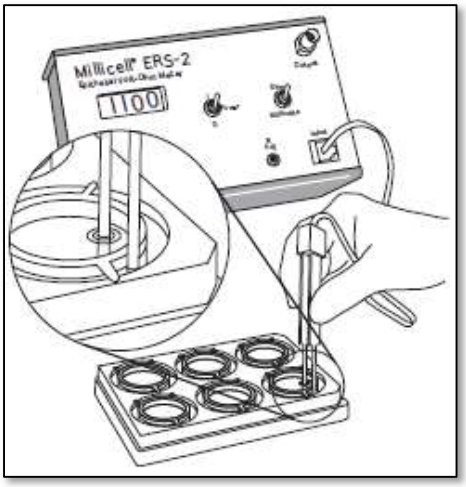

Figure 8. Measurement of TEER of HIBCPP cells in an inverted cell culture system. Graphic representation of TEER measurement with a Millicell ERS-2 voltohmmeter. Special attention should be taken so that the shorter electrode is added into the filter compartment (taken fom Millicell® ERS-2 User Guide).

$$[Measured\ value\ (\Omega) -\ blank\ filter\ (\Omega)] * membrane\ surface\ (cm^2) = x\ (\Omega * cm^2)$$

Figure 9. Mathematical equation applied to determine actual TEER. Inserts were measured, blank distracted and the area coefficent applied to calcuate the elecrical resistance per cm² of HIBCPP cells in an inverted cell culture system.

4.2.2. Measurement of paracellular permeability

As a second parameter of barrier integrity we analysed the paracellular movement of dextran-TexasRed tracer solution (Invitrogen, Germany) from the filter to the well compartment. The fluorescent dye, conjugated to the 3.000 kDa sugar molecules, has optimum excitation at 594 nm. At the start of the experiment 100 µg/ml of dextran-TexasRed was added to the filter compartment (basolateral cell side) and at the end of the experiment the sugar particle concentration within the lower compartment was measured. Therefore, the filter inserts were removed from the 24-well plates and the plates were centrifuged at 1.400 rpm for 10 min at RT to allow attachment of all other cells (i.e.: transmigrated leucocytes) to the well bottom. Exactly 200 µl of media, containing dextran, from each well was transfered to a black 96-well multiwell plate. Using a Tecan Infinite M200 Multiwell reader the excitation levels were measured. Through creation of a standard curve, exact percentage of dextran flux across the HIBCPP cells was evaluated. Low values indicated that the barrier function of the HIBCPP cells remained strong and stable throughout the

experiment. Filters indicating high levels of dextran flux were exluded from the experimental assessment. Internally we considered ≤ 1 % dextan flux per hour as an indication that the barrier was intact [31, 79]

4.2.3. Determination of cell viability

To ensure stable conditions throughout the experiment, we investigated the viability of the HIBCPP cells. This was performed using a LIVE/DEAD® kit, containing two fluorescent agents, which is based on a two-colour discrimination between viable and non viable cells. The cell-permeant dye calcein green AM is able to penetrate the cell membrane and through reaction with esterase, found in the cell cytoplasm, elicits a green fluorescent signal (excitiation/emission max ~495/635 nm). The second fluorescent indicator is ethidium homodimer. It is a weakly fluorescent nucleic acid, which can only penetrate the cell membrane of damaged or non-viable cells. Having penetrated the cell membrane, it intercalates with DNA, which increases the signal (excitiation/emission max ~528/617) about 40-fold.

The viability was verified at numerous time points throughout the experiment. Therefore, the filter inserts were washed once with serum free HIBCPP media. In parallel the master mix, composed of 4 µM ethidium homodimer and 2 µM calcein AM, was added to each filter insert. After an incubation time of 15 min at 37°C in the dark, the filter inserts were washed twice with serum free HIBCPP media to remove any residual non- bound flurescent dye. The results were analysed under a fluorescent microscope and picture documented with a 20x/1.4 objective lens.

4.2.4. Evaluation of cytotoxicity

To evaluate whether any of the added viral strains had a cytotoxic effect on the HIBCPP cells, we applied a lactate dehydrogenase (LDH) assay. The soluble cytosolic enzyme L-lactate dehygrogenase is present in nearly all mammalian cells and catalyses the reaction of L-lactate and NAD^+ to pyruvate and NADH. Healthy cells, with an intact cell membrane, retain the enzyme within the cells, whereas damaged or lysed cells release the enzyme into the supernatant. Therefore an increase in LDH activity in the supernatant is directly

proportionate to the amount of lysed cells (damaged or dead cells). Through application of a commercially available kit, the exact percentage of lysed cells can be determined spectrophotometrically. In a coupled reaction to the formation of NADH, tetrazolium salt INT is reduced to a soluble red flurescent formazan (490nm).

The supernatant of uninfected and unlysed HIBCPP cells was used as a negative control. On the other hand, supernatant from HIBCPP cells lysed with Triton-X, allowing maximum LDH release, was taken as a positive control.

The following formula was applied to calculate the percentage of cytotoxicity for each individual viral strain.

$$Cytotoxicity\ (\%) = \left[\frac{condition\ assay\ well - negative\ control}{positive\ control - negative\ control}\right] * 100$$

Figure 10. Mathematical equation to calculate percentage of cytotoxicity on HIBCPP cells. Cytotoxic effect of each E-30 strain was calculated in relation to maximum possible LDH release.

4.3. Isolation of naive $CD3^+$ T lymphocytes

First, PBMC were obtained via BIOCOLL gradient separation at 2.000 rpm for 20 min at RT (Fig. 11). After a minimum of 2 hours of adherence, $CD3^+$ T lymphocytes were isolated via negative selection (Dynabeads untouched human T cells, Invitrogen, Germany) according to a previously described method [80]. Cells were adjusted to 1 x 10^6 / ml, added to petri dishes and incubated at 37 °C until the experiment commenced. 30 min prior to the start of the experiment, the T lymphocytes were stained with either CellTracer Calcein red-orange or green. Therefore, the cells were washed, counted and concentration set to 1x 10^7 cells in 2,5 ml media. Calcein red-orange or green were added at 2 µM and 1,5 µM, respectively, and incubated for 30 min at 37°C with 5 % CO_2 in the dark. After centrifugation at 1400 rpm for 10 min the supernatant was discharged and the cells diluted to 1x 10^7 cells/ml.

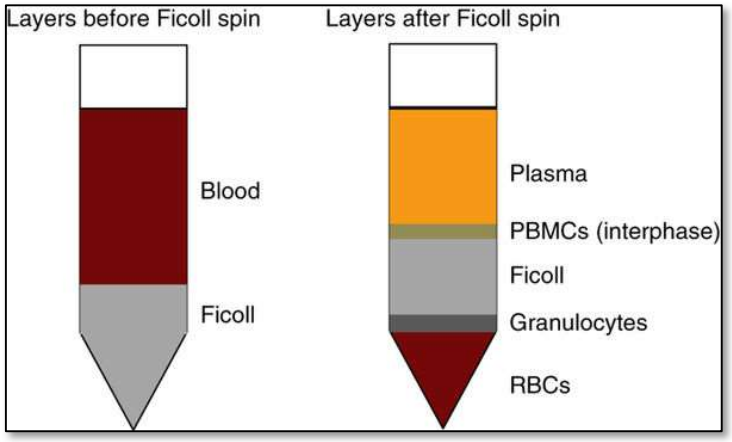

Figure 11. Schematic representation of the PBMC isolation from whole blood. The gradient centrifugation of whole blood in combination with Biocoll creates a gradient from which the cells of interest (PBMC) can be collected [81]

4.4. Isolation of polymorphonuclear cells

PMN were isolated on the day of the experiment from whole blood. The separation process is based on gradient centrifugation with Polymorphprep and was carried out according to manufacturer's instructions (Fig. 12). 15 ml falcon tubes were filled with 5 ml Polymorphprep and then 5 ml blood was very carefully added onto of the layer. The tubes were centrifuged at 1.340 rpm for 35 min at RT without a break to allow formation of a gradient. The supernatant and the upper interphase (containing PBMCs) were discharged with a serological pipette. The lower interphase was collected and washed with HBSS +/+ and then centrifuged for 10 min at 1.400 rpm at 4°C. The supernatant was discharged and the tube was filled up with erythrocyte lyses buffer and incubated for 20 min at 4°C. Subsequent centrifugation at 1400 rpm for 10 min at 4°C separated the PMN from lysed red blood cells. Further washing steps with DPBS +/+ cleaned the pellet of any residual erythrocytes. PMN were counted and set to 1 x 10^6 cells/ml. Staining with either CellTracer Calcein red-orange or green was carried out as previously described for T lymphocytes. The cell suspension was also adjusted to 1 x 10^7 cells/ml.

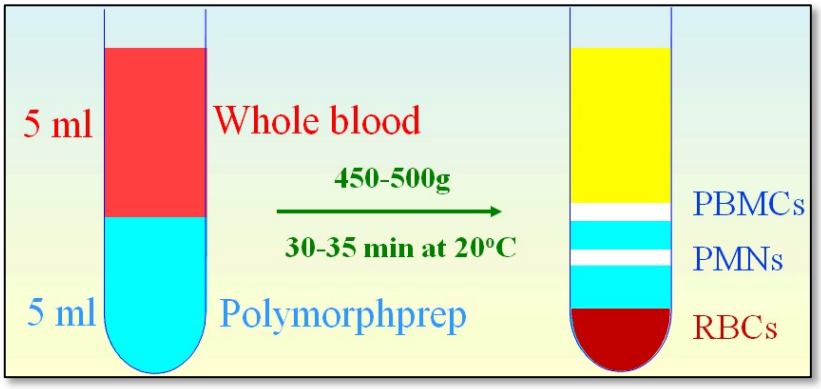

Figure 12. PMN isolation from whole blood using polymorphprep. The gradient centrifugation of whole blood in combination with polymorphprep creates a gradient from which the cells of interest (PMN) can be collected.

4.5. Transmigration assay

After 24 hours of infection with E-30 at a MOI of 0.7 from the basolateral cell side, PMN (4 x 10^5 cells) and dextran TexasRed (100 µg/ml) were added into the filter insert (=basolateral). As chemokines are important mediators for immune cell migration, IL-8 (10 ng/ml) and CXCL12 (100 ng/ml) were added into the well (=apical) compartment. Two hours later, T lymphocytes (4 x 10^5 cells) were also added into the filter inserts. After a total of 28 hours of infection the percentage of migration for both cell types was evaluated and the flux of dextran measured.

4.6. Virus

Viral strains used in this work were obtained from the NRC PE at the RKI. We obtained the prototypic strain Bastianni and the three outbreak strains 13-311, 13-759 and 14-397 isolated in 2013 in Germany.

4.6.1. Viral propagation

Virus was propagated on RD cell layers grown in T-75 flasks. RD cells were grown to 80-90 % confluency and between 50- 200 µl amount of virus from the original stock from the RKI was added. The cell suspension was collected when CPE was present in more than 90 % of the cells. The cell suspension was centrifuged at 4000 rpm for 10 min and cell debris was

discharged. Supernatant was put through two freeze/thaw cycles and centrifugation, for removal of cell debris, was repeated. Finally, the suspension was frozen at – 80°C. The cell free virus containing suspension was sent to Dr. Adams (Virology, University of Düsseldorf) for analysis of viral genome copies per ml.

4.6.2. Determination of viral genome copies

For the quantification of viral genome copies, a quantitative TaqMan-real-time PCR using a two-step-RNA- PCR protocol was performed as previously described (Schneider et al 2012) [36]. The determination of viral genome copies was achieved through a reverse transcription with Ent486R using Sensicript RT and application of standard conditions during amplification carried out in the laboratory of Dr. Adams. The two-step taqMan-real-time PCR included primers for the VP1 protein of enterovirus (under 3.10 PCR and quantitative PCR). The probe used was Ent443T-5'FAM - GTAGTCCTCCGGCCCCTGAATGC - TAMRA-3'. The genome amplification and detection were carried out in an ABI 7500 thermal cycler and results obtained were calculated to state viral copies per ml. The titrated stocks were divided into working stocks to avoid repetitive freeze/thaw cycles.

4.6.3. Infection of HIBCPP and RD cells

For standard infection experiments (all in this work if not otherwise stated) the E-30 Bastianni, 13-311, 13-759 and 14-397 working stocks were thawed and centrifuged at 4000 rpm for 10 min at 4°C. The cell free supernatant was used for infection. With the viral copies per ml obtained from Q-PCR, the multiplicity of infection (MOI) was calculated. Previous work determined that approximately 400.000 HIBCPP cells were present on each filter insert [33, 34].

4.6.4. Infection quantification

To extrapolate the total percentage of HIBCPP cells, which were infected by each virus after 28 hours, we carried out infection of HIBCPP cells in an inverted cell culture system with each E-30 strain at a MOI of 0.7. After the infection period, the filters were washed twice

with warm DPBS and fixed with 4 % formaldehyde (w/v in PBS) for 10 min at RT. The filter membranes were cut out and stained for the HIBCPP cell nucleus (DAPI) and the viral capsid protein (VP) 1. For detailed information on IF please refer to section 4.4.9 Immunofluorescence studies. The stained filter membranes were analysed with a Zeiss Apotome and Zen software. To extrapolate the total percentage of infected cells, 10 fields of view per filter from four independent experiments carried out in duplicates, were counted. The mean value of infected HIBCPP cells per field of view (895,3 µm x 640,8 µm = 0,6 mm²) was taken and multiplied by an area coefficient to determine the overall percentage. The membrane area was 0,33 mm² and we calculate with 400.000 HIBCPP cells in total.

4.7. Genome sequencing

To obtain the complete genomes of all outbreak strains and confirm the published sequence of Bastianni, we carried out reverse transcription from purified viral RNA. The procedure was carried out in our laboratory by Dr. Morozov (University of Heidelberg). The RNA was extracted from the supernatant after an infection experiment with the QIAamp viral RNA mini kit. The RNA conversion into cDNA was performed with SuperScript III Reverse Transcriptase. Both these kits were used according to manufacturer's recommendation. The synthesised cDNA was amplified applying the Phusion High-Fidelity PCR Master Mix with HF buffer. After the amplification, we had small products of about 1-4 kbp, which were purified through running them on a gel. This step was performed with a gel extraction kit. Finally, the genomic sequences were sent to GATC and exact nucleotide sequence was determined with an ABI 3730xl DNA analyser. The sequences can be accessed online with the accession number KY888272 – KY888275 in GenBank.

4.8. Phylogenetic analysis

To create a phylogenetic tree, containing the four E-30 strains analysed in this project, the bioinformatic tools available from NCBI were used. A basic local alignment search tool (BLAST) search, of the genomic regions encoding for the capsid proteins and 3D polymerase (3Dpol), was carried out against the non-redundant database in Genbank. For purpose of comparison the outgroup was chosen according to several parameters. E-6 (AY3025588.1)

and E-11 (X80059.1) were chosen as they are not part of our ingroup (E-30 strains used in this work) and are not too distantly related (making incidental homology impossible). Precise analysis and construction of a phylogenetic tree were performed. The alignment of the sequences was done with the help of Molecular Evolutionary Genetics Analysis (MEGA) 7 and CLustalW. These programs are freely accessible online. For the construction of a phylogenetic tree the Tamua Nei model for nucleotide substitution was chosen. It distinguished during a nucleotide substitution between the two possible transitions, from A to T and from C to G or vice versa. Even though the transversions are assumed to be of equal rates, they must not be at the same rate as the transitions. Bootstrap- resampling test with 1000 replicates was performed to show the trustworthiness of the phylogenetic relationships calculated between the different echovirus strains.

4.9. Molecular assays and methods

4.9.1. RNA isolation

At the end of an infection experiment, the filter inserts were washed twice with PBS and placed upside down in a 12-well cell culture plate. As we used the RNeasy Mini kit, each filter was treated with 75 µl of RLT lyses buffer; cell full lyses were ensured by carefully scratching with the pipette filter tip and pulling the lysate up and down several times. RLT solution from two filters was pooled. The lysates were stored on ice before freezing at -80°C until further use. The lysates were thawed on ice and quickly warmed to 37°C to resuspend the chaotropic agents. Lysates were added to QiaShredder tubes and centrifuged for 2 min at maximum (14.000 rpm) speed at RT. The supernatant was combined with equal volumes of 70 % ethanol and homogenised through pipetting up and down carefully. The lysate was then transferred to RNeasy tubes and centrifuged for 15 sec at 10.000 rpm at RT to ensure attachment of the RNA to the tube surface. Contamination through presence of DNA was hindered through washing with 350 µl RW1- wash buffer and subsequent incubation with 80 µl DNase solution for 15 min at RT. Another washing step with RW1- wash buffer removed the DNase and was followed by a wash step with 80 % ethanol solution. The tubes were dried through a 2 min centrifugation at 14.000 rpm and after addition of 25 µl dH_2O and centrifugation for 1 min at 14.000 rpm at RT, the RNA was collected from the bottom of the tube.

4.9.2. Determination of RNA quantity and quality via Nanodrop

The quality and concentration of RNA was verified with the help of a Nanodrop. To start, the machine was cleaned with RNase/ DNase free water and a zero value was set using the same liquid. Sample volumes for measurement were 2 µl. The concentration of RNA was measured at 260 nm and an absorption of 1 equals 40 µg/ml RNA. The ratio of optical density at 260/ 280 nm was used to control the purity and ensure the absence of any contaminates. The ratio of clean RNA ranges from 1,8- 2,0 and values below or above indicate a contamination with other proteins or phenol. To ensure that no contamination with EDTA or carbohydrates was present, the ratio OD 260/230 was calculated. Only RNA without any contamination and at reasonable concentrations were used for further analysis.

4.9.3. cDNA synthesis for qRT PCR

For synthesis of cDNA from isolated RNA the Affinity script qPCR cDNA Synthesis kit was used and manufacturer's instructions followed. Oligo dT primers were applied in combination with genetically modified reverse transcriptase isolated from the Maloney murine leukaemia virus. The cycles were set to 5 min at 25°C for annealing, 15 min at 42°C for cDNA synthesis and 5 min at 95°C to terminate the reaction and the cDNA was stored at -20°C.

4.9.4. Agarose gel electrophoresis

For a 3 % agarose gel, 1,7 g of agarose were added to 90 ml of 1 x TAE buffer and heated (to boil) in a microwave. After allowing the liquid to cool down, 3 µl ethidium bromide (1 mg/ml) were added and homogenised. The ethidium bromide is an intercalating agent and moves between base pairs of DNA, which can then be visualised. The excitation spectrum of ethidium bromide is changed through the interaction with the heteroaromatic rings from the nucleotides and the aromatic rings from itself. The emission spectrum of DNA and RNA bound ethidium bromide is at 605 nm. The gel is left to cool down and harden and added to a gel chamber containing enough 1 x TAE buffer to fully cover the gel. The samples were

added into the predesigned wells and a marker (Gene Ruler 100 bp DNA Ladder) was added into the first and last well of each lane. The electrophoresis was performed for about 30 min with 120 V. These parameters may vary depending on the size of the fragments analysed. For shorter fragments, the gel was regularly checked from 15 min onward. Visualization of the separated RNA fragments was performed with a BioVision-3026 camera and the VisionCapt. Software.

4.9.5. Whole protein extraction

For use during western blots the whole proteins from HIBCPP and other used cells were isolated. Therefore, the filters were washed twice with PBS and placed upside down in a 12-well cell culture plate. For each filter 70 µl of modified RIPA buffer was added to the cell layer and through careful scratching and pipetting up and down, the protein was collected. The protein lysate was immediately stored in liquid nitrogen to hinder any protein breakdown. Before further use, the tubes were thawed on ice and vortexed before 10 min centrifugation at 14.000 rpm at RT. The pellet, containing cell debris, was discharged and the supernatant collected. The protein concentration for each tube was measured.

4.9.6. Protein concentration measurement

Protein concentration was measured with the DC Protein assay, which is based on the Lowry method [82]. During this process, peptides and Cu^{2+} ions form complexes. This reaction is enabled and stabilized through the presence of copper-tartrate solution (Reagent 1). Following this reaction, the Cu^{2+} ions are reduced to Cu^{1+} which, after the addition of folin's reagent, causes a reduction of folin's reagent. The reduction process of this reagent causes a colorimetric switch from yellow to blue. The colour change is directly proportional to the amount of total protein present in the solution. For calculation, a standard curve was created from a 10 µg/ml BSA stock and subsequent serial dilutions. For each sample, standard curve included, 2 µl was added to a 96-well plate. 20 µl of Reagent A' (20 µl Reagent S / 1 ml Reagent A) was added to each well. The addition of 200 µl of Reagent B caused the previously described colour change. The plates were carefully shaken to perfectly mix all reagents and incubated for 15 min at RT in the dark. The absorption was measured

with a Tecan Reader Infinite M200 at 660 nm and analysed with the I-control software. The standard curve was constructed with the values from the serial dilution of the BSA stock. Protein concentration in each sample was calculated with the standard curve values.

4.9.7. SDS-PAGE and immunoblot

Protein analysis was carried out with a SDS-PAGE separation, based on size (molecular weight) of the protein and subsequent western blot. Proteins were heated and therefore lost their structural characteristics, leading to all proteins being linear during the electric separation on the gel. The detergent was added to both the sample buffer and the gel and causes all proteins to be negatively charged. This causes repulsion between each other. Further addition of a reducing agent leads to breakdown of disulphide bonds. Considering the protein concentration determined prior to the SDS-PAGE, equal amounts of whole protein were loaded onto the gel. The samples were thawed on ice, combined with reducing agent and 4 x loading buffer and heated for 5 min at 99°C. The samples were loaded onto a gel in combination with a size marker (Novex Sharp or HiMark pre-stained Protein Standard). Separation of the proteins was achieved by running 200V across the 4-12 % Bis-tris gel surrounded by ice cold MOPS loading buffer. The instrument was cooled throughout the separation process. Separation was controlled at regular intervals and the process was stopped when the marker reached the end of the gel. Transfer of protein onto a nitrocellulose membrane was done at 20 V for 16 hours at 4°C in transfer buffer.

After the transfer, the membranes were cut if necessary and incubated for one hour at RT in milk-buffer solution (5% TBST buffer). After at least three washing steps with TBST buffer the membranes were incubated with the primary antibodies. The antibodies rabbit-anti-ZO1, rabbit-anti-Occludin and rabbit-anti-E-cadherin were added at 1:500 dilution; mouse-anti-ß-actin was added at 1:10.000 dilution over night at 4°C on an automatic roller. Before addition of the secondary antibodies, the membranes were washed extensively in TBST. Secondary antibodies used for detection of the whole protein were either anti-rabbit or anti-mouse horseradish peroxide (HRP), conjugated and added at dilutions of 1:5.000 for one hour at room temperature. The conjugated enzyme catalyses the oxidation of luminol, which, in combination with the coupled antibody, can be visually detected. For visualization,

the chemiluminescence detection camera Chemi Smart 5100 was used and recorded with the Software ChemiCapt 5000.

4.10. Cytokine bead array (CBA)

For the cytokines bead array, cell free supernatant from both the basolateral and apical cell side were collected after 24 hours of infection and frozen at -80°C. The cytometric bead array was carried out following manufacturer's instructions. In brief, the fluorescent-coded magnetic beads bind to their target protein and subsequently, a biotinylating detection antibody attaches to the construct. The reporter molecule, streptavidin-PE conjugated, is introduced and binds to the bead/protein/antibody construct. This allows detection of a fluorescent signal with an appropriate machine (ex. MAGPIX®). The principle of detection is explained in figure 13.

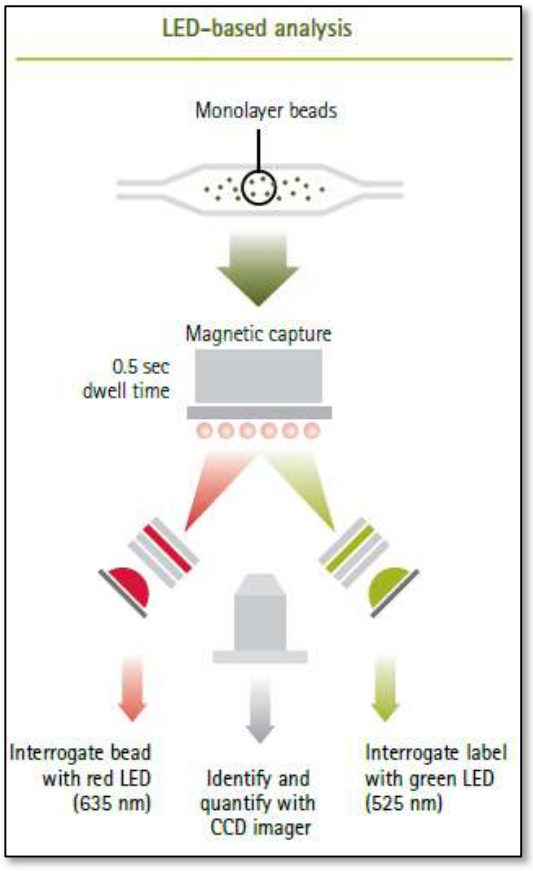

Figure 13. Principles of LED-based cytokine bead array. Overview of the steps involved during the CBA. The specific beads bind to their respective protein and can be analysed through the MAGPIX system (Luminex) [83].

4.11. Immunofluorescence analysis

Immunofluorescence analysis was carried out to analyse the cellular structure, location of proteins of interest and sequential transmigration of leucocytes. Following sequential transmigration of PMN and T lymphocytes across the HIBCPP cells, the cell layers were carefully washed in PBS and fixed in 4 % formaldehyde for 10 min at RT. After infection studies filter inserts were washed twice with warm PBS and fixed in 4 % formaldehyde for 10 min at RT. The membranes were cut out from the filter inserts and kept in 24-well culture plate for the staining process. The HIBCPP cell membranes were permealized through incubation in 0.5 % Triton X-100 with 1 % BSA (w/v in PBS) for 20 min at RT. Between each step of the staining process the membranes were washed thoroughly with PBS. The staining of the HIBCPP cells for cytoskeleton and cell nucleus were carried out for one hour at RT with phalloidin at 1:50 dilution and DAPI at 1: 50.000 dilutions, respectively. Staining of the proteins of interest was achieved through addition of the primary antibodies, directed at them, overnight at 4°C. All primary antibodies were added at a dilution of 1:250. For ZO1, polyclonal rabbit anti-ZO1, for Occludin, polyclonal rabbit anti-Occludin, for E-cadherin polyclonal anti-E-cadherin and for VP1 monoclonal mouse-anti-enterovirus VP1 (Clone 5-D8/1) primary antibodies were added. The secondary antibodies were directed at either rabbit or mouse (polyclonal anti-rabbit IgG Alexa Fluor 488 and 594) and added at 1:250 dilution for one hour at RT in the dark. The membranes were embedded on microscope slides with ProLong Gold Antifade reagent. Images, in particular Z-stacks, were taken with a Zeiss Apotome using a 63x/1.4 objective lens. Images were analysed and manipulated with the Zen software. The creation of Z-stacks allowed immunocytochemical evaluation also from the orthogonal perspective.

4.12. Transmission electron microscopy

Samples for TEM were prepared in our laboratory and send to Dr. Fallier-Becker (Electron microscopy, University of Tübingen) for further analysis. After sequential transmigration experiments, the filters were fixed with 2 % glutaraldehyde + 0.1 M cacodylate buffer (pH 7.4) over night at 4°C. The membranes were cut from the filter inserts using a sharp scalpel and transferred to a 1-5 containing cacodylate buffer. The filters were sent to Tübingen at 4°C. Further fixation was achieved through an one-hour incubation in 1 % osmium tetroxide

(OsO_4) cacodylate buffer. Alternating treatment with ethanol and propyleneoxide was done to cause dehydration of the cell membranes. Before embedding the membranes in Araldite, they were bloc-stained in uranyl-acetate in 70 % ethanol for four hours. The fixed cell layers on the membranes were cut using an ultramicrotome. This enabled cutting of precise slices of 1 µm or 50 nm. The cut segments were stained with lead citrate and analysed with a Zeiss Electron microscope 10 (Em 10).

4.13. Focused ion beam microscopy

Similar to the TEM, samples for the FIB were generated in our laboratory and Dr. Schädler (Zeiss, Oberkochen) carried out the microscopic analysis. The membranes sent for investigation were coated with gold palladium sputter and transferred onto specific scanning electron microscope sample holders. For samples HIBCPP cells + PMN + T lymphocytes + E-30 Bastianni + CXCL 12 voxel sizes of 10 x 10 x 10 nm and for HIBCPP cells + PMN + T lymphocytes + E-30 Bastianni + IL-8 voxel sizes of 8 x 8 x 8 nm were used. Prior to the FIB, we identified regions of interest from similar HIBCPP cells grown on inverted cell culture inserts under a light microscope. This helped at finding possible regions of interest without having to scan the whole cell layer. A gallium FIB-SEM instrument, operating at low voltage (EHT = 1.7 kV), was used for serial sectioning tomography and an energy selective inlens backscattered (EsB) electron detector was used for images with high light contrast at regions of interest. Images or videos were visualized and analysed using the commercial software package ORS Visual SI.

4.14. Statistics

Statistical analysis was performed using the SAS system, release 9.3 (SAS Institute Inc., Cary, USA). For analysis of PMN and T lymphocyte migration rates (Section 5.1 – 5.2), repeated measurements with 3 fixed factors (PMN or T lymphocyte, E-30 infection and cytokine presence) was carried out. This step was performed by the SAS procedure PROC MIXED, which allocated experiment numbers to be a random effect and the conditions (PMN or T lymphocyte, E-30 infection and cytokine presence) to be a fixed effect. For each particular condition ANOVA tests were carried out due to the highly significant interaction terms

(when comparing the different conditions and infection with E-30). In case paired Student´s *t*-test were calculated, it has been indicated on the figures.

Statistical significance for the remaining (Section 5.3 – 5.5) work was calculated with several different models. Dextran flux and TEER (Section 5.3.1) was calculated with the SAS procedure SAS MIXED, where the day of the experiment was taken as the random factor and the different E-30 strain (E-30 Bastianni, 13-311, 13-759 and 14-397) were allocated as fixed factors. To calculate significance for the viral load distribution (Section 5.4) a Poisson-Regression using the Tukey-Kramer comparison was used. Level of significance is indicated with either # or * and results are presented as mean + SD.

5. Results

5.1. Effects of infection with E-30 on cytokine response and immune cell migration across the BCSFB

5.1.1. Barrier integrity and viability of HIBCPP cells following infection with E-30 Bastianni

The ability of E-30 Bastianni to infect HIBCPP cells *in vitro* has previously been shown [36]. In the current study, we adapted a multiplicity of infection (MOI) and duration of infection to a MOI of approximately 0.7 over 28 hours.

Throughout the infection period at 0, 24 and 28h the viability of HIBCPP cells was verified with a LIVE/DEAD® assay (Fig. 20A). We could confirm that the viral infection had no important impact on the viability of the HIBCPP cells (Fig. 20A and B). Thus, we investigated further parameters of barrier integrity such as the TEER and paracellular dextran flux. The experimental set up remained the same and measurements for TEER were performed at 0, 24 and 28h. To assess the permeability for low molecular weight molecules, dextran was added to the upper filter compartment at 24h post infection and measurements of dextran concentration in the lower compartment were taken 4h afterwards. Over the 28h time course the levels of TEER for control HIBCPP cells showed slight increase from 0h to 24h and remained relatively stable until the end of the experiment (Fig. 14). However, a significant decrease in TEER was measured in all infected conditions compared to their respective control (Fig. 14).

The paracellular dextran flux was evaluated through the detection of dextran molecules in the lower compartment after 28h infection and 4h post addition of the sugar to the upper compartment. In control settings, the paracellular permeability of the HIBCPP cells was comparable in all settings with values remaining low (0.31 ± 0.28 % to 0.95 ± 0.87 %) (Fig. 15A). In contrast, the infection with E-30 Bastianni caused a significant ($p<0.0001$) increase in paracellular dextran flux with values rising to 1.01 ± 0.64 % to 1.57 ± 1.23 % (Fig. 15B). In general, the dextran flux remained at tolerable low levels and we could confirm that the barrier integrity was intact even after 28h infection with E-30 Bastianni.

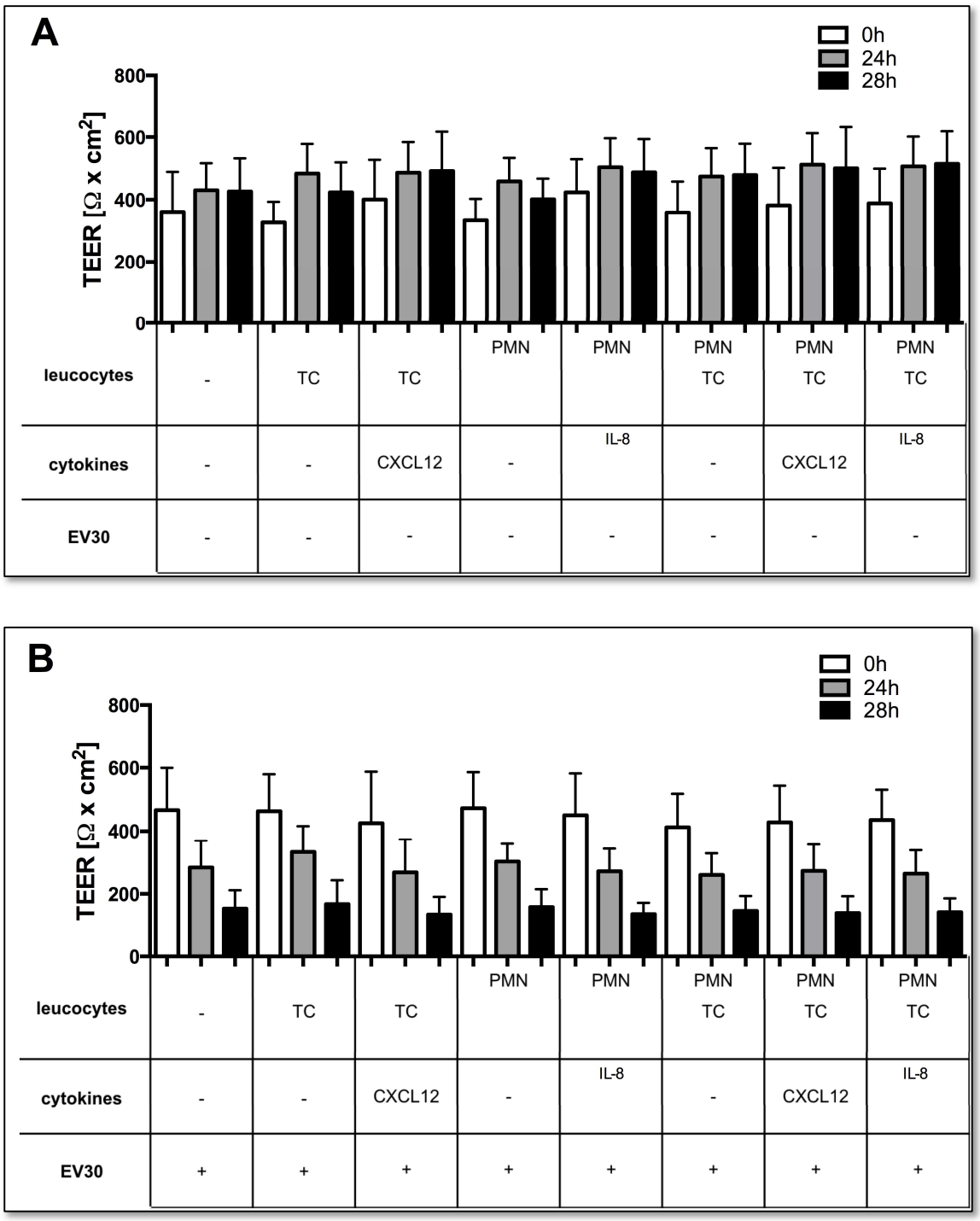

Figure 14. Barrier integrity evaluation through TEER measurement of HIBCPP cells over 28h. Uninfected controls were compared to infected (E-30 Bastianni at MOI 0.7) HIBCPP cells, for infected (A) and uninfected (B) set ups, conditions ± PMN ± $CD3^+$ T lymphocytes ± IL-8 ± CXCL 12, were measured. Measurements were taken at 0, 24, and 28h. Data are shown as mean + SD of 10 independent experiments each performed in triplicates.

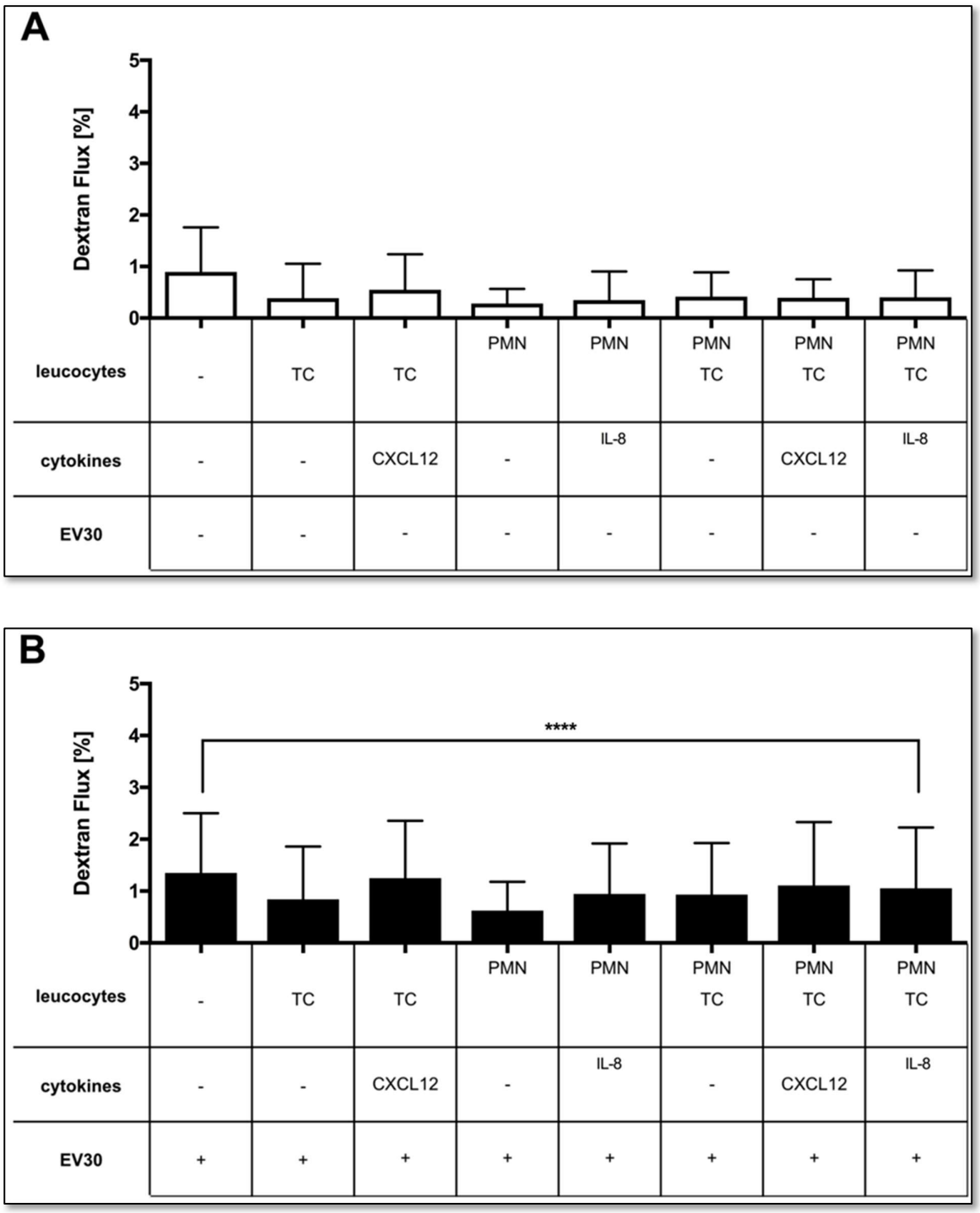

Figure 15. Evaluation of barrier integrity evaluation through measurement of the paracellular dextran flux. Dextran-TexasRed was added to the upper compartment at 24h and measurements from the lower compartment were performed at 28h. The evaluation was carried out for infected (E-30 Bastianni at MOI 0.7) (A) and uninfected (B) condition. For both, all settings ± PMN ± CD3+ T lymphocytes ± IL-8 ± CXCL 12 were analysed. For all settings, the paracellular dextran- TexasRed tracer solution flux across the HIBCPP cells was significantly increased (**** $p<0.0001$) when infected with E-30 Bastianni. Significance was calculated by a 4-factorial ANOVA. Data are shown as mean + SD of 10 independent experiments each performed in triplicates.

5.1.2. Migration of T lymphocytes and PMN across HIBCPP cells

In a healthy human CNS about 70-80 % of all present cells are phenotypic $CD3^+$ memory T cells. The rest of the cellular population consists of PMN, monocytes, natural killer cells, dendric cells, B-cells and perivascular and meningeal mast cells. Following enteroviral infection of the CNS, the movement of PMN into the infected CNS comes prior to a flux of T lymphocytes. Thus, we adapted a previously established set up and analysed sequential migration of two cell types, following infection with E-30 Bastianni [36]. Therefore, the HIBCPP cells were infected with E-30 Bastianni for 24h at a MOI of 0.7. These settings were chosen according to the results obtained from the control experiments on viability and barrier integrity, with the aim to allow inflammatory reactions of the HIBCPP cells without affecting their viability significantly. Moreover, the appropriate chemoattractant, IL-8 for PMN and CXCL 12 for T lymphocytes, were added to the apical cell side to create a chemical gradient towards the CNS side. After the 24h infection period 4 x 10^5 PMN were added to the basolateral cell side, followed by 4 x 10^5 T lymphocytes two hours afterwards. The cells migrated for four (PMN) and two (T lymphocytes) hours respectively followed by evaluation of migration potential.

The evaluation showed that E-30 Bastianni infection of the HIBCPP cells significantly ($p<0.0003$) increased PMN migration in the presence of either IL-8 or CXCL 12 on the apical cell side (Fig. 16A). In addition, we observed a significant ($p<0.0049$) increase in PMN migration after infection with E-30 Bastianni in the set up, where both PMN and T lymphocytes were present without any additional chemokines. T lymphocytes, even though added two hours after the PMN, had a positive effect on the migration of PMN across infected HIBCPP cells leading to higher migration rates (Fig. 16A).

Interestingly, infection of HIBCPP cells with E-30 Bastianni at a MOI of 0.7 for 24h, also led to significantly ($p<0.0001$) enhanced T-lymphocyte migration in the presence of either IL-8 or CXCL 12 on the apical cell side (Fig.16B). The increase in T-lymphocyte migration was also significant ($p<0.0001$) in the presence of PMN if IL-8 and CXCL 12 were added to the apical HIBCPP cell side. The hypothesis that PMN alone would significantly cause an enhanced migration of T lymphocytes was not confirmed. However, an increase in T-lymphocyte

migration was observed in the presence of PMN when the cell layer had been infected with E-30 Bastianni prior to addition of the immune cells ($p<0.0001$) (Fig. 16B).

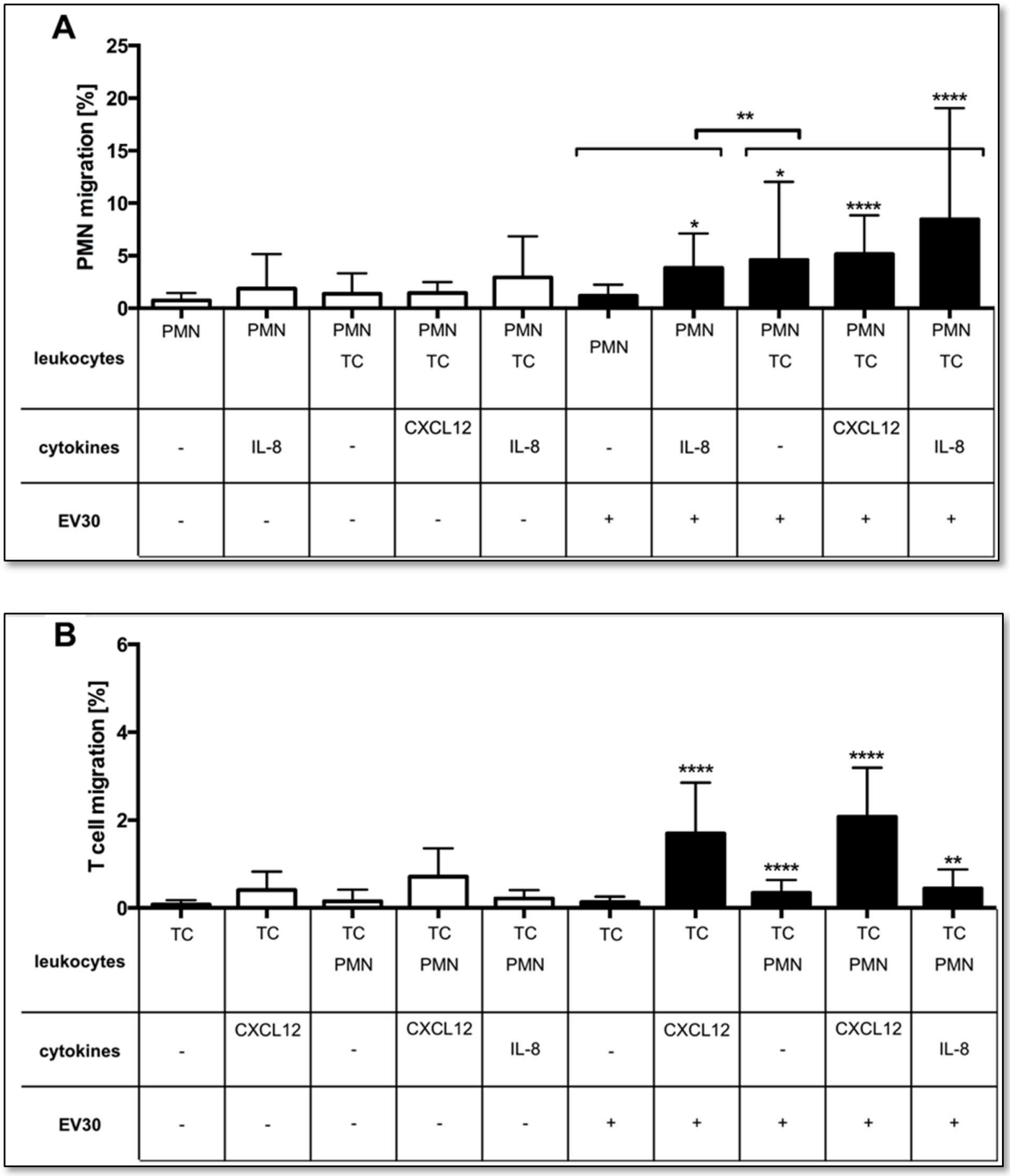

Figure 16. Percentage of transmigration of PMN and T lymphocytes across HIBCPP cells. Uninfected HIBCPP cells (white bars) and infected HIBCPP cells (black bars) were used. HIBCPP cells were infected with E-30 Bastianni at a MOI of 0.7 for 24h prior to the addition of PMN and subsequently T lymphocytes. Statistical significance, comparing infected with their respective uninfected control, was calculated using a 3-factorial ANOVA and indicated through asterisks **** $p<0.0001$, *** $p<0.001$, ** $p<0.01$ and * $p<0.05$. Data are shown as mean + SD of 10 independent experiments each performed in triplicates.

5.2. Polar secretion of cytokines and chemokines by HIBCPP cells

During the migration experiments we focused on IL-8 and CXCL 12 as chemical attractants for the leucocytes due to their well recorded effects on their respective cell type [84]. Nevertheless, our interest laid also with understanding and evaluating a wider range of cytokines and chemokines, which might be involved during the inflammatory response of epithelial cells following enteroviral infection. Therefore, we collected the conditioned media used during the sequential migration experiments and analysed it with a bead-based suspension array. This array allowed the precise determination of cytokine and chemokine concentrations within the media.

A panel of 29 cytokines and chemokines was chosen according to known probable involvement and manufacturer possibilities. A complete list can be found under section 3.8 kits and arrays (cytokine bead array). The detection level of the array was between 0 and 5.000 pg/filter insert (Fig. 17A). The characteristics of secretion of these cytokines was further analysed in the aspect of polar secretion. The direction, either towards the basolateral cell side (blood) or the apical cell side (CNS), plays a key role in determining their possible involvement during enteroviral meningitis.

For the magnetic bead array the cell media was taken both from the basolateral cell side (from within the filter insert, blood side) and the apical cell side (from within the well, CNS side) to allow analysis of possible polar secretion. In total 18 out of the 29 cytokines laid within detectable levels (Fig. 17A), with many found at either end of the spectrum. The detected cytokines were grouped into three categories: (1) Nearly exclusively secreted towards the basolateral cell side (2) predominantly secreted towards the basolateral cell side, but also apically (3) mainly secreted towards the apical side, but also towards the basolateral cell side (Fig. 17B). Out of the detected cytokines, CCL 2, CCL 4, CCL 5, CCL 20, CXCL 10, CXCL 11, GM- CSF, IL-1ra, IL-6, IL-8, IL-12 p40, IL-13 and TNF were detected nearly exclusively on the basolateral side. The group of cytokines predominantly secreted on the basolateral side but also towards the apical cell side consists of CCL 7, CCL 11, INFα 2 and M-CSF. Of the 29 cytokines and chemokines tested only IL-7 was mainly secreted towards the apical HIBCPP cell side.

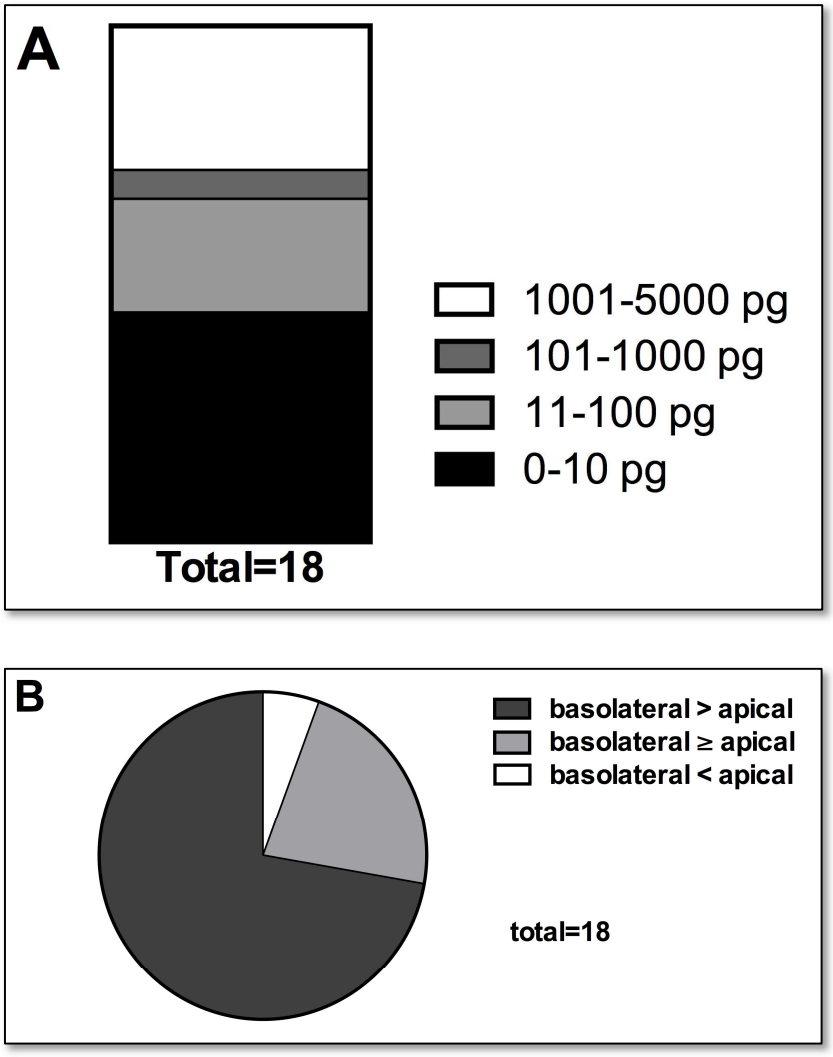

Figure 17. Cytokine and chemokine secretion of HIBCPP cells after 28h infection with E-30 Bastianni. (A) Out of the 29 cytokines tested, 18 reached detectable levels, which ranged from 0 to 5.000 pg/filter insert. (B) The 18 detectable cytokines were grouped into three categories: (1) Nearly exclusively secreted towards the basolateral cell side: CCL 2, CCL 4, CCL 5, CCL 20, CXCL 10, CXCL 11, GM- CSF, IL-1ra, IL-6, IL-8, IL-12 p40, IL-13 and TNF (2) predominantly secreted towards the basolateral cell side, but also apically: CCL 7, CCL 11, INFα 2 and M-CSF (3) mainly secreted towards the apical side, but also towards the basolateral cell side: IL-7. As examples for each of the catergories (1) CXCL 11; (2) M-CSF and (3) IL-7 were chosen to be further illustrated with their exact percentage of apical and basolateral secretion (Fig. 7).

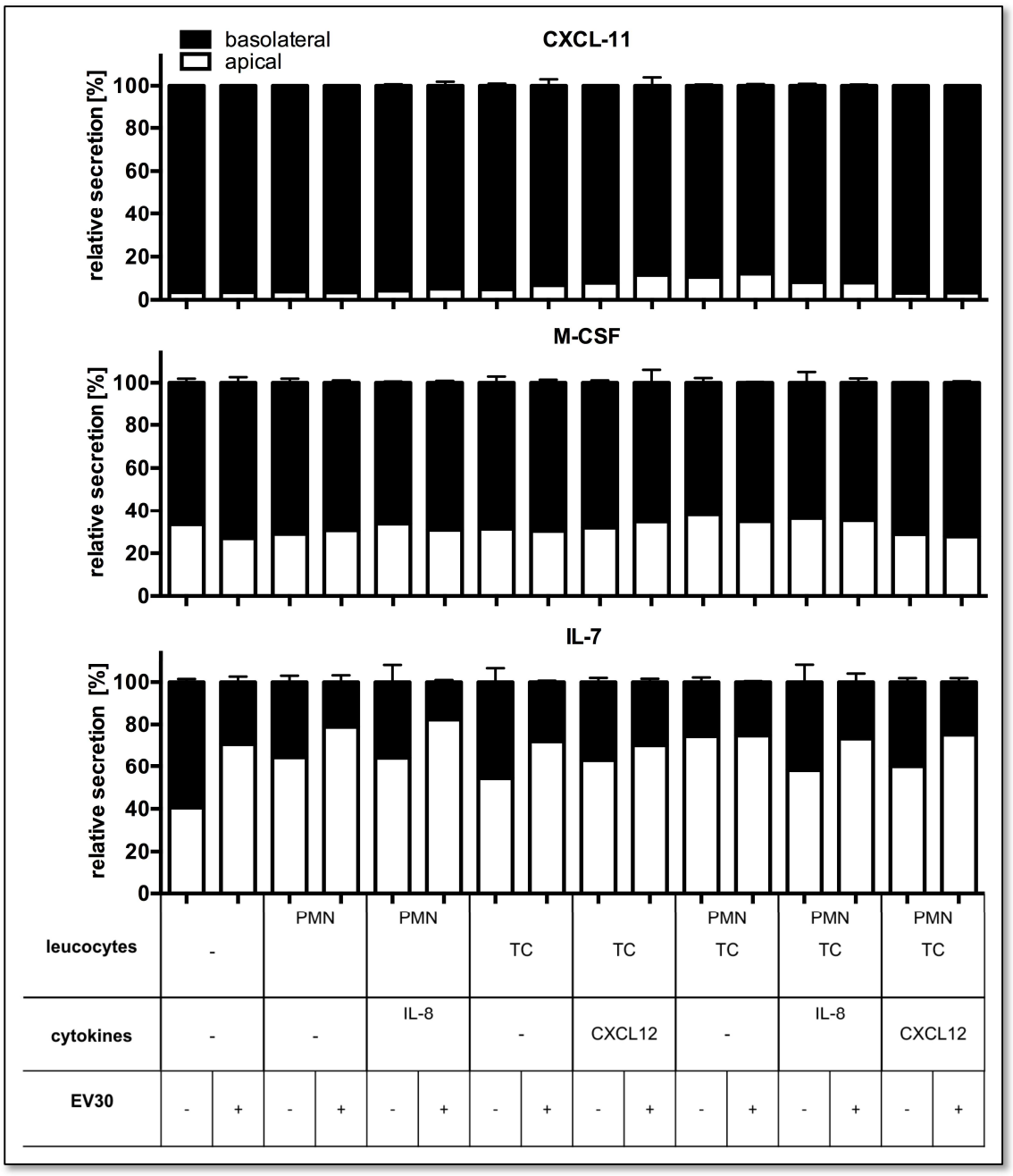

Figure 18. Measurement of polar cytokine secretion of HIBCPP cells after 28h infection with E-30 Bastianni. The media from both the basolateral (filter insert) and apical (well) cell side were collected and cytokine concentrations determined through application of a magnetic bead-based suspension array. CXCL 11 represents group (1), which are nearly exclusively secreted towards the basolateral cell side; M-CSF represents group (2), which are predominantly secreted towards the basolateral cell side and in minor amounts towards the apical cell side; and IL-7 represents group (3), which are mainly secreted towards the apical cell side and in slight amounts towards the basolateral cell side.

5.3. Strain dependent effects of clinical E-30 outbreak isolates at the blood- CSF barrier

5.3.1. Barrier integrity of HIBCPP cells after infection with E-30 Bastianni, 13-311, 13-759 and 14-397

We previously showed that infection of HIBCPP cells with E-30 Bastianni at a MOI of 0.7 up to 28 hours had no important impact on epithelial cell viability or leucocytes viability but did influence paracellular permeability and TEER. To extend this knowledge onto the three outbreak strains, we carried out infections of HIBCPP cells with E-30 Bastianni in comparison with three outbreak strains, 13-311, 13-759 and 14-397, over 28 hours and measured any effects on barrier integrity.

The TEER measurements were taken at 0, 5, 24 and 28h; and values obtained from uninfected control HIBCPP cells were compared to the infected layers. As confirmation from the results obtained in the sequential transmigration experiments, the TEER of the control HIBCPP cells remained constant (at around 400 Ω^2 x cm^2) or showed a slight increase over the 28h time course. For the E-30 strains 13-759 and 14-397 the pattern was comparable to control HIBCPP cells (Fig 19A). The significant decrease in TEER after infection with E-30 Bastianni had previously been confirmed, but also the strain 13-311 caused similar results. The TEER values decreased significantly ($p<0.0001$) compared to their control already after 24h, to 183 ± 86 and 285 ± 64 Ω x cm, respectively. A further significant ($p<0.0001$) reduction of the TEER, compared to their respective control, occurred until 28h post infection when values, of E-30 Bastianni and E-30 13-311 infected cell layers, reached 128 ± 64 and 193 ± 40 Ω^2 x cm^2 (Fig. 19A).

The paracellular permeability of the HIBCPP cells infected with the four E-30 strains was evaluated through measurement of dextran flux across the cell layer between the 24 and 28h infection time course. The dextran movement from the basolateral to the apical cell side over 4h was significantly ($p= 0.0020$) increased (2.30 ± 1.46%), compared to uninfected control (0.94 ± 1.06%), only with HIBCPP cells infected by E-30 Bastianni. The infection of HIBCPP cells with E-30 13-311 (1.18 ± 1.31%), 13-759 (0.63 ± 0.90%) or 14-397 (0.45 ± 0.42%) did not trigger a significant increase in paracellular dextran flux (Fig. 19B).

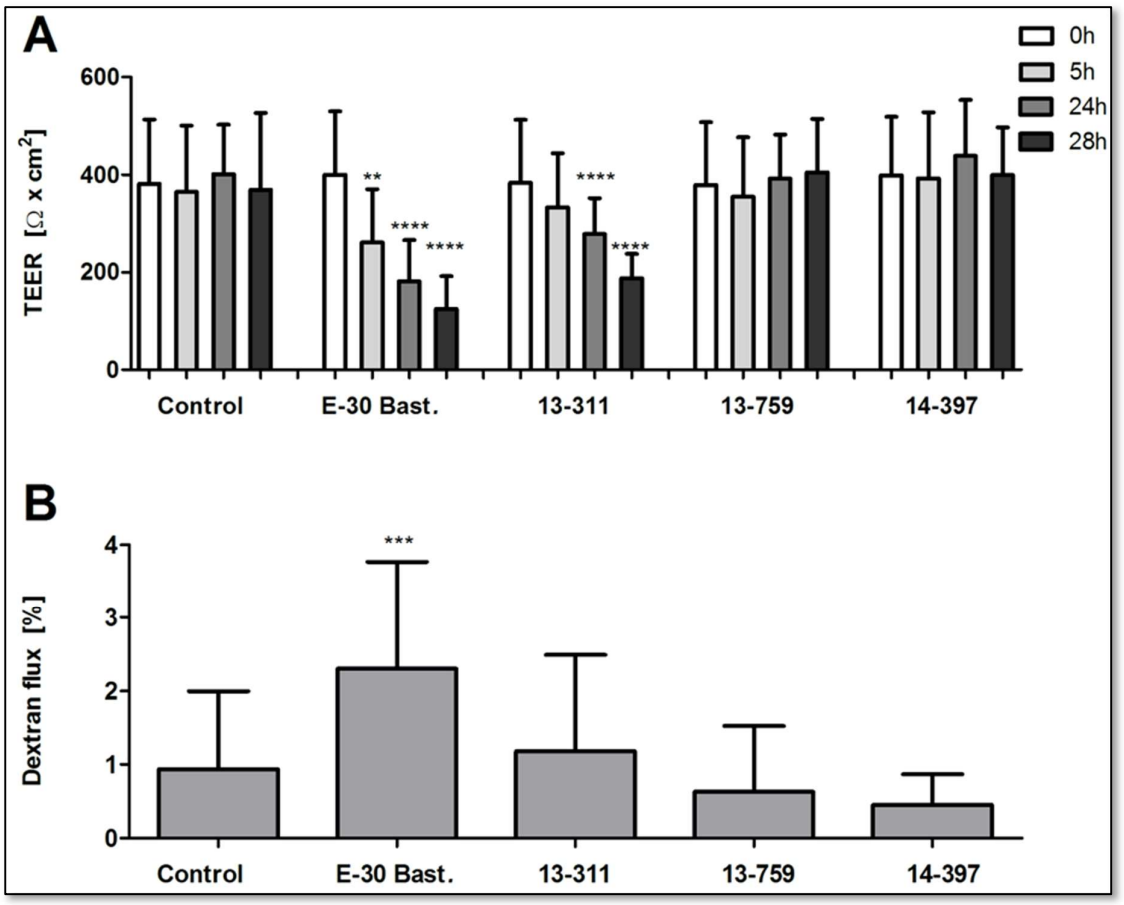

Figure 19. E-30 strain-dependent impact on the barrier integrity of HIBCPP cells. The evaluation was carried out through measurements of the TEER and the paracellular dextran flux. (A) The HIBCPP cells were infected with E-30 Bastianni, 13-311, 13-759 and 14-397 and TEER measurements were taken at 0h (white bars), 5h (light grey bars), 24h (dark grey bars) and 28h (black bars). The values of TEER were represented as Ω x cm² and p values were obtained through comparison of the TEERs after 5, 24 and 28h to their respective 0h TEER value. Significance was calculated using Dunnett test followed by a Post-hoc-test and indicated through asterisks **** $p<0.0001$, ** $p<0.01$. Data are shown as mean + SD of 11 independent experiments each carried out in triplicates. (B) The paracellular permeability for the low molecular weight (3000kDa) molecule dextran-TexasRed was measured over four hours starting after 24h infection. The HIBCPP cell were infected with E-30 Bastianni, 13-311, 13-759 and 14-397 and 24h post infection dextran was added to the basolateral (filter insert) cell side. After four hours, the amount on the apical (well side) cell side was quantified and represented as percentage of the total. P value (***$p < 0.001$) was obtained when the values from E-30 Bastianni infected HIBCPP cells were compared to the three outbreak strains (13-311, 13-759 and 14-397) and the uninfected control. Data are shown as mean + SD of 5 independent experiments each carried out in triplicates.

5.3.2. E-30 strain specific cytotoxic effects on HIBCPP cells and impact on cell viability

Based on the observations made during barrier integrity analysis of HIBCPP cells after infection with E-30 Bastianni, 13-311, 13-759 or 14-397, we focused on the impact of infection on viability of the HIBCPP cells and possible cytotoxic effects of the viral strains. The viability was verified through a live/dead assay after 28 hours of infection (Fig. 20A). The principles of the live/dead assay are explained in detail under section 4.2.3 Determination of cell viability. The results were recorded as photographs with a fluorescence microscope. Evaluation of viability of HIBCPP cells after 28 hours of infection with E-30 showed no significant increase in dead cells (stained red) for any of the strains.

To assess possible cytotoxic effect of the viral strains on the HIBCPP cells by a second assay, we performed a lactate dehydrogenase assay. The principles are explained in detail under section 4.2.4 Evaluation of cytotoxicity. The levels of lactated dehydrogenase in the media is directly proportional to the percentage of dead or damaged cells and can be colorimetrically represented and measured. The HIBCPP cells were infected for 28h at a MOI of 0.7 with four E-30 strains and LDH-release into the cell media was measured (Fig. 20B). The analysis of cytotoxic effects of each strain on HIBCPP cells showed no significant impact of any strain on the human brain epithelial cells. All strains elicited minor cytotoxic effects when compared to uninfected control, with all values remaining below 5% of the total.

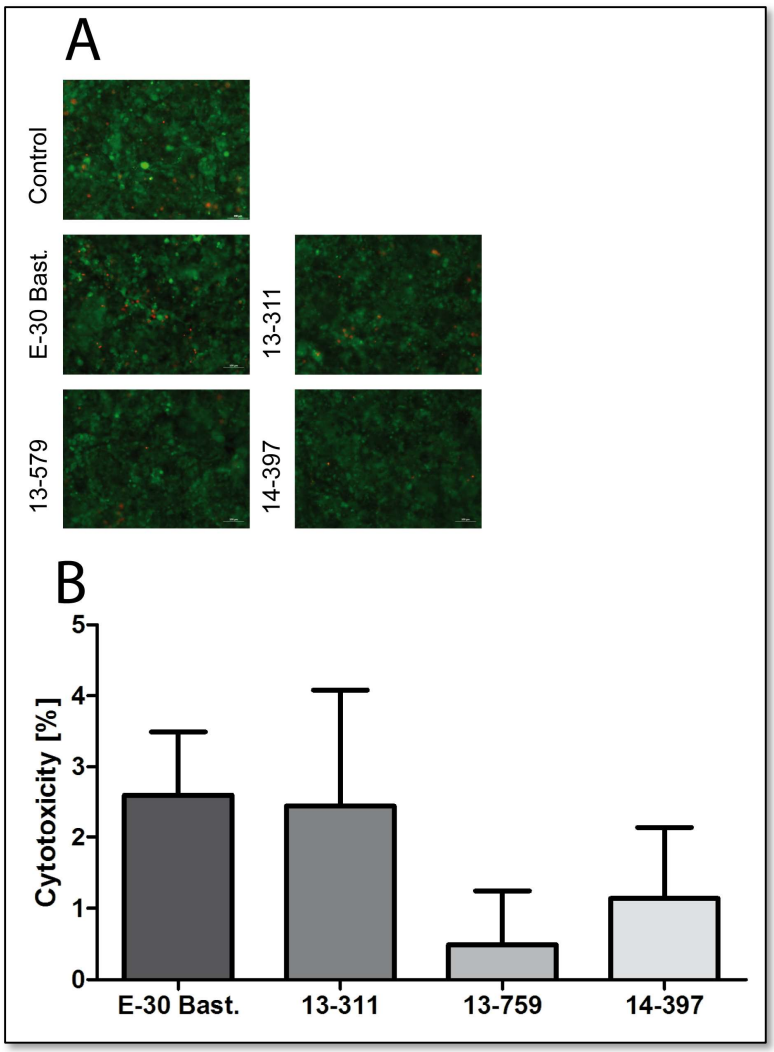

Figure 20. E-30 strain specific cytotoxic effects on HIBCPP cells and impact on their viability. (A) Live/dead assay of HIBCPP cells after 28h infection with E-30 Bastianni, 13-311, 13-759 or 14-397 compared to uninfected control. The images were taken with a x20 lens on a fluorescent microscope. Shown here are representative images of four independent experiments each carried out in triplicates. (B) LDH release into the cell culture media following infection with all four E-30 strains was measured after 28h infection and calculated as a percentage of the negative (100 % release) control. Values from uninfected control were used to set 0 and are not represented on the chart. Data are shown as mean + SD of four independent experiments each performed in triplicates. Technical triplicates were used during the analytical evaluation.

5.3.3. E-30 strain dependent effect on tight junction and adherens junction morphology

As we observed E-30 strain specific effects on the barrier integrity, both the TEER measurements and paracellular dextran flux, we focused our attention towards possible morphological changes to the tight and adherens junction proteins. These complex cell-to-cell connection proteins are a major reason for epithelial cell layers, here the HIBCPP cells, to create and maintain an intact and functioning network. The significantly lower TEER measured with E-30 Bastianni and 13-311 after 28-hour infection raised the question, whether the decreased electrical resistance causes visible alteration to the junctional proteins. Based on previous observations made in the laboratory and publications on viral impact on epithelial and endothelial cells (REF) we chose the tight junction proteins ZO1 and Occludin and the adherens junction protein E-cadherin. TJ and AJ are known to be located at the apical and basolateral cell sides of polar epithelial cells, which was confirmed for HIBCPP cells through microscopic analysis with an orthoscopic view (Fig. 21, 22 and 23). The HIBCPP cells were infected with E-30 Bastianni, 13-311, 13-759 and 14-397 at a MOI of 0.7 for 28 hours and stained for the protein of interest (ZO1, Occludin or E-cadherin), HIBCPP cell nuclei, HIBCPP cell cytoskeleton and the viral protein (VP) 1. The VP1 staining allowed to accurately distinguish between infected (VP1 staining found within the cytosol of the epithelial cells) HIBCPP cells or uninfected (no VP1 staining in the epithelial cells) HIBCPP cells. The staining of DAPI and the cytoskeleton of HIBCPP cells did not get affected under any condition (Fig. 21, 22 and 23).

As for ZO1 staining, a very regular “honeycomb-like” pattern can be observed (Fig. 21). The same regular and undisrupted staining can be seen for HIBCPP cells infected with either E-30 13-759 or 14-397. However, for HIBCPP cells infected with E-30 Bastianni or 13-311 the staining of ZO1 was majorly disrupted. These extensive disruptions were focused on cell-to-cell borders of infected HIBCPP cells (Fig. 21). When two adjacent HIBCPP cells were not infected by E-30, no alteration to the ZO1 morphology was visible. For the second TJ protein, Occludin, the observations made were comparable to ZO1. Again, the protein staining of Occludin on uninfected HIBCPP cells was in a regular pattern and undisrupted (Fig. 22).

The infection with strains E-30 13-759 and 14-397 had no visible effect on the morphology of Occludin. The staining, even between two or several infected HIBCPP cells, remained

comparable to control. In strong contrast, when HIBCPP cells were infected with E-30 Bastianni or 13-311, the staining for Occludin was extensively disrupted (Fig. 22). The staining for the TJ protein was interrupted or completely absent between infected neighbouring HIBCPP cells. For the AJ protein E-cadherin staining of uninfected control, and E-30 13-719 and 14-397 infected HIBCPP cells were comparable (Fig. 23). The basolateral staining can be found alongside the HIBCPP cellular body.

The staining for E-cadherin on HIBCPP cells infected with E-30 Bastianni was disrupted between infected cells. However, infection with 13-311 caused only minor morphological disruption to the protein staining. For all conditions (Fig. 21, 22 and 23) infection with E-30 did not cause any visible alterations to the HIBCPP nuclei (Column 1, blue) or cytoskeleton staining (Column 2, yellow).

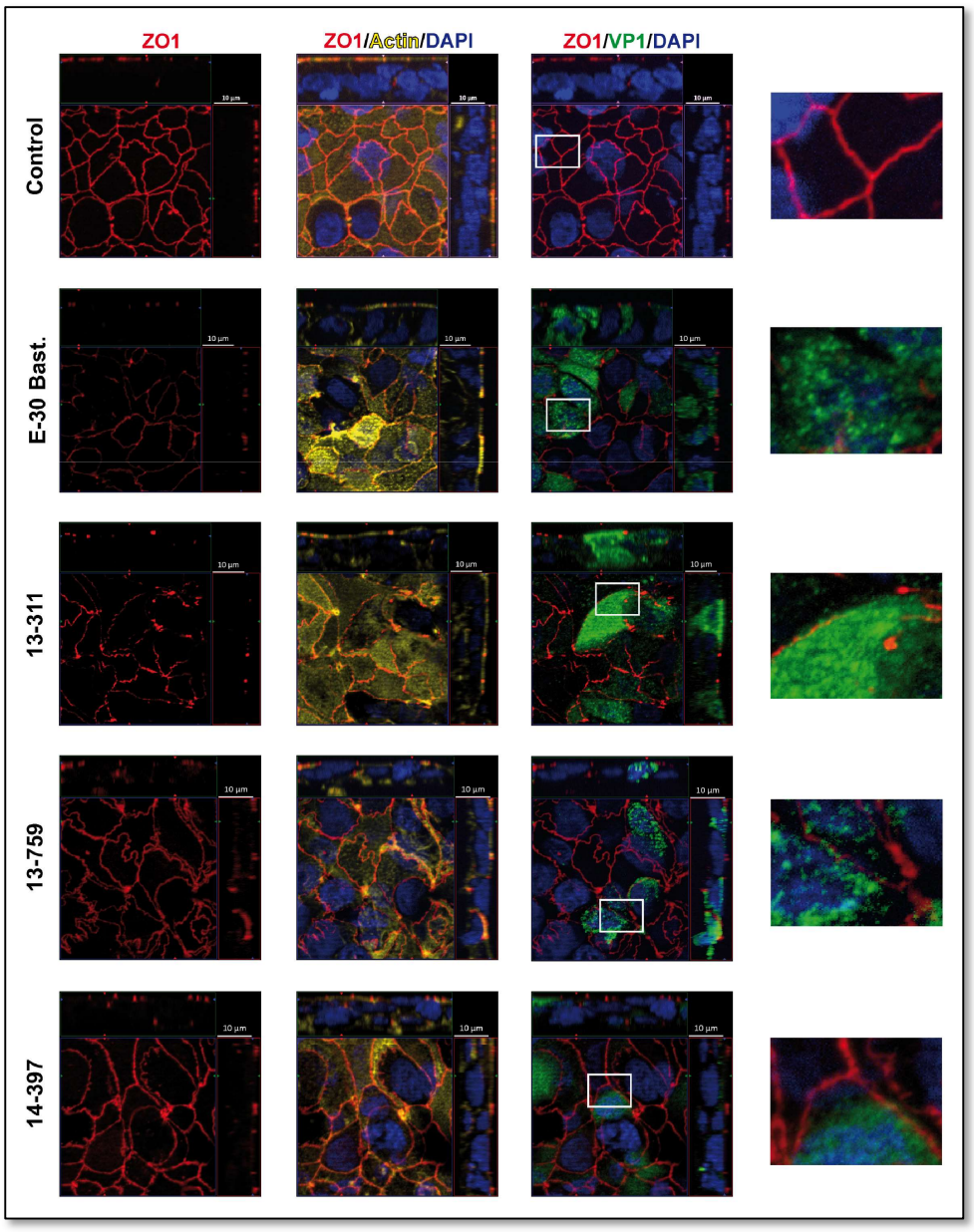

Figure 21. E-30 strain specific effects on ZO1 morphology. HIBCPP cells were infected with E-30 Bastianni, 13-311, 13-759 and 14-397 at a MOI of 0.7 for 28 hours and compared to uninfected HIBCPP cells. Through the application of an Apotome, on a fluorescent microscope, we created Z-stacks, which were represented with a two-dimensional view onto the apical HIBCPP cell side and a cross-section through the z-plane of numerous slices. The cell layers were oriented so that the apical HIBCPP cell sides were facing "up" and "right" and the basolateral cell sides were facing "down" and "left". The filter membranes were stained for the TJ protein ZO1 (red), the viral capsid protein VP1 (green), the HIBCPP cell nuclei DAPI (blue) and the HIBCPP cell F-actin (yellow). For enhanced visible analysis, the images were arranged in four columns: column 1- only ZO1 staining, column 2- ZO1 in combination with DAPI and the cytoskeleton, column 3- ZO1 in combination with DAPI and VP1 and column 4- a zoomed in frame of images from column 4 (frame of interest was indicated with a white box). For column 4 a representative frame was selected and 400 times enlarged. The different settings, control and four E-30 strains, were arranged vertically. Shown here are representative images chosen from manifold Z-stacks, from six independent experiments each performed in triplicates.

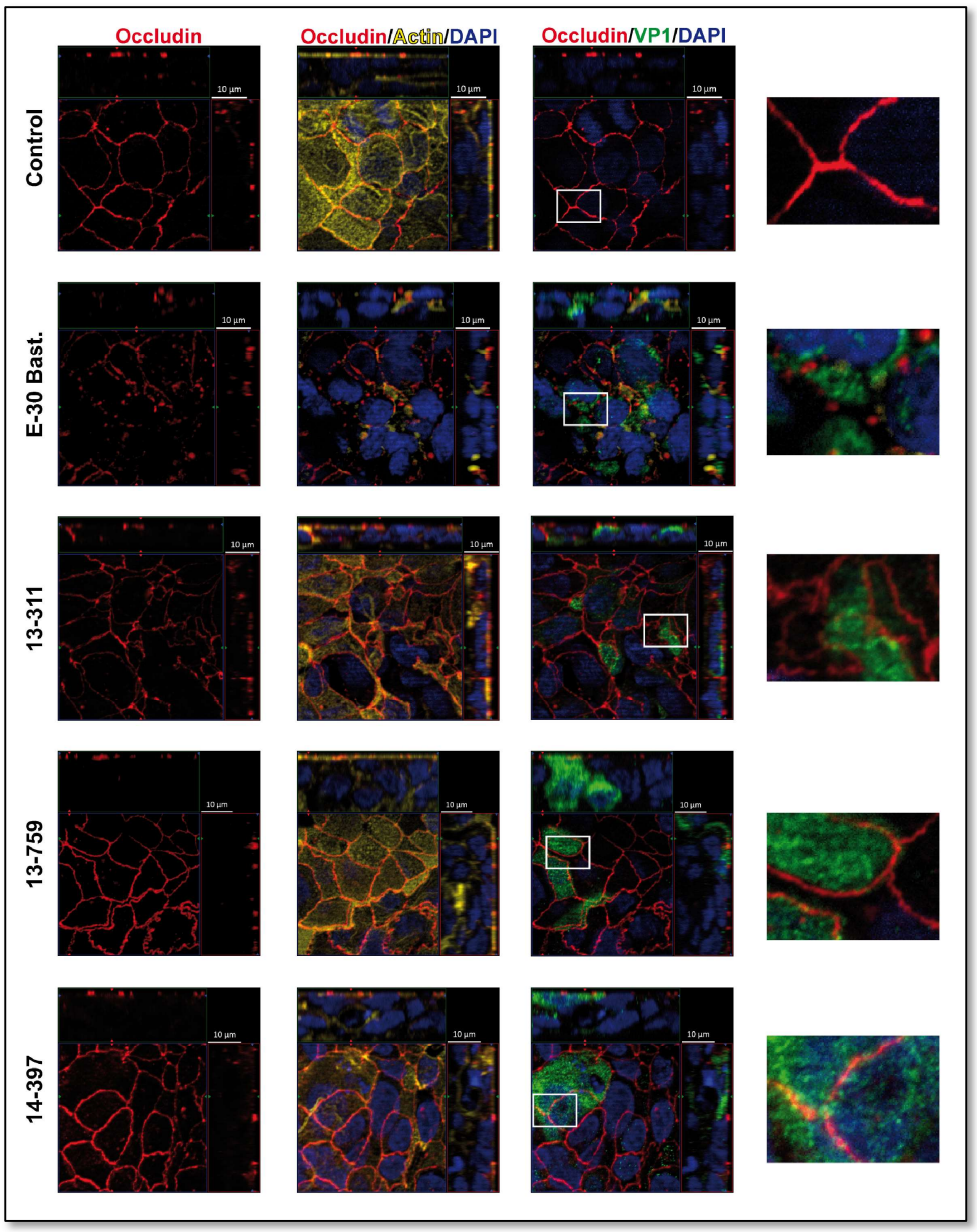

Figure 22. E-30 strain specific effects on Occludin morphology. HIBCPP cells were infected with E-30 Bastianni, 13-311, 13-759 and 14-397 at a MOI of 0.7 for 28 hours and compared to uninfected HIBCPP cells. Through the application of an Apotome, on a fluorescent microscope, we created Z-stacks, which were represented with a two-dimensional view onto the apical HIBCPP cell side and a cross-section through the z-plane of numerous slices. The cell layers were oriented so that the apical HIBCPP cell sides were facing "up" and "right" and the basolateral cell sides were facing "down" and "left". The filter membranes were stained for the TJ protein Occludin (red), the viral capsid protein VP1 (green), the HIBCPP cell nuclei DAPI (blue) and the HIBCPP cell F-actin (yellow). For enhanced visible analysis, the images were arranged in four columns: column 1- only Occludin staining, column 2- Occludin in combination with DAPI and the cytoskeleton, column 3- Occludin in combination with DAPI and VP1 and column 4- a zoomed in frame of images from column 4 (frame of interest was indicated with a white box). For column 4 a representative frame was selected and 400 times enlarged. The different settings, control and four E-30 strains, were arranged vertically. Shown here are representative images chosen from manifold Z-stacks, from six independent experiments each performed in triplicates.

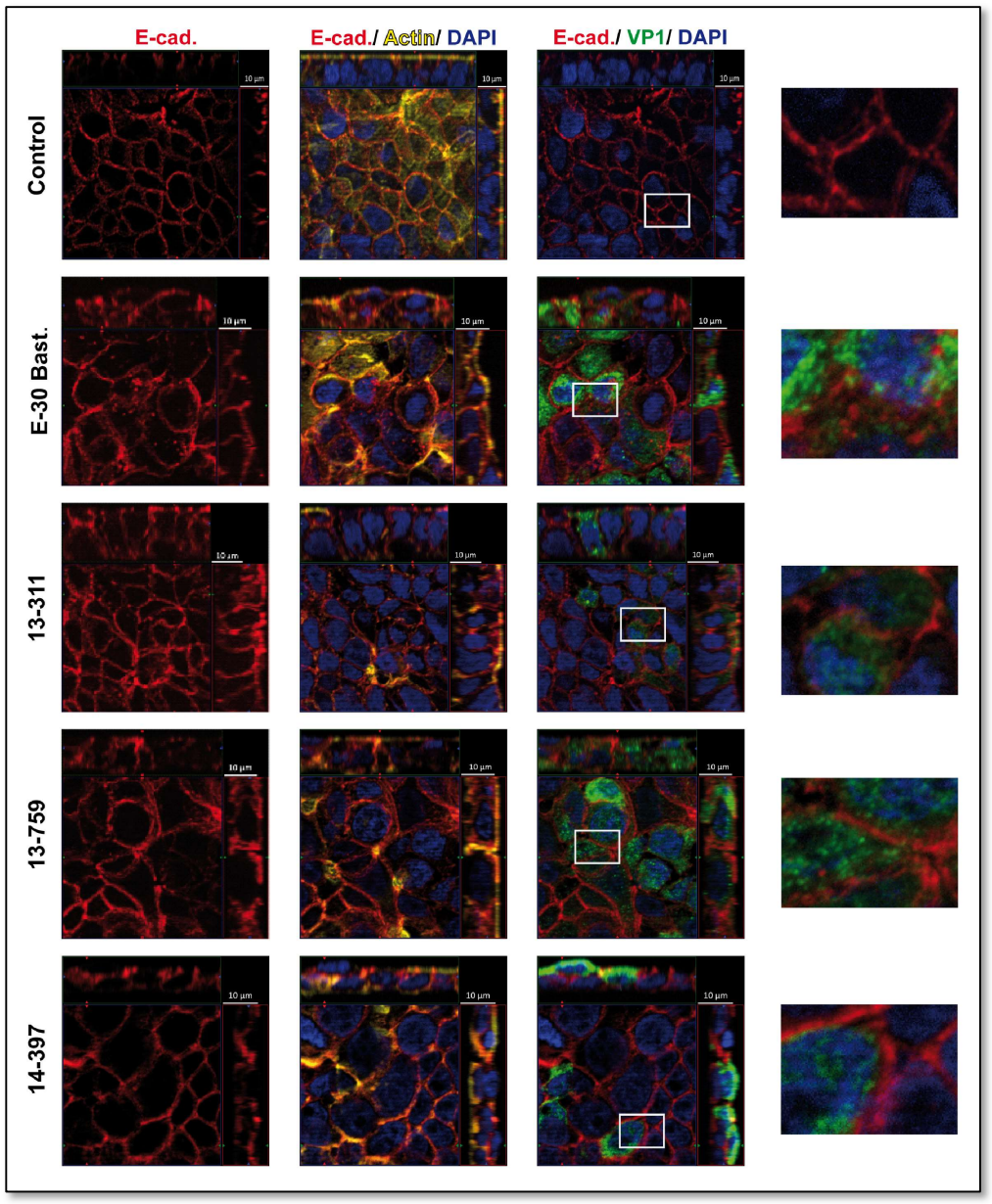

Figure 23. E-30 strain specific effects on E-cadherin morphology. HIBCPP cells were infected with E-30 Bastianni, 13-311, 13-759 and 14-397 at a MOI of 0.7 for 28 hours and compared to uninfected HIBCPP cells. Through the application of an Apotome, on a fluorescent microscope, we created Z-stacks, which were represented with a two-dimensional view onto the apical HIBCPP cell side and a cross-section through the z-plane of numerous slices. The cell layers were oriented so that the apical HIBCPP cell sides were facing "up" and "right" and the basolateral cell sides were facing "down" and "left". The filter membranes were stained for the TJ protein E-cadherin (red), the viral capsid protein VP1 (green), the HIBCPP cell nuclei DAPI (blue) and the HIBCPP cell F-actin (yellow). For enhanced visible analysis, the images were arranged in four columns: column 1- only E-cadherin staining, column 2- E-cadherin in combination with DAPI and the cytoskeleton, column 3- E-cadherin in combination with DAPI and VP1 and column 4- a zoomed in frame of images from column 4 (frame of interest was indicated with a white box). For column 4 a representative frame was selected and 400 times enlarged. The different settings, control and four E-30 strains, were arranged vertically. Shown here are representative images chosen from manifold Z-stacks, from six independent experiments each performed in triplicates.

5.3.4. Tight and adherens junction protein expression analysis

The morphological alterations of junctional proteins observed during the immunofluorescence studies led to the question, whether the protein amount or their localization within the HIBCPP cells may vary. Standard western blots and western blots with the soluble and membrane HIBCPP fractions were performed (Fig. 24A and B). The standard western blots suggest that the protein expression of ZO1, Occludin and E-cadherin was not altered due to infection with any of the E-30 strains (Fig. 24A). Protein analysis of the membrane and cytosolic fraction indicate that, despite infection with E-30, the protein localization did not alter (Fig. 24B).

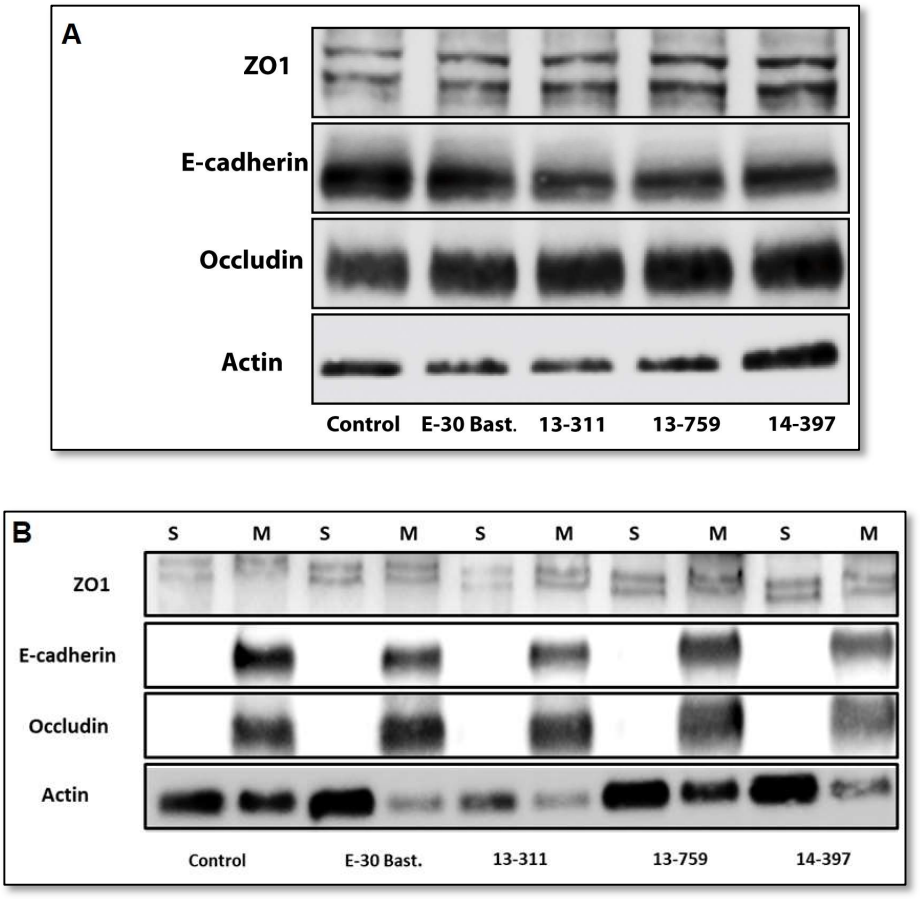

Figure 24. Western blot analysis of junctional proteins after E-30 infection. Protein analysis of HIBCPP cells after 28 hours of infection with E-30 Bastianni, 13-311, 13-759 and 14-397. TJ proteins ZO1 (220 kDa) and Occludin (65 kDa), and AJ protein E-cadherin (120 kDa) were investigated with actin (42 kDa) used as a loading and expression control. (A) Blot of total protein lysate of HIBCPP cells. Experiments were carried out in triplicates and a representative blot, from 6 independent experiments, was used for illustration. (B) HIBCPP cells were chemically separated into membrane (M) and soluble (S) fraction. Experiments were carried out in triplicates and a representative blot, from 2 independent experiments, was used for illustration.

5.3.5. Immunofluorescence analysis of T lymphocyte and PMN migration pathway

Due to the previously observed strain specific alterations to the junctional proteins of HIBCPP cells, we continued with an investigation into a possible variation in migration pathway of leucocytes across an infected epithelial cell layer. The known pathways of immune cells across the BBB or the BCSFB into the CNS are para- and transcellular migration. To differentiate between the pathways, we carried out large scale analysis, applying several different methods and tools aimed at discovering leucocytes during their migration across the epithelial cell layer. We carried out immunofluorescence analysis in our laboratory; transmission electron microscopy and focused ion beam analysis was performed by collaborative laboratories (see section 4.12 and 4.13). All images were taken after 28 hours infection period with E-30 Bastianni at a MOI of 0.7 and a four hours migration period for PMN and two hours for T lymphocytes. Migration was stimulated by the addition of IL-8 and CXCL 12 to the apical HIBCPP cell side.

We focused on the prototypic strain, as it caused the most extensive barrier impairment of HIBCPP cells and compared it to leucocyte migration across uninfected HIBCPP cells. Suggestions of possible migration pathways were made depending on the location of the stained PMN and T lymphocytes in relation to the actin skeleton and nucleus of HIBCPP cells (Fig. 25). Throughout our microscopic analysis we discovered both cell types using both pathways and decided on representative images to be illustrated in the figure. The continuous staining of the actin skeleton surrounding the PMN (Fig. 25C and D) and T lymphocytes (Fig. 25A&B and E&F) indicated that the cells are within the epithelial cells and therefore moving transcellularly. Paracellular migration, identified by a continuous connection of intercellular actin reaching the apical HIBCPP cell side, was identified for both PMN and T lymphocytes. Another feature to identify paracellular migration was a continuous actin staining of an elongated PMN pushing through two HIBCPP cells (Fig. 25C and D). The tip of the PMN is squeezing between two HIBCPP cell borders, which is an indication of paracellular movement. Identification of transcellular movement of immune cells was based on the lack of enclosing actin cytoskeleton and their distance to the HIBCPP cell membranes (Fig. 25G and H). The migrating PMN is found in clear distance to HIBCPP cell membranes and without surrounding actin staining; it was therefore considered as transcellular movement.

The IF analysis has proven to be an useful tool for analysis of migration pathways of immune cells across epithelial cell layers, however, to allow a more confident assessment, further studies including more precise methods were applied.

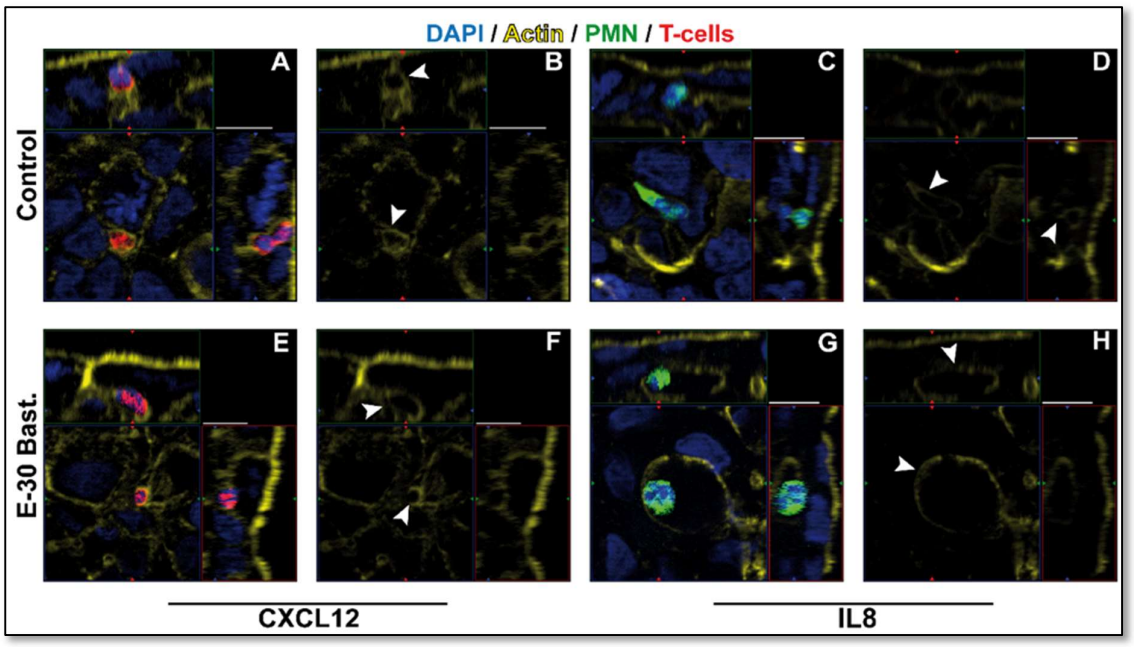

Figure 25. Immunofluorescent analysis of PMN and T lymphocyte migration pathway across HIBCPP cells. Pre-stained PMN (green) and T lymphocytes (Red) were analysed according to their location within the HIBCPP cell layer. After 28 hours of infection with E-30 Bastianni, the layers were stained for nuclei with DAPI (blue) and actin skeleton with phalloidin (yellow). Images pairs represent the complete frame (A, C, E and G) and the same frame with neither leucocytes nor nuclei staining and small white arrows indicating the most important features of the actin skeleton. Illustrated here are images taken for each of the following experimental set ups: HIBCPP cells + PMN and T-lymphocytes + CXCL 12 = A, B; HIBCPP cells + PMN and T-lymphocytes + E-30 Bastianni + CXCL 12 = E, F; HIBCPP cells + PMN and T-lymphocytes + IL-8 =C, D; HIBCPP cells + PMN and T-lymphocytes + E-30 Bastianni + I-L8 = G, H. Shown here are representative images of three independent experiments each carried out in duplicates and analysed with at least four Z-stacks per filter membrane.

5.3.6. Transmission electron microscopy analysis of leucocyte migration pathway

To substantiate the results obtained with immunofluorescence analysis of migrating leucocytes across the BCSFB and to gain further insight into cellular processes involved, also in relation to barrier impairment through infection with E-30, we carried out electron microscopic analysis. For this purpose, the same experimental set up was chosen and we were able to confirm that both cell types use both para- and transcellular migration pathways across HIBCPP cells (Fig. 26).

Both PMN (Fig. 26A&B and C&D) and T lymphocytes (Fig. 26E&F and G&H) were captured during their migration process. From the representative images chosen for the figure, a 400x

enlargement of an area of interest was added to show more precise cellular processes. Paracellular movement of a PMN from the basolateral to the apical HIBCPP cell side was shown (Fig. 26A). The elongated PMN moving towards the apical (CNS) cell side is localised in line with the TJ. The intact TJ between two neighbouring HIBCPP cells and the tip of the elongated PMN in close proximity to the cell-to-cell connection can be seen in the enlargement (Fig. 26B). PMN migrating transcellularly can be identified through the interruption of its cellular membrane (indicated with small black arrows), which extends towards the apical side of the HIBCPP cell indicating its direction of movement (Fig. 26D). The PMN is located close to the basolateral side of the HIBCPP cell (early phase of migration) and is moving towards the luminal side (Fig. 26C). Transcellular migration of T lymphocytes was also validated (Fig. 26E&F and G&H). The T lymphocyte has already migrated across the HIBCPP cells and is located at the apical HIBCPP cell side. The migrating cell is in clear distance to intact TJs found between HIBCPP cells (Fig. 26E). It is still attached to the HIBCPP cell through a thick actin filament (Fig. 26F). For the second migrating T lymphocyte, it is not as clear whether the para- or transcellular route was taken (Fig. 26G). The cell is just exiting the epithelial cell layer in clear distance to intact TJ connections. The connection with the HIBCPP cell is slightly less advanced as in images E and F (Fig. 26H). The electron microscopy allows an investigation of the migration pathway in detail, however the images recorded are two-dimensional and therefore we also studied the migration pathways through focused ion beam.

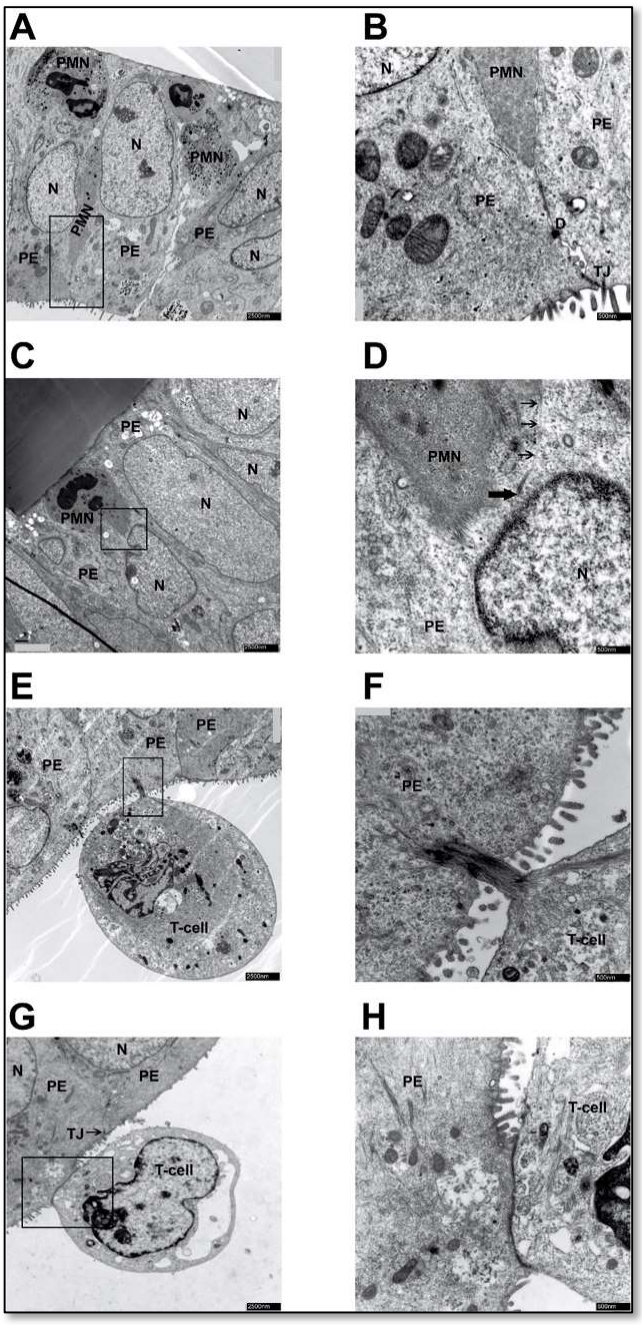

Figure 26. Transmission electron microscopic analysis of immune cell migration pathway across HIBCPP cells. Two-dimensional representation of leucocyte migration across the HIBCPP cells. The left column (A, C, E and G) are images which show larger frames, including a more complete view of the cell layer and the right column (B, D, F and H) are zoomed in areas of interest. Images from the left column have a scale bar of 2500 nm, for zoomed in images from the right column the scale bar represents 500nm. Illustrated here are images taken for each of the following experimental set ups: HIBCPP cells + PMN and T-lymphocytes + CXCL 12 = A, B; HIBCPP cells + PMN + T lymphocytes + E-30 Bastianni + CXCL 12 = C, D & G, HIBCPP cells + PMN + T lymphocytes + E-30 Bastianni + IL-8 = E, F. The images are orientated so that the apical HIBCPP cell side (identified through the presence of microvilli) is either down or right. The small black arrows indicate the cell membrane and the thick black arrow shows the termination of the membrane (E and F). N= plexus epithelial cell nucleus; PE= plexus epithelial cell; D= desmosome; PMN= polymorphonuclear neutrophil; TJ= tight junctions.

5.3.7. Focused ion beam microscopy analysis of leucocyte migration pathway

We could validate that PMN and T lymphocytes use both para- and transcellular migration pathways across the HIBCPP cells through IF and TEM analysis. To allow the creation of a three-dimensional representation and moving images (videos) of the migrating leucocytes, we carried out focal ion beam microscopy (Fig. 27). We investigated the migration of PMN and T lymphocytes under the same experimental conditions as previously: HIBCPP cells + PMN + T lymphocyte + E-30 Bastianni + IL-8 (A and B); HIBCPP cells + PMN + T lymphocytes + E-30 Bastianni + CXCL 12 (B and C). We chose representative freeze-frames from recorded videos and show a migrating PMN (Fig. 27A&B) and a T lymphocyte (Fig. 27C&D). The PMN is squeezing through a filter membrane pore and is entering the HIBCPP cell layer from the basolateral side (Fig. 27A&B). The white arrow heads indicate where two cell membranes, from the PMN and from the neighbouring HIBCPP cells, are located side by side. The arrows point directly at the tricellular borders, which are formed by the paracellular migration process of the immune cell. The PMN is creating intracellular gaps by pushing the neighbouring HIBCPP cells apart to move towards the apical cell side. This process, including the presence of intact cellular membranes of both PMN and HIBCPP cells, is a clear indication for paracellular movement. The transcellularly migrating T lymphocyte across the infected HIBCPP cells is found imbedded into the epithelial cell layer (Fig. 27C and D). In contrast to the processes involved during the paracellular movement of the PMN, we can see the immune cell being in clear distance to the HIBCPP cell junction complex, while it moves from the basolateral to the apical HIBCPP cell side (white arrow heads). The three-dimensional representation of leucocyte migration across an infected epithelial cell layer confirmed previous findings and produced even more detail on the process.

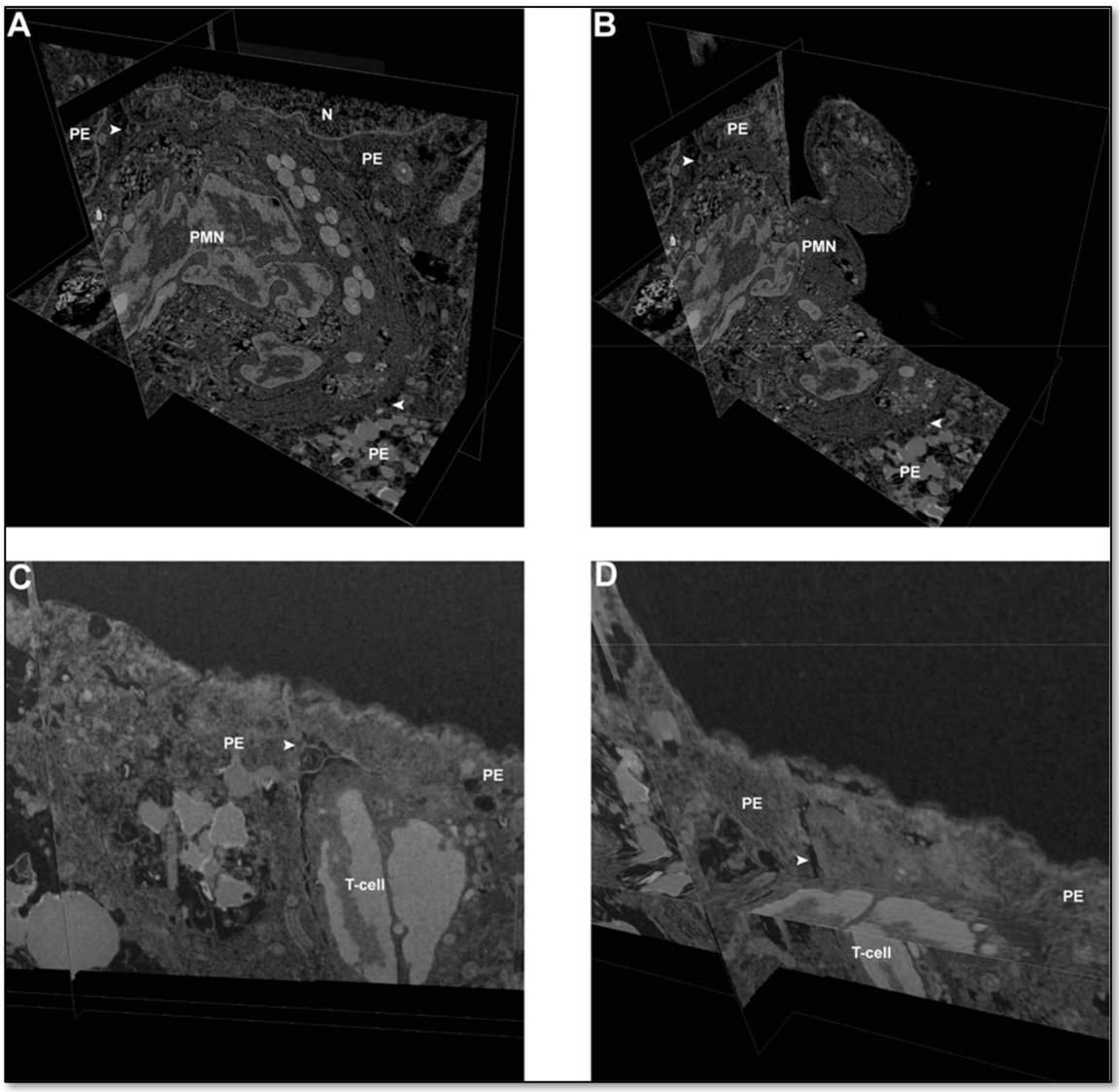

Figure 27. Focused ion beam analysis to determine migration pathways of immune cells across HIBCPP cells. HIBCPP cells were infected for 28 hours and sequential migration of PMN and T lymphocytes recorded through focal ion beam microscopy. Illustrated here are freeze-frame images taken for each of the following experimental set ups: HIBCPP cells + PMN + T lymphocytes + E-30 Bastianni + IL-8 = A and B; HIBCPP cells + PMN + T lymphocytes + E-30 Bastianni + CXCL 12 = C and D. Paracellular migration of a PMN from the basolateral to the apical side of HIBCPP cells can be seen (A and B). The small white arrows indicate the cellular gaps between the PMN and neighbouring HIBCPP cells. The "hourglass" shape of the PMN is caused as the PMN squeezes through a filter membrane pore (B). The transcellularly moving T lymphocyte is in clear distance from cell borders and membranes; the white arrow shows where the cell is moving through the HIBCPP cell. N= plexus epithelial cell nucleus; PE= plexus epithelial cell; PMN= polymorphonuclear neutrophil.

5.4. E-30 strain characterisation and behaviour in HIBCPP and RD cells

5.4.1. E-30 strain specific replication in HIBCPP and RD cells

The barrier impairment of HIBCPP cells caused by two E-30 strains, Bastianni and 13-311, in contrast to no detectable impairment caused by 13-759 and 14-397 was analysed further in relation to possible causes related to replication efficacy. The replication of viral pathogens varies depending on their genetic code and host cell. Therefore, we investigated the replication rates of E-30 Bastianni, 13-311, 13-759 and 14-397 in HIBCPP cells and as a control we also analysed their replication rates in RD cells. The control cell line was chosen due to their wide spread use in enteroviral propagation and maintenance. Thus, it was not surprising that the overall replication rates of all four strains were much higher in RD cells compared to HIBCPP cells (Fig. 28A and B). After 24 hours infection, E-30 Bastianni showed the highest replication rate and viral copies per ml overall in both cell types; the outbreak strains had comparable low levels. The increase in viral copies was calculated in relation to the starting amount (Fig. 28A and B)

The pattern of viral replication within the two cell lines varies (Fig. 28A and B). After 5 hours replication in RD cells the pattern was comparable to replication after 5 hours in HIBCPP cells. The Bastianni strain was standing out with much higher levels compared to similar low levels of the outbreak strains. After 24 hours infection period, however, also the outbreak strains reached similar viral copy numbers in RD cells (Fig. 28A and B). To further characterise the replication and passage of the viral strains in and across HIBCPP cells, we analysed via the measurement of viral genome copies the localisation of the viral particles (Fig. 29).

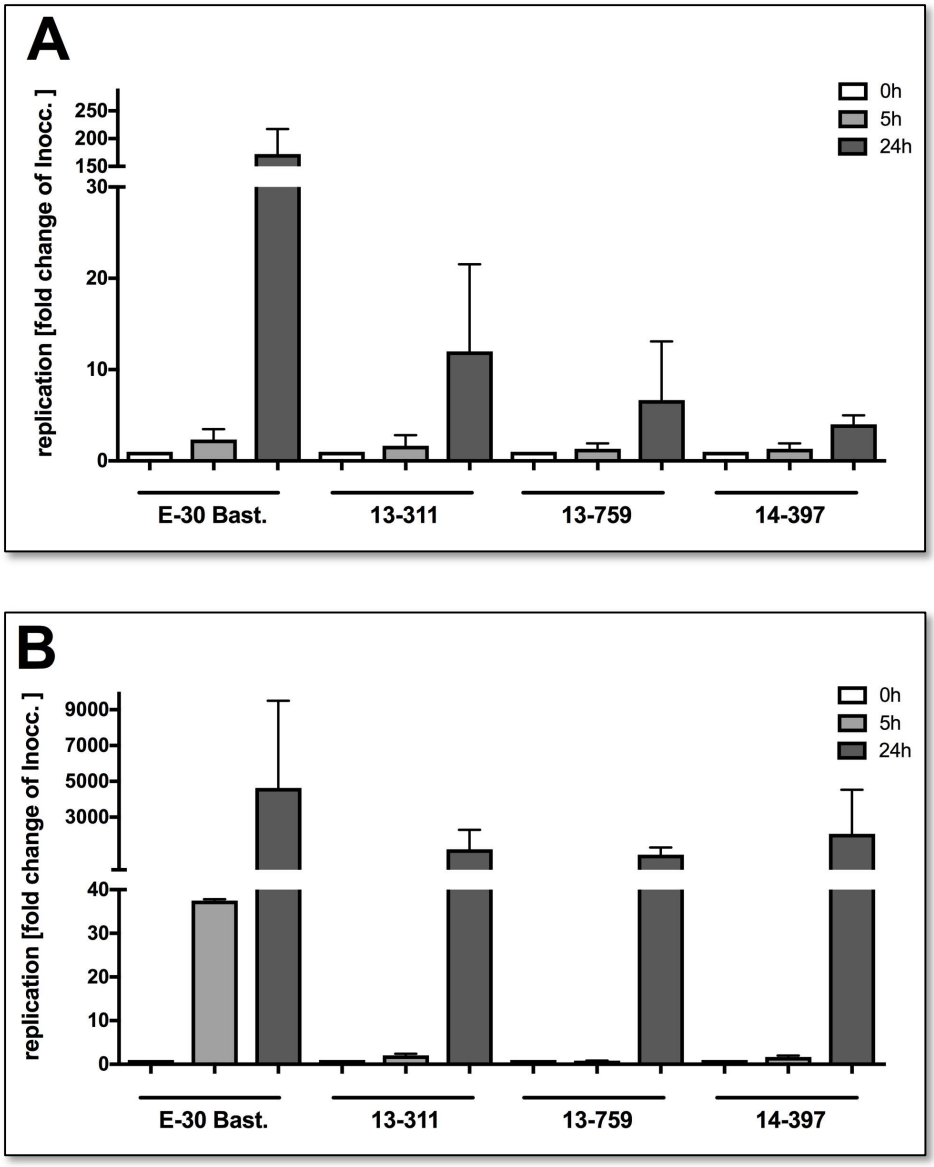

Figure 28. E-30 strain- specific replication pattern in HIBCPP and RD cells. Both HIBCPP (A) and RD (B) cells were infected for 24 hours and the total viral copies were determined after 0, 5 and 24 hours. For replication in HIBCPP cells, the values were calculated from 3 independent experiments performed in triplicates and shown as mean + SD. For replication in RD cells, the values were calculated from four independent experiments carried out in triplicates and shown as mean + SD.

5.4.2. E-30 dissemination within the in vitro cell culture system

The inverted *in vitro* cell culture system allows the determination of viral concentration in different compartments of the set up. An infection experiment was performed as previously described and at specific time points the viral concentration in the filter compartment, within the cells and in the cell compartment were measured (Fig. 29A).

After 5 hours of infection at a MOI of 0.7 all strains had very minor amounts of viral genome copies within the HIBCPP cells or already passaged across them to the apical cell side (Fig. 29B). For the outbreak strains viral genome copies were found nearly exclusively on the basolateral side, where they were added at the beginning of the experiment. However, for E-30 Bastianni already after 5 hours an important fraction, 33 ± 18 %, of the total viral genome copies was found within the HIBCPP cells (Fig. 29B). After 24 hours of infection with E-30, the pattern of viral dissemination was more similar to each other. For E-30 Bastianni 20 ± 15 % of viral genome copies were found on the basolateral side, 49 ± 10 % within the HIBCPP cells and 31 ± 11 % had passaged across the layer. For 13-311 35 ± 7 % of viral copies were still found on the basolateral side, already 47 ± 7 % were in the cell lysate and 17 ± 1 % were found on the apical HIBCPP cell side. For 13-759 37 ± 2 % were detected on the basolateral cell side, 47 ± 6 and 16 ± 8 % had passaged to the apical cell side. The final outbreak strain, 14-397, stands apart from the others with 72 ± 18 % still located on the basolateral side, only 12 ± 12 % of copies within the HIBCPP cells and 16 ± 9 % on the apical cell side. For E-30 Bastianni, 13-311 and 13-759 a progress of infection can be noted from 5 to 24 hours. However, for 14-397 the pattern of viral copies remains comparable (Fig. 29B).

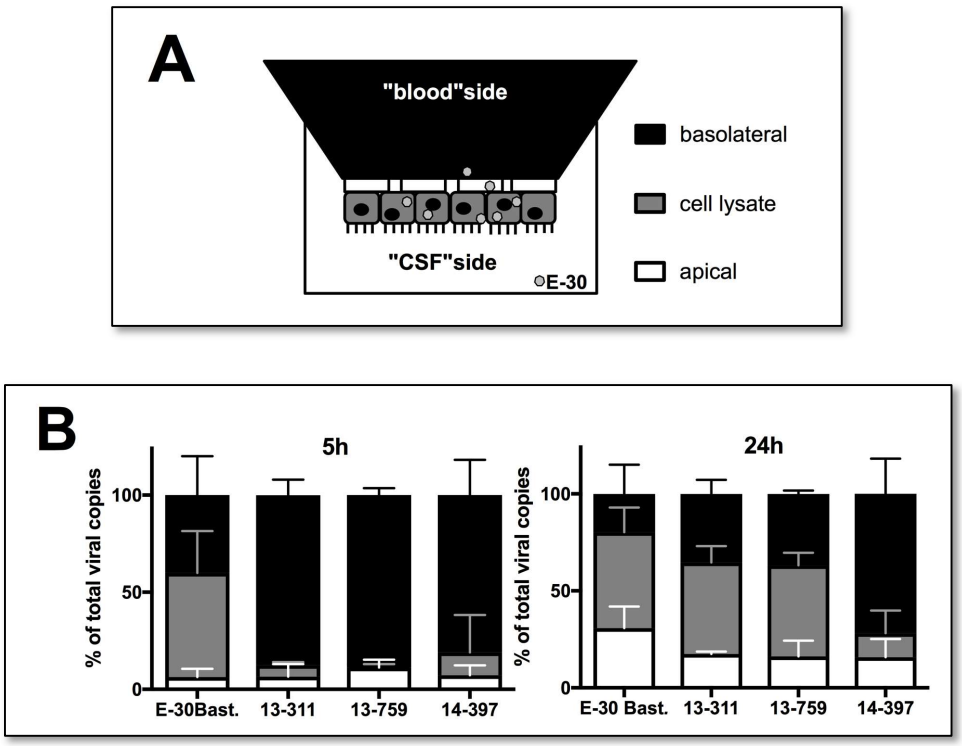

Figure 29. Strain dependent variation in viral dissemination. HIBCPP cells were infected with E-30 Bastianni, 13-311, 13-759 and 14-397 and viral copies were measured at 5 and 24 hours. (A) Schematic diagram of the experimental in vitro set up, where the colours black (basolateral), grey (cell lysate) and white (apical) correspond to the bar chart below. (B) The supernatant from both the basolateral HIBCPP cell side and the apical HIBCPP cell side were measured. Also, the HIBCPP cells attached to the filter membrane were lysed (to release all viral particles) and analysed for their viral particle amount. Percentages were calculated from total amount of viral particles measured. Data are shown as mean + SD of three independent experiments each performed in triplicates.

5.4.3. Verification of virulence of E-30 strains after passage across the HIBCPP cells

The virus copies which have been detected in the well compartment (apical HIBCPP cell side) can be either virus copies from the original inoculum or viral progeny. To verify that the virus maintains its virulence despite passage across the HIBCPP cells, we transferred the cell free supernatant harvested from the lower part of the well after a 28 h infection experiment onto monolayer of RD cells (Fig. 30 schematic set up). We could show that all strains remained virulent after passage across the HIBCPP cells (Fig. 30).

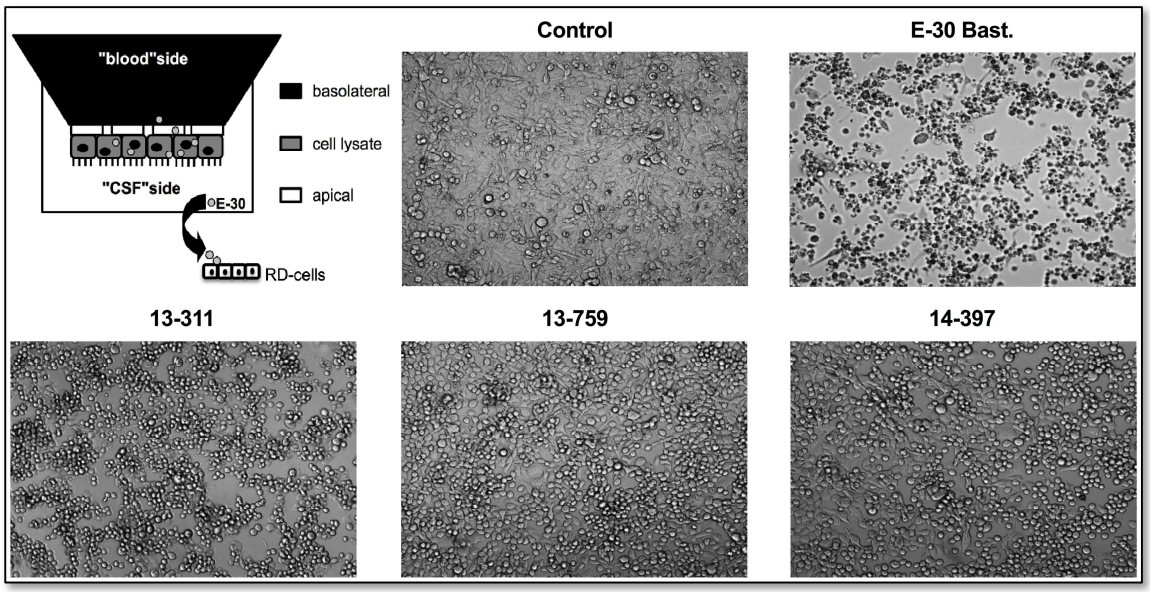

Figure 30. E-30 strains remain virulent after passage across HIBCPP cells. The cytopathic effect (rounding off and detachment) of the RD cells is clearly visible for all strains compared to uninfected control. Infected RD cell monolayers were analysed under a light microscope and images taken. Images are taken from 2 independent experiments carried out in triplicates and a representative image for each strain was illustrated.

5.4.4. E-30 infection quantification in HIBCPP and RD cells

We noticed that the different E-30 strains infect various amounts of HIBCPP cells. Based on this observation and to gain further insight into the conceivable explanations for the alterations at the BCSFB with consequent barrier impairment, we quantified the amount of infected HIBCPP cells after 28 hours of infection at MOI of 0.7. The infection experiment was carried out as previously stated with all E-30 strains. When comparing the number of infected HIBCPP cells by the outbreak strains to Bastianni, a significant ($p < 0.0001$) increase was calculated (Fig. 31). E-30 Bastianni infected 0.7047 ± 0.3615 % HIBCPP cells compared to 0.1279 ± 0.1020 % for 13-311, 0.0894 ± 0.0966% for 13-759 and 0.0463 ± 0.0547 % for 14-397. Strain 13-311 infected significantly ($p < 0.0001$) more cells than 14-397 (Fig. 31).

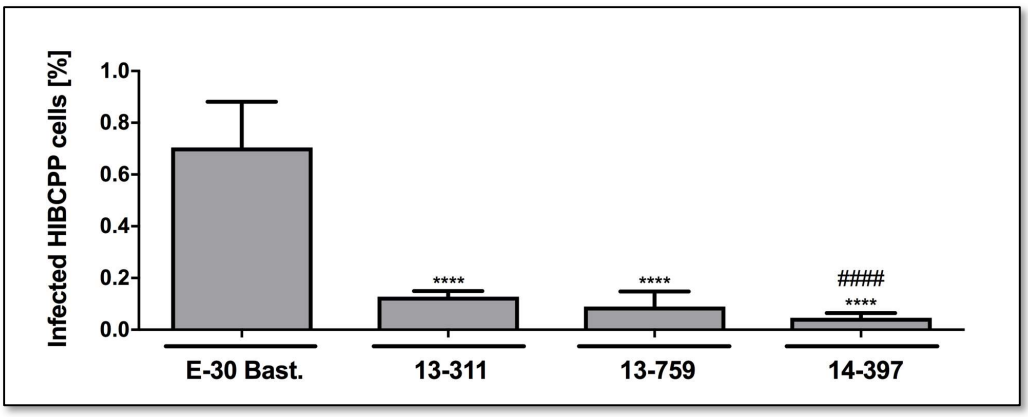

Figure 31. Strain specific amount of infected HIBCPP cells. After infection with E-30 Bastianni, 13-311, 13-759 and 14-397 HIBCPP cells were stained for DAPI and VP1 to allow identification of infected and uninfected cells. Percentage of infected cells was calculated in relation to the complete cell layer. Data are illustrated as mean + SD and were calculated from three independent experiments performed in duplicates. 10 fields of view per filter were counted to enable exact extrapolation. Significance ****p < 0.0001 was calculated for amount of infected HIBCPP cells by E-30 Bastianni compared to all outbreak strains and ####p < 0.0001 for evaluation of 13-311 against 13-759 and 14-397.

5.5. Bioinformatic analysis of the genetic code of E-30 strains

5.5.1. Differences in genome sequences of E-30 strains

The phenotype of a virus is determined by its genetic code and variations may explain differences in characteristics between them. To allow comparison of the E-30 strains used for this project we first had to determine their genetic sequences. Therefore, the strains E-30 Bastianni, 13-311, 13-759 and 14-397 were sequenced and then, using bioinformatic tools, aligned to allow exact comparison of each amino acid. The full genomes of the outbreak strains were compared to each other and to Bastianni in terms of similarities for nucleotides and amino acids (Fig. 32).

Between the outbreak strains we discovered 83.4 - 99.1 % nucleotide and 96.6 - 99.5 % amino acid similarity. When comparing E-30 Bastianni to the outbreak strains 81.1 – 81.6 % of nucleotides and 96.0 – 96.4 % of amino acids corresponded to the outbreak strains. To further compare the sequences of E-30 Bastianni to the outbreak strains and emphasize the differences, we identified several clusters on the polyprotein sequences, where amino acid variations were of higher frequency. The locations of these clusters were mainly at 15-24, 573-655, 690-725, 831-886 and 1043-1157 amino acid positions of the P1 and P2 regions (Fig.32). Furthermore, alignment of the polyprotein sequences showed numerous point

mutations between the different E-30 strains. Comparison of the outbreak strains between each other brought forward an interesting sequence difference. The outbreak strain E-30 13-759 showed important differences in amino acid sequences when compared to E-30 13-311 and 14-397 with 70 and 74 different amino acids. However, in strong contrast, when comparing E-30 13-311 and 14-397 only 10 amino acids were different between them (Fig. 32).

A

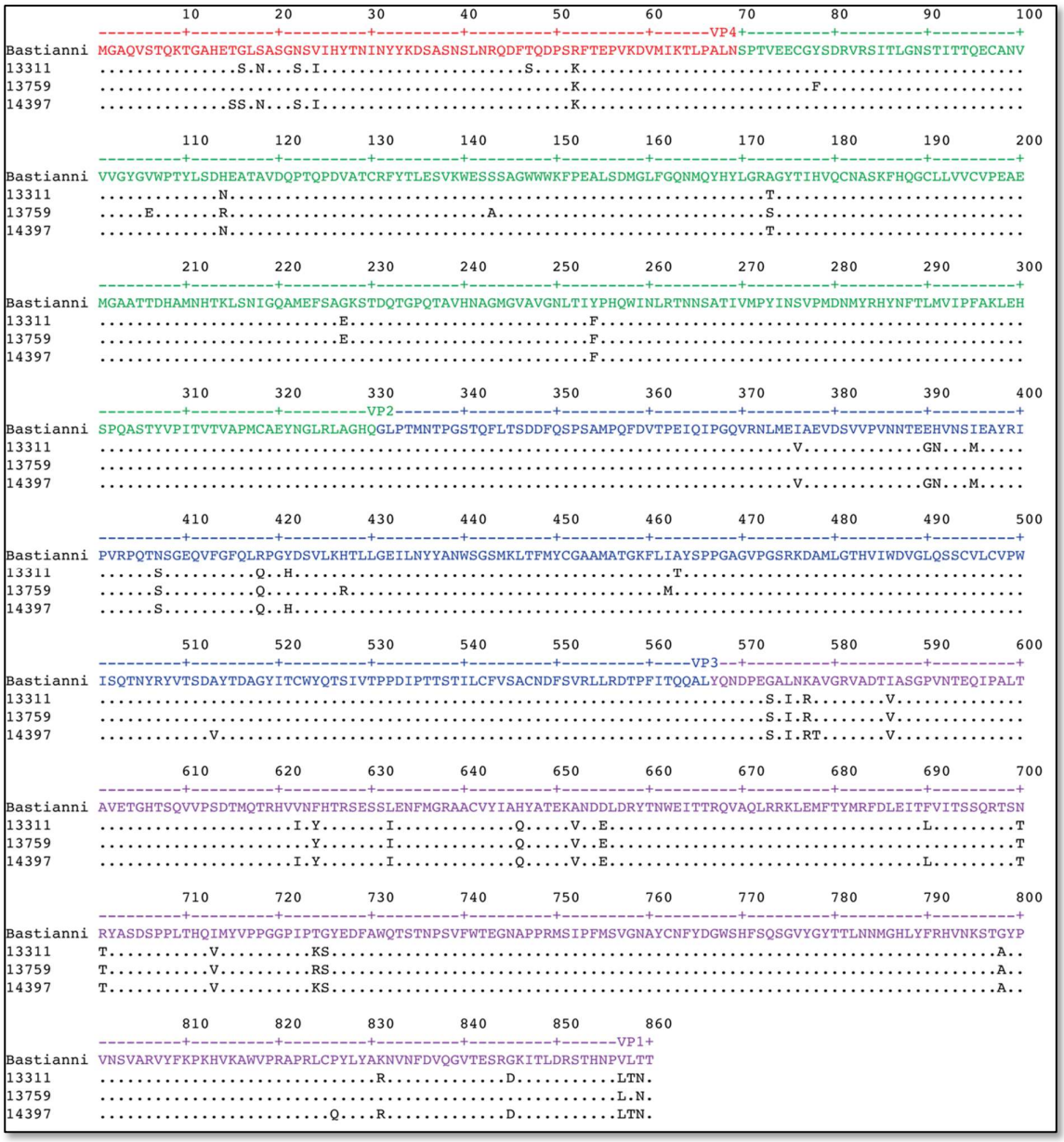
10 20 30 40 50 60 70 80 90 100
VP4
Bastianni MGAQVSTQKTGAHETGLSASGNSVIHYTNINYYKDSASNSLNRQDFTQDPSRFTEPVKDVMIKTLPALNSPTVEECGYSDRVRSITLGNSTITTQECANV
13311 .....S.N...S.I.....S....K.....
13759 .....K.....F.....
14397 .....SS.N...S.I.....K.....
110 120 130 140 150 160 170 180 190 200
Bastianni VVGYGVWPTYLSDHEATAVDQPTQPDVATCRFYTLESVKWESSSAGWWWKFPEALSDMGLFGQNMQYHYLGRAGYTIHVQCNASKFHQGCLLVVCVPEAE
13311 .....N.....T.....
13759 .....E.....R.....A.....S.....
14397 .....N.....T.....
210 220 230 240 250 260 270 280 290 300
Bastianni MGAATTDHAMNHTKLSNIGQAMEFSAGKSTDQTGPQTAVHNAGMGVAVGNLTIYPHQWINLRTNNSATIVMPYINSVPMDNMYRHYNFTLMVIPFAKLEH
13311 .....E.....F.....
13759 .....E.....F.....
14397 .....F.....
310 320 330 340 350 360 370 380 390 400
VP2
Bastianni SPQASTYVPITVTVAPMCAEYNGLRLAGHQGLPTMNTPGSTQFLTSDDFQSPSAMPQFDVTPEIQIPGQVRNLMEIAEVDSVVPVNNTEEHVNSIEAYRI
13311 .....V.....GN...M.....
13759 .....
14397 .....V.....GN...M.....
410 420 430 440 450 460 470 480 490 500
Bastianni PVRPQTNSGEQVFGFQLRPGYDSVLKHTLLGEILNYYANWSGSMKLTFMYCGAAMATGKFLIAYSPPGAGVPGSRKDAMLGTHVIWDVGLQSSCVLCVPW
13311 .....S.....Q..H.....T.....
13759 .....S.....Q.....R.....M.....
14397 .....S.....Q..H.....
510 520 530 540 550 560 570 580 590 600
VP3
Bastianni ISQTNYRYVTSDAYTDAGYITCWYQTSIVTPPDIPTTSTILCFVSACNDFSVRLLRDTPFITQQALYQNDPEGALNKAVGRVADTIASGPVNTEQIPALT
13311 .....S.I.R.....V.....
13759 .....S.I.R.....V.....
14397 .....V.....S.I.RT.....V.....
610 620 630 640 650 660 670 680 690 700
Bastianni AVETGHTSQVVPSDTMQTRHVVNFHTRSESSLENFMGRAACVYIAHYATEKANDDLDRYTNWEITTRQVAQLRRKLEMFTYMRFDLEITFVITSSQRTSN
13311 .....I.Y.....I.....Q.....V..E.....L.....T
13759 .....Y.....I.....Q.....V..E.....T
14397 .....I.Y.....I.....Q.....V..E.....L.....T
710 720 730 740 750 760 770 780 790 800
Bastianni RYASDSPPLTHQIMYVPPGGPIPTGYEDFAWQTSTNPSVFWTEGNAPPRMSIPFMSVGNAYCNFYDGWSHFSQSGVYGYTTLNNMGHLYFRHVNKSTGYP
13311 T.....V.....KS.....A..
13759 T.....V.....RS.....A..
14397 T.....V.....KS.....A..
810 820 830 840 850 860
VP1+
Bastianni VNSVARVYFKPKHVKAWVPRAPRLCPYLYAKNVNFDVQGVTESRGKITLDRSTHNPVLTT
13311 .....R.....D.....LTN.
13759 .....L.N.
14397 .....Q....R.....D.....LTN.

B

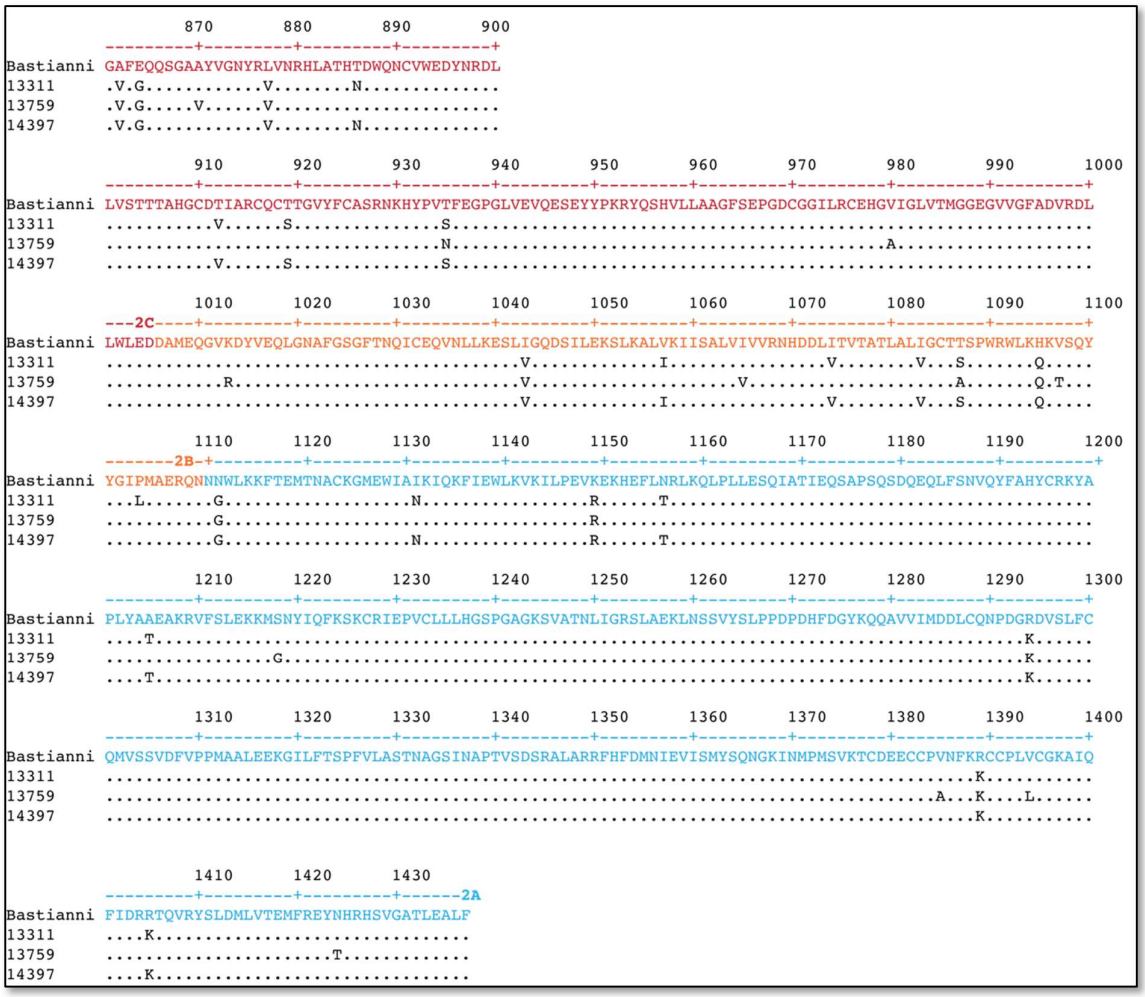
870 880 890 900
Bastianni GAFEQQSGAAYVGNYRLVNRHLATHTDWQNCVWEDYNRDL
13311 .V.G.....V.....N.....
13759 .V.G.....V.....V.....
14397 .V.G.....V.....N.....
910 920 930 940 950 960 970 980 990 1000
Bastianni LVSTTTAHGCDTIARCQCTTGVYFCASRNKHYPVTFEGPGLVEVQESEYYPKRYQSHVLLAAGFSEPGDCGGILRCEHGVIGLVTMGGEGVVGFADVRDL
13311 .....V.....S.....S.....
13759 .....N.....A.....
14397 .....V.....S.....S.....
1010 1020 1030 1040 1050 1060 1070 1080 1090 1100
---2C----
Bastianni LWLEDDAMEQGVKDYVEQLGNAFGSGFTNQICEQVNLLKESLIGQDSILEKSLKALVKIISALVIVVRNHDDLITVTATLALIGCTTSPWRWLKHKVSQY
13311 .....V.....I.....V.....V...S.....Q.....
13759 .....R.....V.....V.....A.....Q.T...
14397 .....V.....I.....V.....V...S.....Q.....
1110 1120 1130 1140 1150 1160 1170 1180 1190 1200
-------2B-+
Bastianni YGIPMAERQNNNWLKKFTEMTNACKGMEWIAIKIQKFIEWLKVKILPEVKEKHEFLNRLKQLPLLESQIATIEQSAPSQSDQEQLFSNVQYFAHYCRKYA
13311 ...L.....G.....N.....R.....T.....
13759 .....G.....R.....
14397 .....G.....N.....R.....T.....
1210 1220 1230 1240 1250 1260 1270 1280 1290 1300
Bastianni PLYAAEAKRVFSLEKKMSNYIQFKSKCRIEPVCLLLHGSPGAGKSVATNLIGRSLAEKLNSSVYSLPPDPDHFDGYKQQAVVIMDDLCQNPDGRDVSLFC
13311 ....T.....K.....
13759 .....G.....K.....
14397 ....T.....K.....
1310 1320 1330 1340 1350 1360 1370 1380 1390 1400
Bastianni QMVSSVDFVPPMAALEEKGILFTSPFVLASTNAGSINAPTVSDSRALARRFHFDMNIEVISMYSQNGKINMPMSVKTCDEECCPVNFKRCCPLVCGKAIQ
13311 .....K.....
13759 .....A...K....L.....
14397 .....K.....
1410 1420 1430
---------+---------+---------+------2A
Bastianni FIDRRTQVRYSLDMLVTEMFREYNHRHSVGATLEALF
13311 ....K.....
13759 .....T.....
14397 ....K.....

C

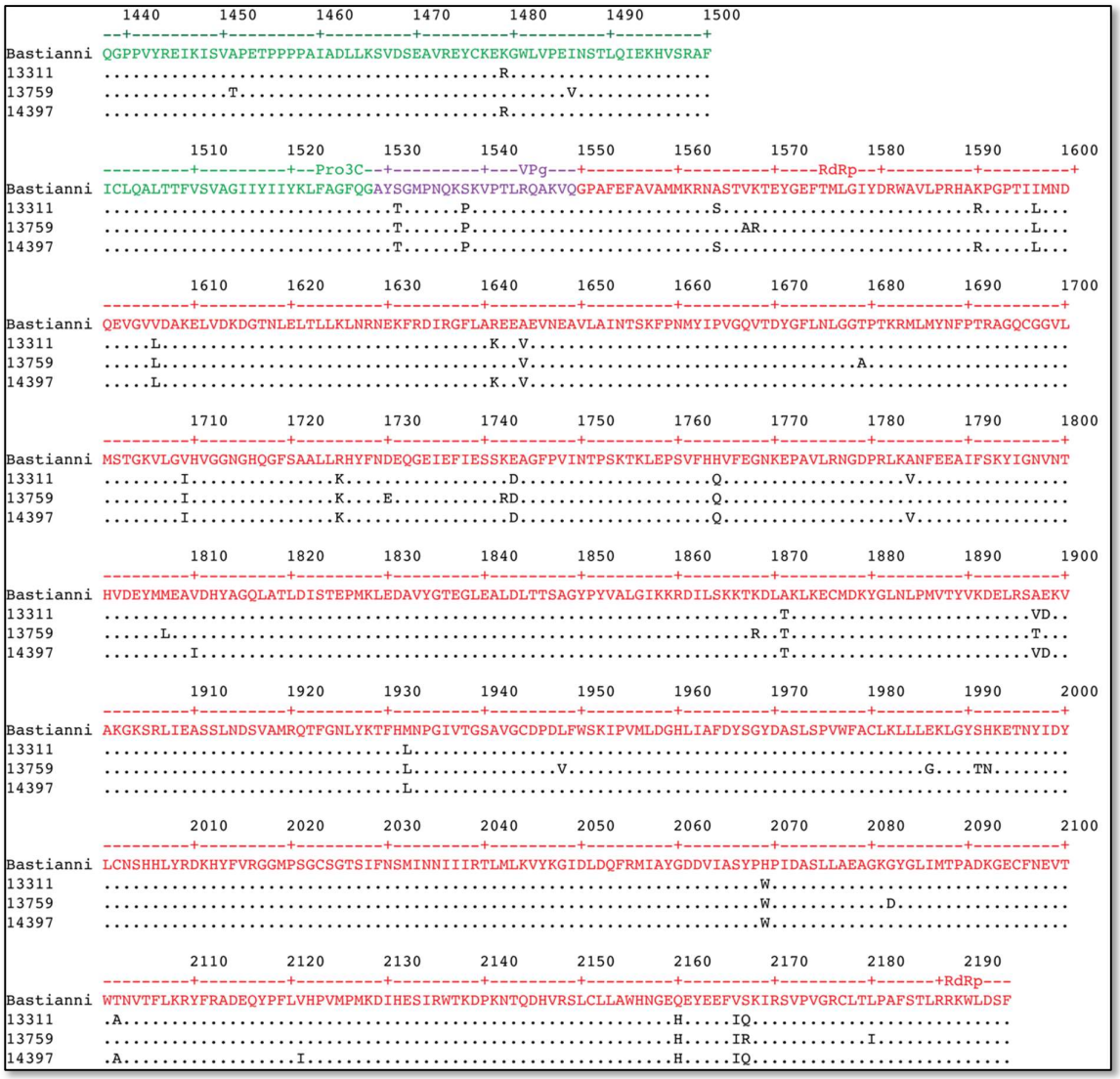
1440 1450 1460 1470 1480 1490 1500
Bastianni QGPPVYREIKISVAPETPPPPAIADLLKSVDSEAVREYCKEKGWLVPEINSTLQIEKHVSRAF
13311 .....R.....
13759 .....T.....V.....
14397 .....R.....
1510 1520 1530 1540 1550 1560 1570 1580 1590 1600
--Pro3C-- --VPg--- ----RdRp--
Bastianni ICLQALTTFVSVAGIIYIIYKLFAGFQGAYSGMPNQKSKVPTLRQAKVQGPAFEFAVAMMKRNASTVKTEYGEFTMLGIYDRWAVLPRHAKPGPTIIMND
13311 .....T.....P.....S.....R.....L...
13759 .....T.....P.....AR.....L...
14397 .....T.....P.....S.....R.....L...
1610 1620 1630 1640 1650 1660 1670 1680 1690 1700
Bastianni QEVGVVDAKELVDKDGTNLELTLLKLNRNEKFRDIRGFLAREEAEVNEAVLAINTSKFPNMYIPVGQVTDYGFLNLGGTPTKRMLMYNFPTRAGQCGGVL
13311 .....L.....K..V.....
13759 .....L.....V.....A.....
14397 .....L.....K..V.....
1710 1720 1730 1740 1750 1760 1770 1780 1790 1800
Bastianni MSTGKVLGVHVGGNGHQGFSAALLRHYFNDEQGEIEFIESSKEAGFPVINTPSKTKLEPSVFHHVFEGNKEPAVLRNGDPRLKANFEEAIFSKYIGNVNT
13311 .....I.....K.....D.....Q.....V.....
13759 .....I.....K....E.....RD.....Q.....
14397 .....I.....K.....D.....Q.....V.....
1810 1820 1830 1840 1850 1860 1870 1880 1890 1900
Bastianni HVDEYMMEAVDHYAGQLATLDISTEPMKLEDAVYGTEGLEALDLTTSAGYPYVALGIKKRDILSKKTKDLAKLKECMDKYGLNLPMVTYVKDELRSAEKV
13311 .....T.....VD..
13759 .....L.....R..T.....T...
14397 .....I.....T.....VD..
1910 1920 1930 1940 1950 1960 1970 1980 1990 2000
Bastianni AKGKSRLIEASSLNDSVAMRQTFGNLYKTFHMNPGIVTGSAVGCDPDLFWSKIPVMLDGHLIAFDYSGYDASLSPVWFACLKLLLEKLGYSHKETNYIDY
13311 .....L.....
13759 .....L.....V.....G....TN.....
14397 .....L.....
2010 2020 2030 2040 2050 2060 2070 2080 2090 2100
Bastianni LCNSHHLYRDKHYFVRGGMPSGCSGTSIFNSMINNIIIRTLMLKVYKGIDLDQFRMIAYGDDVIASYPHPIDASLLAEAGKGYGLIMTPADKGECFNEVT
13311 .....W.....
13759 .....W.....D.....
14397 .....W.....
2110 2120 2130 2140 2150 2160 2170 2180 2190
--RdRp---
Bastianni WTNVTFLKRYFRADEQYPFLVHPVMPMKDIHESIRWTKDPKNTQDHVRSLCLLAWHNGEQEYEEFVSKIRSVPVGRCLTLPAFSTLRRKWLDSF
13311 .A.....H.....IQ.....
13759 .....H.....IR.....I.....
14397 .A.....I.....H.....IQ.....

D

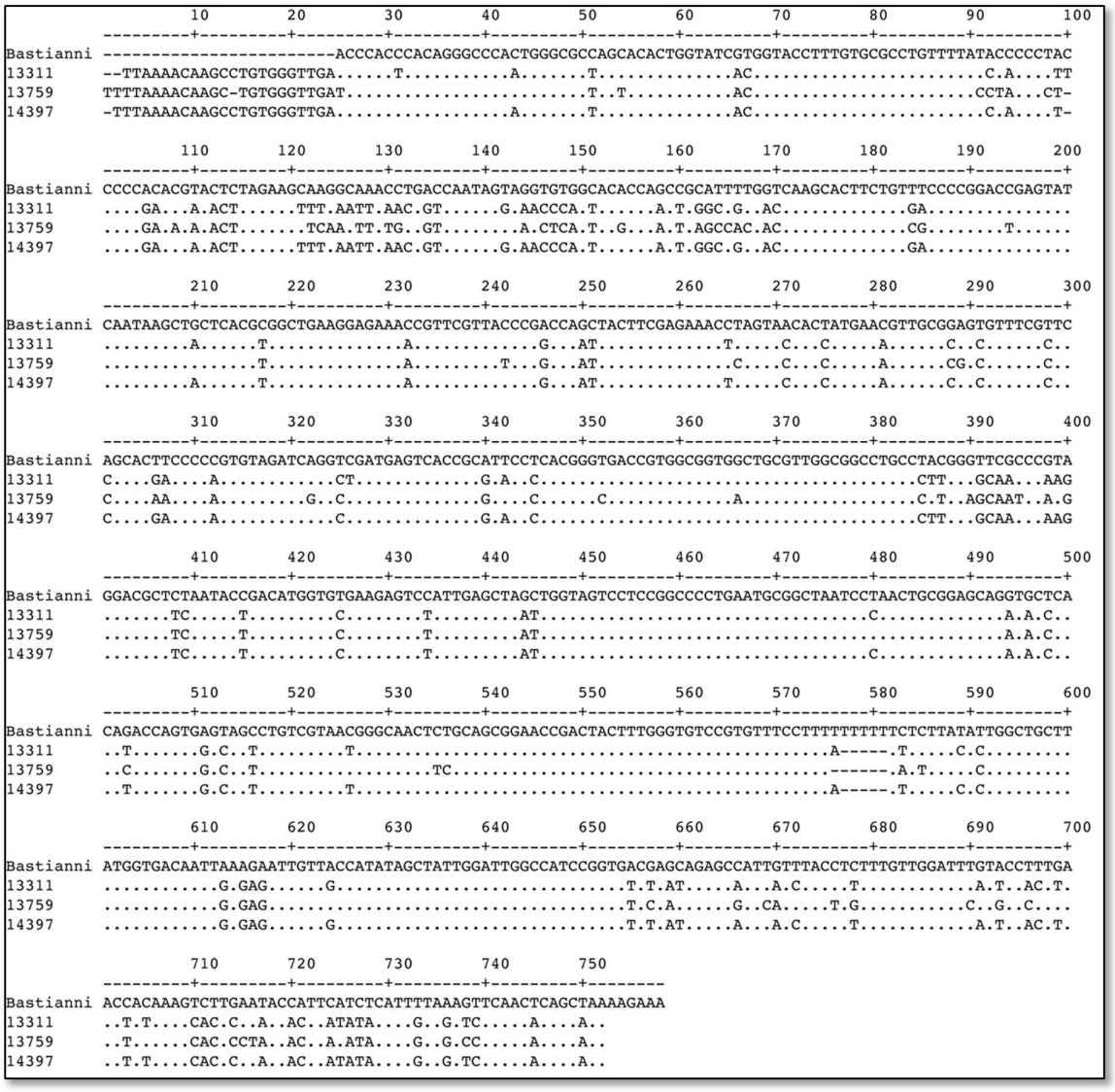

Figure 32. Sequence alignment of E-30 strains. Sequences of E-30 Bastianni, 13-311, 13-759 and 14-397 were aligned and compared. On the P1 region, amino acids, from the outbreak strains, which are found on the same position in the sequence of E-30 Bastianni are marked with dots. The protein sequences of the structural proteins VP1 (purple), VP2 (blue), VP3 (blue) and VP4 (red) are illustrated.

5.5.2. E-30 homology analysis

The information obtained from the sequence alignment of E-30 strains showed some interesting differences and similarities between them. To further enhance the characterisation of the viral strains we focused on the genetic evolution of the E-30 strains, in particular of the clinical isolates. With the application of GenBank we built neighbour-

joining nucleotide phylogenies for the full P1 nucleotide regions (Fig. 33). E-30 13-311 and 14-397 are closely related and are part of a cluster of E-30 strains, which have been discovered mainly in China and Ukraine. Strain E-30 13-759 was calculated to not be closely related in terms of phylogenetic relationship. But it showed great similarities with strains isolated in France, such as KF920598.1/FRA/2013 (96.9 – 97.2 % nucleotide similarity) (Fig. 33). Moreover, numerous E-30 strains from around the world show high phylogenetic similarities to E-30 Bastianni and the outbreak strains used in this work.

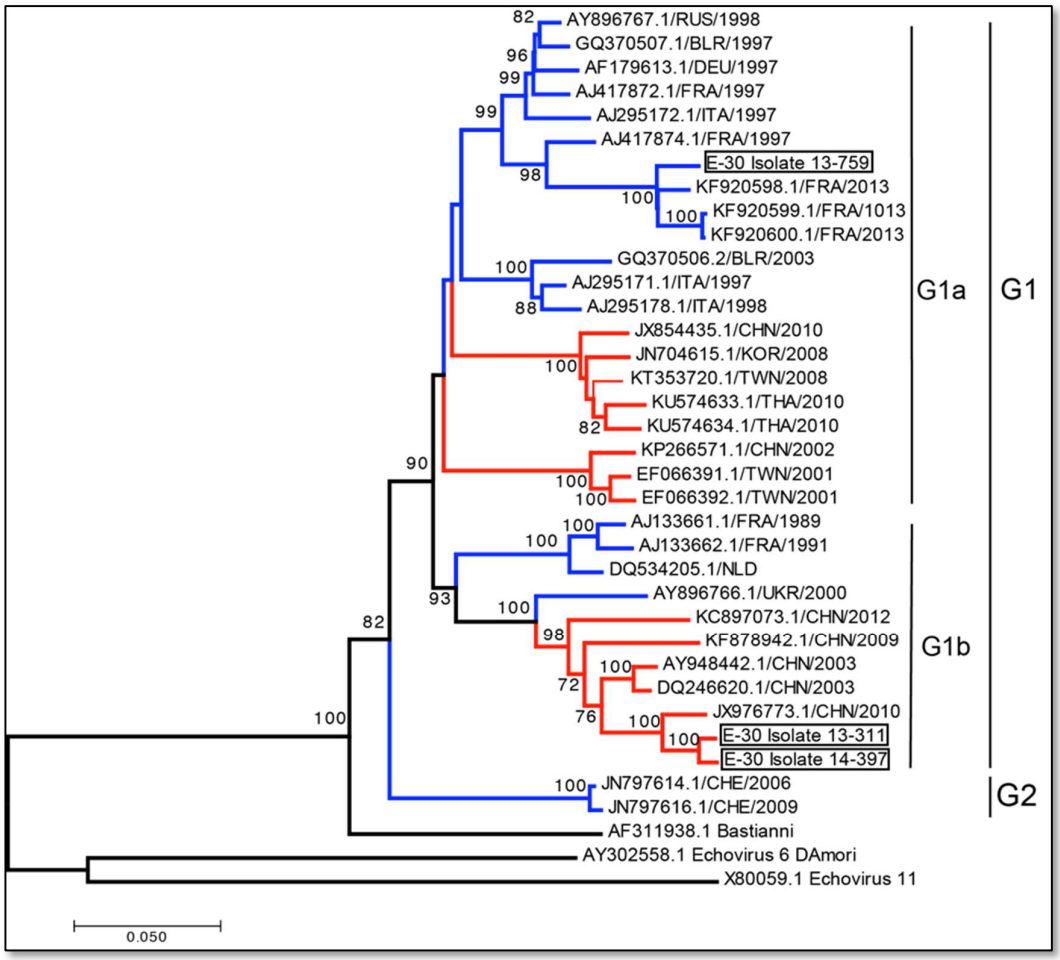

Figure 33. Phylogenetic analysis of E-30 strains. The structural proteins VP1-4 were aligned. Similar strains were identified on GenBank and used to compare, based on nucleotide regions encoding the complete capsid proteins (VP1-4) to the E-30 Bastianni, 13-311, 13-759 and 14-397. Colorimetric differences indicate the location of their isolation: Blue for Europe and Red for Asia. Only bootstrap values >70% are shown at relevant nodes. As outgroup, we applied the prototype strains Echovirus 11 (X80059.1) and Echovirus 6 (AY3025588.1). The branch length is directly proportional to the marked scale (Bottom left) and indicates the amount of nucleotide substitutions per site.

6. Discussion

6.1. Specific role of enteroviral strains on barrier function and morphology of the BCSFB

The BCSFB has been identified as a possible entry site for viral pathogens and leukocytes into the CNS. Enteroviral strains, particularly Echovirus 30, may use this route of entry to penetrate the protective barrier and infect the CNS. The components of the BCSFB, which are mainly involved in creating and maintaining the integrity of the barrier, are TJs such as ZO1 and Occludin and AJ proteins such as E-cadherin. This complex network is able to reduce and restrain the movement of pathogens and leukocytes between the blood stream and the CNS. An important focus of this work laid in confirming the involvement of these TJ and AJ proteins and their effect on the integrity of the barrier during infection of various EV 30 strains. The *in vitro* BSCFB model consisting of HIBCPP cells represents the barrier found *in vivo* and therefore allows examination of the effects of viral infection. The response of the HIBCPP cells to infection with the strain E-30 Bastianni, used as a prototype, was compared to E-30 strains which were identified during the German outbreak of viral meningitis 2013/2014. Especially the morphological changes which follow a viral infection and the subsequent leukocyte migration can be visualised and studied in this model of the human choroid plexus.

We noticed that viral infection, especially for E-30 but also the outbreak strain 13-311, led to a decrease in TEER. Focus was turned to the effects of viral infection from the basolateral side to identify and specify variations between the genotypes. We discovered that infection of the HIBCPP cells with the three E-30 outbreak strains and Bastianni led to distinct differences in permeability. The infection with 13-759 and 14-397 had little to no effect on the integrity of the barrier, however, when infected with E-30 Bastianni or 13-311 the permeability of the barrier was increased significantly.

Studies carried out in *in vitro* models of the BBB of mice has shown strain-specific alterations to the BBB permeability. Immortalized mouse endothelial cells (bEnd.3) were infected with three genotypes of the mouse hepatitis virus (MHV) and modifications to the TJ and AJ proteins were noted. Interestingly these variations were shown both on RNA and protein level for E-cadherin, Occludin and ZO1. Although these alterations were noted with all three variants used, only the MHV3 strain was detected on the apical endothelial cell side, thus

having crossed into the CNS [85]. During another study at the level of the BBB it was shown that NPEV variants may affect the integrity of the endothelial cell layer in a strain-specific manner. Upon infection of the *in vitro* brain endothelial cell (hCMEC/D3) layer with either coxsackievirus group B (CV-B) or EV-A71, the paracellular permeability and the actin staining remained comparable to the control. However, when the brain endothelial cells were infected with the cytolytic E-6, E-11, E-12 or E-30 serotype, a decrease in TEER, augmented paracellular permeability and reduced actin staining indicated an important impairment of the barrier function [86]. This contrasts with our observation of an intact actin staining in all experimental conditions. This points towards the fact that the effect of viral infection is specific to certain cellular structures and in this case does not alter the actin cytoskeleton. The remarkable strain-specific effects on barrier integrity have also been observed when CaCo-2 cells were infected with variants of CVB. Notably the affinity for the receptors Coxsackievirus and adenovirus receptor (CAR) or decay-accelerating factor (DAF) was the decisive step which controlled the stability of the TEER [87]. These TJ-localized integral membrane proteins are also used by several viruses as receptors during infection [88-90]. Due to the lack of relevant data on echovirus receptor affinity on human choroid plexus epithelial cells, we so far were not able to correlate the strain specific effects with possible receptor interactions. Using polarized epithelial cells (Caco-2 cells) a decrease in TEER in correlation with an augmentation of the paracellular flux of the fluorescent sugar markers dextran and mannitol was shown following infection with CV-B3 strain [91]

Focusing on the complex cell-to-cell connection proteins of the tight and adherens junction, disruptions to the normally very regular “honeycomb-like” pattern was observed for HIBCPP cell layers infected with E-30 Bastianni and 13-311. These findings underline that the increase in permeability of the HIBCPP cell layer may likely be caused by morphological changes of the epithelial cells triggered by the infection of specific E-30 genotypes. Infection with E-30 Bastianni and 13-311 caused similar effects on the morphology of ZO1 and Occludin and to a lesser extend to that of E-cadherin. The alterations in permeability discussed above and taken together with the visual changes at the level of TJ and AJ connections between the cells are an indication for important impacts on the barrier integrity. These were visualized through immunofluorescent analysis and could be, especially for E-30 Bastianni, correlated to a decrease in TEER and increase in paracellular permeability.

Downregulation of ZO1 and Occludin, but also further junctional proteins, has shown to have a direct effect on the decrease in barrier integrity [92, 93].

The correlation between infection with a viral pathogen causing changes in morphology of the cells and a decrease in barrier integrity was shown *in vitro* following infection with HIV-1. The infection of human retinal pigment epithelial (HRPE) cells with HIV-1 led to an increased paracellular movement of sodium fluorescein caused and reflected in the decreased TEER [94]. This has also been looked at with the focus on the AJ proteins. The correct functionality of E-cadherin was linked to barrier permeability. A decreased TEER causing an increase in permeability of dextran, inulin and mannitol was observed following the infection of airway epithelial cells with the adenovirus. The viral infection led to dysfunction of E-cadherin and this was identified as the cause for barrier impairment [95].

For further confirmation we looked at the TJ and AJ protein expression. The similarity between E-30 Bastianni and 13-311 compared to 13-759 and 14-397 was not reflected in analysis of protein content. However, we believe that the proteins were not denatured but rather changed and underwent morphological changes. This was based on previous findings from bacterial infection of porcine choroid plexus epithelial cells. The infection led to morphological changes of the cells in parallel with TJ proteins from membrane fraction (Triton X insoluble) relocating to the soluble fraction (Triton X soluble) [96]. The approach to separate the membrane into two fractions was investigated. However, this method did not lead to any conclusive results. For clarification of the infection mechanism which affects the protein expression in HIBCPP, cells would be needed. Most likely, the reason for the lack of correlation may be the overall low number of infected cells. As the complete HIBCPP cell layer was used for protein analysis, the much higher percentage of healthy and uninfected cells may have masked the changes in the infected cells. Follow-up experiments with higher percentage of infected cells need to be carried out, as strong indication exists that enteroviruses utilise cell-to-cell junctions as a mean to infect the protective barriers of the CNS and that these infections lead to modifications in protein expression [72, 97].

As the involvement of junctional proteins during viral infection is well understood, it would be of great interest to investigate the cause of these disruptions and put these findings in relation to previously discovered modes of action [86, 94, 98, 99]. In literature many observations similar to our results in relation to the infection leading to increased

paracellular permeability and loss of junctional integrity have been made [99, 100]. It is known for a range of viruses to manipulate the actin network of polarized epithelial cells to facilitate host invasion [101-104]. Therefore, we expected to see a virus-induced impact on the cytoskeleton and an influence on the migration pathways of immune cells, which was not visible during the immunofluorescence analysis.

6.2. Distinct migration pattern of leucocytes across the BCSFB after enteroviral infection

When measuring the composition of the CSF during different stages of NPEV meningitis, a shift in leukocyte population can be observed. The cell population consists mainly of PMN during the early stages of the infection and shifts to a $CD4^+$ T-lymphocytes and other mononuclear cell population. Investigations into the relation between and possible interactions of different cell types during enteroviral meningitis have not yet been performed.

During bacterial infection with *Neisseria meningitidis* the importance of sequential migration of different immune cell populations into the CNS across the BCSFB has been highlighted [33]. To obtain a more complete understanding of the synergism during immune cell transmigration at the occasion of viral meningitis, we investigated sequential transmigration of PMN and T cells in the presence of specific chemokine profiles. In our model, PMNs showed a significant increase in transmigration rates across the epithelial cell layer in the presence of T cells. This enhanced migration due to the presence of another cell type was not measured vice versa. In murine *in vivo* studies in the context of acute viral encephalitis it was shown that monocytes promote the transmigration of T lymphocytes only across the glia limitans, whereas T-lymphocyte migration across the BBB was independent of monocytes [105]. Both PMN and naïve T-lymphocyte migration from the basolateral to the apical HIBCPP cell side was increased following E-30 Bastianni infection. This increase was only achieved in the presence of IL-8 for PMN and CXCL 12 for T cells. Here we can already see the importance of chemical stimulus for the immune cell response during viral meningitis.

We have further investigated this interesting fact during the cytokine and chemokine secretion studies. Residual CNS cells maintain high levels of CXCL 12 concentration in the CSF

and create a further increase during inflammation [106, 107]. The high levels of CXCL 12 can result in T-lymphocyte migration. We also observed this in our system, where interestingly we could measure an increase in PMN migration in the presence of naïve CD3+ lymphocytes. Thus CXCL 12 does not have a direct effect on PMN migration, however we were able to identify a secondary effect through the enhanced T-lymphocyte presence. Also, at the BBB, *in vitro* studies observed lower lymphocyte migration after the removal of monocytes from the system [108]. The link between presence and interaction of different cell types and alterations to the migration pattern was also seen *in vivo* in mice. Interestingly, it was shown that the presence of monocytes can have opposite effects on the transmigration of T lymphocyte transmigration depending on their localization [105]. The presence of monocytes was shown to be of no importance during the recruitment of T cells towards the infected CNS, however, for movement of T-lymphocytes through the glia limitans the presence of monocytes had a positive effect [105].

6.3. PMN and T lymphocytes migrate both para-and transcellularly across the infected BCSFB

Once a pathogen enters the CNS and causes infection, the immune system responds by directing leukocytes to the site of the infection. The response is dependent on the type of the pathogen and precisely controlled through the releases of specific cytokines. To reach the site of infection, leukocytes cross the protective barrier by one of two, or both known routes. In this study we concentrated our effort on determining the chosen pathways of both PMN and T-lymphocytes. We focused on the extent of barrier impairment caused by E-30 Bastianni or the three outbreak strains and how it may correlate with an increase in paracellular migration of the leukocytes. Despite extensive immunofluorescence analysis and further TEM and FIB/SEM studies, we were not able to identify a preferred pathway. In all approaches we observed PMN and T-lymphocytes at different stages of both para- and transcellular migration. Quantification of cells choosing either trans- or paracellular migration was not possible. This was due to the low number of migrating cells visualized. However, the majority of investigations identified the paracellular route as the preferred mode of diapedesis [115, 116]. Further observations were made at the level of the BCSFB and BBB following bacterial infection. Infection of HIBCPP cells with *Neisseria menigitidis* led

to both para-and transcellular migration of PMN [33]. Infection of PCPEC with *Streptococcus suis* showed PMN using both pathways, yet the transcellular route was preferred over the paracellular [117].

Interestingly, until these recent publications, it was a frequent assumption that cells undergoing diapedesis would choose the path of least resistance. This theory correlates a decrease in TEER with an increase in paracellular migration [113]. In an *in vitro* study carried out with human lung and human microvascular cells and primary rat heart and brain endothelial cells, it was shown that the path of least resistance is chosen by migrating leukocytes [113]. However, rapid repair and reconstruction of TJ connections was observed after paracellular movement of leukocytes across the endothelium [109, 110]. Further support for migration being independent of possible barrier impairment comes from the observation that cell surface proteins may play a decisive role in the choice of pathway. The migrating cells do not choose their pathway according to possible impairment of the barrier but rather due to receptor interactions. The decisive factors for the choice between para- and transcellular migration of leukocytes are not yet fully understood; however, the importance of chemical stimulus and integrin activation is evident.

In another study the hypothesis of PMN transmigration being dependent on the expression levels of ICAM-1 was tested and they came to the conclusion that decreased levels of functional ICAM-1 led to a decrease in transcellular transmigration across human umbilical vein endothelium cells (HUVECs) [112]. This is supported as the importance of expression levels of chemokines and integrins has been identified as a key factor for leukocyte diapedesis into the infected CNS [113, 114]. At the level of the BBB it was possible to identify protein interactions which played a decisive role in deciding the migration pathway. Here, endothelial ICAM has been described to play a decisive role in choosing the pathway. Furthermore, both *in vitro* and *in vivo* T-lymphocytes and neutrophils predominantly used the transcellular migration pathway across the endothelial cells [111]. The human epithelial cells applied to the transwell system used during this work express ICAM only on the apical side. Therefore, the leukocytes, migrating from the basolateral towards the apical cell side, do not establish early contact with ICAM upon reaching the barrier cells. Thus the question, whether or to which extent ICAM is involved, has not been investigated; in consequence also the potential effect of ICAM expression and interaction with the leukocytes on the migration has not been studied in the course of this work.

6.4. Polar secretion patterns for cytokines and chemokines from HIBCPP cells after enteroviral infection

Cytokines, chemokines and chemokine receptors play an important role in the control of activation and movement of leukocytes towards the infected CNS. Further the balance between pro- and anti-inflammatory cytokines also affects the migration of leukocytes. Particularly IL-8 and CXCL12 for PMN and T-lymphocytes have been shown to influence migration. Furthermore, the cytokine and chemokine profile of the CSF show distinct variations between healthy and infected patients. We observed low levels of IL-6, IL-10, IL-13, IL-1β IFN-γ and TNF-α in our system. Whereas patients infected with EV-71 show high levels of the named chemokines in the CSF and serum [118-121]. In our model we used naïve $CD3^+$ T cells and did not include other cells of the CNS such as glial cells or neurons, which might be a possible explanation for the low levels of detected chemokines named [59]. On the other hand, we observed high levels of IL-8, CXCL 3, CCL 20 and CXCL10 independent of enteroviral infection. The importance of these chemokines during viral meningitis has been shown [36, 58].

As Reboldi also showed high levels of CCL 20 in the CSF of healthy human and mice *in vivo,* this particular chemokine might be an interesting target for further studies [122]. Combination of the observations made on the high levels of CXCL 3, CXCL 10, IL-8 and CCL20 found in the CNS led to the assumption that the epithelial cells of the choroid plexus are implicated in the control of movement of T lymphocytes and PMN from the blood into the CNS. In the CSF of patients suffering from aseptic meningitis, sharp rise in infiltrating PMNs was accompanied by raised concentration of G-CSF [69]. Production of chemokines by epithelial cells plays an important role in the highly regulated cascade of events leading to immune cell movement from the stroma of the choroid plexus to the CNS.

The relationship between specific chemokine profiles and according leukocyte populations has also been shown during E-30 infections. Leukocytes usually move from an area of low chemokine concentration to an area of high chemokine concentration. This chemical gradient was observed for both CXCL 10 and CXCL 11. Following infection, higher concentrations were detected in the CSF compared to the plasma [123]. A dominant PMN and T-lymphocyte population in the CSF was in accordance with a shift from pro-inflammatory cytokines such as IFN-γ, IL-6 and IL-8 to the anti-inflammatory cytokines TGF-

ß1 and IL-10 [67]. Monocyte recruitment is known to be triggered by the release of CCL 12 in mice. At the BCSFB of mice the strong involvement of CCL 12 (which corresponds to CCL 2 in human) has been detected during the migration of Coxackievirus B3 (CVB3)-infected nestin^{+} myeloid cells [71]. Interestingly, after infection with the lymphocytic choromeningitis virus (LCMV) the chemoattractant profile was different to that seen after CVB3 infection. Most importantly CCL 12, known to cause monocyte recruitment was not detected after LCMV infection. Due to the lack of chemical stimulus, recruitment of myeloid cells was observed. The importance of specific chemokines, their location and concentration but also the interplay between various cytokines and chemokines is evident. Therefore, we focused on quantifying various cytokines and chemokines and analysing their direction of secretion after E-30 infection

Furthermore, we focused on the direction of chemokine secretion. We found it interesting that in our system only IL-7 was secreted to the apical cell side. Even though IL-7 is involved in the regulation of T-lymphocyte homeostasis, we do not believe that it is the sole regulator for increased leukocyte transmigration, because the levels of IL-7 measured on the apical side did not vary depending on the experimental conditions and cells present. The role of IL-7 in the CNS has been studied both *in vivo* and *in vitro*, however further studies are needed to fully understand its role and possible interactions with other chemokines and cell movement [124]. Another possible explanation for the role of IL-7 is in regards to its involvement in advancing leucocyte phenotype, which aids in inflammation reduction and resolution. The resulting phenotype has been identified to have properties supporting the resolution of an inflammation [125]. We were able to identify specific chemokine profiles following E-30 Bastianni infection, however due to the limitation within the *in vitro* system and very low overall levels of many chemokines measured, we believe that further *in vivo* studies would be needed for clarification.

6.5. Enteroviral strain specific replication patterns in HIBCPP cells

As many pathogens such as viruses penetrate the host cells and use the cellular structures for their own replication, we were curious to know whether possible difference in the speed of viral infection, absolute viral replication or viral dissemination would help understanding the observed differences. Virus replications, or other secondary effects, have shown to be

able to disrupt the protective barriers of the brain [126]. Viral RNA of the prototypic E-30 Bastianni was detected in much higher quantities within the HIBCPP cells compared to when infected with the outbreak strains. Also, the replication rates were many-fold higher than the other strains. No differences were observed between the outbreak strains in terms of viral replication and percentage of infected cells. The higher concentration of E-30 Bastianni RNA and overall faster infection and growth rates are also reflected in the higher percentage of infected HIBCPP cells.

We had observed a pattern in which the E-30 Bastianni and the 13-311 had similar effects on the barrier integrity in terms of paracellular permeability and effect on TEER, whereas the outbreak strains 13-759 and 14-397 had comparable low or no effect. Considering the replication and infection rates of all four strains we cannot explain the observed differences at the level of the barrier with the viral dissemination and growth rates. For strain 14-397 very low number of viral copies were detected, which might be caused by the low infection efficacy and thereby caused slower replication within the HIBCPP cells. E-30 Bastianni is already found in high numbers within the HIBCPP cells after only 5 hours of infection which also could explain the many-fold higher viral copies detected at the end of the experiment. Interestingly, all four viral strains have a similar percentage of viral copies already in the apical compartment.

When the HIBCPP cells were infected from the basolateral side, we observed replication of the virus in the cells. The viral copies were then released towards the apical side (representing the CNS *in vivo*) of the epithelial cells. Taking into consideration the findings on viral replication, infection frequency and distribution of viral copies around the BCSFB system, we could conclude that the morphological changes to the barrier were not solely dependent on these parameters. A replication independent effect on epithelial cell barrier function and morphology has been observed also during host infection with other viruses. Following apical infection of CaCo-2 cells with Astrovirus, the paracellular permeability increased and, as seen during our study, was accompanied by a disruption of Occludin. However, the impairment was rather due to a capsid protein than to the replication of the virus [127]. Similar findings were made during HIV infection of primary epithelial cells from the female genital tract. A significant impairment of the tight junction proteins in parallel to an increased paracellular permeability was deemed to be independent of viral replication but rather due to the presence of viral envelope glycoprotein [128]. The fact that the viral

life cycle or other secondary effects on the host and differences in these processes between the strains may have a role in the process of barrier disruption, needs to be looked at in more detail.

6.6. Genetic analysis of E-30 strains (Homology modelling)

As we wanted to determine whether the observed differences between the E-30 variants used in this study could be in relation to their genetic similarities and differences, we carried out sequence analysis of all strains. Epidemics worldwide and seasonal outbreaks have been led back to genetic recombination [46, 47, 129, 130]. For the strains used in our study we were able to show some variation in the areas of non-structural and structural proteins. With the information acquired we were not able to link the detected differences with the observations made during the infection experiments with HIBCPP cells and RD cells. However, some interesting information arose from the genetic analysis. The strain with the least effect on the epithelial cells and barrier integrity, 14-397, and the outbreak strain with the most obvious effect, 13-311, only show variation in 10 amino acids of the polyproteins. During the phylogenetic analysis we were able to confirm that the two strains were closely related. The observation made during the genetic analysis, that both were closely related was also confirmed through phylogenetic analysis.

In literature mutation in the VP1 region of E-30 are described as having the most striking effect on the resulting serotype. Serotypes showing mutations in this region have been linked to outbreaks causing severe meningitis [48, 73, 131, 132]. The VP1 region is one of the four structural proteins (VP1-4) of the E-30 capsid. VP4 is the only one which is not presented on the capsid surface of the virus [133]. The fact that most seasonal outbreaks can be led back to mutations in the VP1 region is reasonable as this region determines the antigenic characteristics of the serotype [48]. Genetic variations as small as some differences in a couple of amino acids can already alternate the ability of a virus to recognise and bind to cellular receptors [134]. Even a substitution of just one amino acid in the genome of CV-B variant enables binding to and infection of RD-cells [135, 136]. Not only the infection ability of the strains is altered but also other factors such as replication may be affected. A phenotype switch and increase in replication frequency was observed when one amino acid of the VP1 protein of CV-B6-Schmitt was exchanged [137]. Strain dependent effects on

epithelial cells were observed for CV-B *in vitro*. Slight changes to the genetic code of the VP1 region led to different effects of the variants during epithelial cell infection. Particularly the interaction with DAF and CAR varied between the different isolates. The genetic variation was led back to influencing the affinity for receptors and changing the infection pattern of the virus [87].

7. Conclusion

This work contributes to the understanding of immune cell migration in relation to chemical stimulus and alterations to the BCSFB in humans following viral infection with E-30. It was shown that the presence of chemokines in an *in vitro* model of the BCSFB increases the migration rate of both $CD3^+$ T lymphocytes and PMN. Also, PMN transmigration across the HIPCPP cells was enhanced in the presence of $CD3^+$ T lymphocytes. When analysing the effect on barrier integrity of different E-30 strains we observed strain dependent results. One of the three outbreak strains investigated, namely 13-311, had similar effects on the TJ proteins ZO1 and Occludin and AJ protein E-cadherin of HIBCPP cells as the prototypic strain E-30 Bastianni, which was also used during the previous studies. The other strains, 13-759 and 14-397, were comparable to 13-311 in terms of replication, effects on paracellular permeability and viral dissemination. However, they influenced the integrity of the junctional proteins to a much lesser extent. We were able to detect both para- and transcellular migration of immune cells across healthy and infected HIBCPP cell barriers. Furthermore, genome sequencing of the structural proteins VP1, VP2, VP3 and VP4 of the strains used showed areas of noticeable similarities and differences. It was not possible to link the pattern observed on a genome level to the variation in effect during the infection of the HIBCPP cells.

Overall, we gained insight into the effect of E-30 infection of the human CNS and could enhance the knowledge of viral meningitis and the importance of the BCSFB during immune cells migration.

8. Future outlook

Building on the observations made during this work, it could be very interesting to link clinical data from patients suffering from viral meningitis to experimental results using isolated strains. The step-by-step progression of the viral particles from the moment of infecting an human cell, their replication to the release into the CNS could add to the understanding of the pathogenesis.

Further experiments focusing on the chemokine profile and release pattern, particularly possible synergies between different chemokines, could help understand the migration of leukocytes and the epithelial cell response better. An investigation into a possible shift of the junctional proteins from the soluble to the insoluble membrane fraction would be very interesting. This would need to be carried out with a much higher percentage of infected cells and would give more insight into the effect of viral infection on the TJ and AJ proteins.

Extensive analysis into quantification of para- and transcellular migration of immune cells across an infected epithelial cell layer would give a better understanding of a possible link between migration pathway and paracellular permeability. The fact that the increased paracellular permeability did apparently not lead to a more dominant paracellular migration, may mean that the immune cells migrated independently of the state of the barrier and thus would raise the question which factors are involved. Here, maybe chemokine signalling or activation of the immune cells may play an important role. Also, visualization of the virus particles in and attached to the epithelial cells could clarify and visualize the infection and replication process.

Moreover, a deeper investigation into the genomic differences between outbreak strains could help to a better understanding of enteroviral pathogenesis. To evaluate the genomic differences better and link them to the infection abilities, it would be interesting to create clones with site-specific mutations and analyse these during infection experiments. This would allow identification of precise amino acids or specific clusters which are involved in detection, infection and replication. Finally, the *in vitro* experiments carried out in this work would be interesting to be combined with *in vivo* data and further linked with clinical observations.

9. Publication list and Conferences

Dahm T, Frank F, Adams O, Lindner HA, Ishikawa H, Weiss C, Schwerk C, Schroten H, Tenenbaum T, Rudolph H. 2017. Sequential transmigration of polymorphonuclear cells and naive CD3+ T lymphocytes across the blood-cerebrospinal fluid barrier *in vitro* following infection with Echovirus 30. *Virus Res*. 232: 54-62

Dahm T, Rudolph H, Schwerk C, Schroten H, Tenenbaum T. 2016. Neuroinvasion and Inflammation in Viral Central Nervous System Infections. *Mediators Inflamm*. Article ID 8562805, 16 pages doi:10.1155/2016/8562805

Dahm T, Adams O, Böttcher S, Diedrich S, Morozov V, Hansman G, Fallier-Becker P, Burkhardt C, Weiß C, Ishikawa H, Schwerk C, Schroten H, Tenenbaum T, Rudolph H. Strain dependent effects of clinical Echovirus 30 outbreak isolates at the blood-CSF barrier. *J.Neuroinflammation*. Under Review

Speaker at the “International Symposium on Signal Transduction at the Blood-Brain Barriers (IBBS)”, 2016 Copenhagen, Denmark.

Poster presentation at the Deutsche Gesellschaft für Pädiatrische Infektion, 2015 Freiburg, Germany

10. References

1. Abbott, N.J., et al., *Structure and function of the blood-brain barrier.* Neurobiol Dis, 2010. **37**(1): p. 13-25.
2. Saikat, R. *From outermost to innermost, what are the names and the correct order of the meninges around the brain?* 2016 25.03.2019]; Available from: https://socratic.org/questions/from-outermost-to-innermost-what-are-the-names-and-the-correct-order-of-the-meni.
3. Ehrlich, P., *Das Sauerstoff-Bedürfnis des Organismus. Eine farbe analytische Studie. Berlin Hirschwald.* Abh Preuss Wissensch. Phys-Math, 1885: p. 69-72.
4. Goldman, E.E., *Die äussere und innere Sekretion des gesunden und kranken Organismus im Lichte der "vitalen Färbung".* Beitr. Klin. Chirug, 1909. **64**: p. 192-265.
5. Crisan, E. and J. Chawala. *Ventricles of the Brain*. 2016 [cited 2019 24.09.2019]; Available from: https://emedicine.medscape.com/article/1923254-overview.
6. Brightman, M.W. and T.S. Reese, *Junctions between intimately apposed cell membranes in the vertebrate brain.* J Cell Biol, 1969. **40**(3): p. 648-77.
7. Redzic, Z.B. and M.B. Segal, *The structure of the choroid plexus and the physiology of the choroid plexus epithelium.* Adv Drug Deliv Rev, 2004. **56**(12): p. 1695-716.
8. Spector, R. and C.E. Johanson, *The mammalian choroid plexus.* Sci Am, 1989. **261**(5): p. 68-74.
9. Dahm, T., et al., *Neuroinvasion and Inflammation in Viral Central Nervous System Infections.* Mediators Inflamm, 2016. **2016**: p. 8562805.
10. Betz, L.A., G.W. Goldstein, and R. Katzman, *Blood-brain-cerebrospinal fluid barriers.* New York, Raven Press, 1989.
11. Strazielle, N. and J.F. Ghersi-Egea, *Choroid plexus in the central nervous system: biology and physiopathology.* J Neuropathol Exp Neurol, 2000. **59**(7): p. 561-74.
12. Wolburg, H. and W. Paulus, *Choroid plexus: biology and pathology.* Acta Neuropathol, 2010. **119**(1): p. 75-88.
13. Demeule, M., et al., *Drug transport to the brain: key roles for the efflux pump P-glycoprotein in the blood-brain barrier.* Vascul Pharmacol, 2002. **38**(6): p. 339-48.
14. Engelhardt, B. and L. Sorokin, *The blood-brain and the blood-cerebrospinal fluid barriers: function and dysfunction.* Semin Immunopathol, 2009. **31**(4): p. 497-511.
15. Vorbrodt, A.W. and D.H. Dobrogowska, *Molecular anatomy of intercellular junctions in brain endothelial and epithelial barriers: electron microscopist's view.* Brain Res Brain Res Rev, 2003. **42**(3): p. 221-42.
16. Hartsock, A. and W.J. Nelson, *Adherens and tight junctions: structure, function and connections to the actin cytoskeleton.* Biochim Biophys Acta, 2008. **1778**(3): p. 660-9.
17. Balda, M.S., et al., *Assembly of the tight junction: the role of diacylglycerol.* J Cell Biol, 1993. **123**(2): p. 293-302.
18. Aijaz, S., M.S. Balda, and K. Matter, *Tight junctions: molecular architecture and function.* Int Rev Cytol, 2006. **248**: p. 261-98.
19. Kohler, K. and A. Zahraoui, *Tight junction: a co-ordinator of cell signalling and membrane trafficking.* Biol Cell, 2005. **97**(8): p. 659-65.

20. Fanning, A.S., T.Y. Ma, and J.M. Anderson, *Isolation and functional characterization of the actin binding region in the tight junction protein ZO-1.* FASEB J, 2002. **16**(13): p. 1835-7.

21. Wittchen, E.S., J. Haskins, and B.R. Stevenson, *Exogenous expression of the amino-terminal half of the tight junction protein ZO-3 perturbs junctional complex assembly.* J Cell Biol, 2000. **151**(4): p. 825-36.

22. Fanning, A.S., et al., *The tight junction protein ZO-1 establishes a link between the transmembrane protein occludin and the actin cytoskeleton.* J Biol Chem., 1998. **273**(45): p. 29745-53.

23. Wolburg, H. and A. Lippoldt, *Tight junctions of the blood-brain barrier: development, composition and regulation.* Vascul Pharmacol, 2002. **38**(6): p. 323-37.

24. Lippoldt, A., et al., *Phorbol ester induced changes in tight and adherens junctions in the choroid plexus epithelium and in the ependyma.* Brain Res, 2000. **854**(1-2): p. 197-206.

25. Kemler, R., *From cadherins to catenins: cytoplasmic protein interactions and regulation of cell adhesion.* Trends Genet, 1993. **9**(9): p. 317-21.

26. Yarong, H., et al., *Cell-Culture Models of the Blood-Brain Barrier.* Stroke, 2014. **45**: p. 2515-2526.

27. Eigenmann, D.E., et al., *Comparative study of four immortalized human brain capillary endothelial cell lines, hCMEC/D3, hBMEC, TY10, and BB19, and optimization of culture conditions, for an in vitro blood-brain barrier model for drug permeability studies.* Fluids Barriers CNS, 2013. **10**(1): p. 33.

28. Persidsky, Y., et al., *A model for monocyte migration through the blood-brain barrier during HIV-1 encephalitis.* J Immunol, 1997. **158**(7): p. 3499-510.

29. Zheng, W. and Q. Zhao, *Establishment and characterization of an immortalized Z310 choroidal epithelial cell line from murine choroid plexus.* Brain Res, 2002. **958**(2): p. 371-80.

30. Schroten, M., et al., *A novel porcine in vitro model of the blood-cerebrospinal fluid barrier with strong barrier function.* PLoS One, 2012. **7**(6): p. e39835.

31. Schwerk, C., et al., *Polar invasion and translocation of Neisseria meningitidis and Streptococcus suis in a novel human model of the blood-cerebrospinal fluid barrier.* PLoS One, 2012. **7**(1): p. e30069.

32. Tenenbaum, T., et al., *Polar bacterial invasion and translocation of Streptococcus suis across the blood-cerebrospinal fluid barrier in vitro.* Cell Microbiol, 2009. **11**(2): p. 323-36.

33. Steinmann, U., et al., *Transmigration of polymorphnuclear neutrophils and monocytes through the human blood-cerebrospinal fluid barrier after bacterial infection in vitro.* J Neuroinflammation, 2013. **10**: p. 31.

34. Borkowski, J., et al., *Neisseria meningitidis elicits a pro-inflammatory response involving IkappaBzeta in a human blood-cerebrospinal fluid barrier model.* J Neuroinflammation, 2014. **11**: p. 163.

35. Dinner, S., et al., *Mitogen-activated protein kinases are required for effective infection of human choroid plexus epithelial cells by Listeria monocytogenes.* Microbes Infect, 2017. **19**(1): p. 18-33.

36. Schneider, H., et al., *Chemotaxis of T-cells after infection of human choroid plexus papilloma cells with Echovirus 30 in an in vitro model of the blood-cerebrospinal fluid barrier.* Virus Res, 2012. **170**(1-2): p. 66-74.

37. Dahm, T., et al., *Sequential transmigration of polymorphonuclear cells and naive CD3+ T lymphocytes across the blood-cerebrospinal-fluid barrier in vitro following infection with Echovirus 30.* Virus Res, 2017. **232**: p. 54-62.

38. Kim, K.S., *Mechanisms of microbial traversal of the blood-brain barrier.* Nat Rev Microbiol, 2008. **6**(8): p. 625-34.

39. Michos, A.G., et al., *Aseptic meningitis in children: analysis of 506 cases.* PLoS One, 2007. **2**(7): p. e674.

40. Rotbart, H.A., *Viral meningitis.* Semin Neurol, 2000. **20**(3): p. 277-92.

41. Romero, J.R., *Diagnosis and Management of Enteroviral Infections of the Central Nervous System.* Curr Infect Dis Rep, 2002. **4**(4): p. 309-316.

42. Ooi, M.H., et al., *Human enterovirus 71 disease in Sarawak, Malaysia: a prospective clinical, virological, and molecular epidemiological study.* Clin Infect Dis, 2007. **44**(5): p. 646-56.

43. Rudolph, H., H. Schroten, and T. Tenenbaum, *Enterovirus Infections of the Central Nervous System in Children: An Update.* Pediatr Infect Dis J, 2016. **35**(5): p. 567-9.

44. Rantakallio, P., M. Leskinen, and L. von Wendt, *Incidence and prognosis of central nervous system infections in a birth cohort of 12,000 children.* Scand J Infect Dis, 1986. **18**(4): p. 287-94.

45. Pons-Salort, M., E.P. Parker, and N.C. Grassly, *The epidemiology of non-polio enteroviruses: recent advances and outstanding questions.* Curr Opin Infect Dis, 2015. **28**(5): p. 479-87.

46. Palacios, G., et al., *Molecular epidemiology of echovirus 30: temporal circulation and prevalence of single lineages.* J Virol, 2002. **76**(10): p. 4940-9.

47. Lugo, D. and P. Krogstad, *Enteroviruses in the early 21st century: new manifestations and challenges.* Curr Opin Pediatr, 2016. **28**(1): p. 107-13.

48. Xiao, H., et al., *Molecular characterization of echovirus 30-associated outbreak of aseptic meningitis in Guangdong in 2012.* Virol J, 2013. **10**: p. 263.

49. Pinto Junior, V.L., et al., *Description of a widespread outbreak of aseptic meningitis due to echovirus 30 in Rio de Janeiro state, Brazil.* Braz J Infect Dis, 2009. **13**(5): p. 367-70.

50. van der Linden, L., K.C. Wolthers, and F.J. van Kuppeveld, *Replication and Inhibitors of Enteroviruses and Parechoviruses.* Viruses, 2015. **7**(8): p. 4529-62.

51. Baggen, J., et al., *Publisher Correction: The life cycle of non-polio enteroviruses and how to target it.* Nat Rev Microbiol, 2018. **16**(6): p. 391.

52. Baggen, J., et al., *The life cycle of non-polio enteroviruses and how to target it.* Nat Rev Microbiol, 2018. **16**(6): p. 368-381.

53. Khetsuriani, N., et al., *Enterovirus surveillance--United States, 1970-2005.* MMWR Surveill Summ, 2006. **55**(8): p. 1-20.

54. Allen, S.J., S.E. Crown, and T.M. Handel, *Chemokine: receptor structure, interactions, and antagonism.* Annu Rev Immunol, 2007. **25**: p. 787-820.

55. Hosking, M.P. and T.E. Lane, *The role of chemokines during viral infection of the CNS.* PLoS Pathog, 2010. **6**(7): p. e1000937.

56. Zlotnik, A. and O. Yoshie, *Chemokines: a new classification system and their role in immunity.* Immunity, 2000. **12**(2): p. 121-7.

57. Sulik, A., et al., *Increased levels of cytokines in cerebrospinal fluid of children with aseptic meningitis caused by mumps virus and echovirus 30.* Scand J Immunol, 2014. **79**(1): p. 68-72.

58. Bastos, M.S., et al., *Divergent cerebrospinal fluid cytokine network induced by non-viral and different viral infections on the central nervous system.* Bmc Infectious Diseases, 2015. **15**: p. 345.

59. Wang, S.M., H.Y. Lei, and C.C. Liu, *Cytokine immunopathogenesis of enterovirus 71 brain stem encephalitis.* Clin Dev Immunol, 2012. **2012**: p. 876241.

60. Kothur, K., et al., *CSF cytokines/chemokines as biomarkers in neuroinflammatory CNS disorders: A systematic review.* Cytokine, 2015.

61. Frei K, M.U., Leist TP, Zinkernagel RM, Schwab ME, Fontana A, *On the cellular surface and function of interleukin-6 produced in the central nervous system in viral diseases.* European journal of Immunology, 1989. **19**: p. 689-694.

62. Christensen, J.E., et al., *Fulminant lymphocytic choriomeningitis virus-induced inflammation of the CNS involves a cytokine-chemokine-cytokine-chemokine cascade.* J Immunol, 2009. **182**(2): p. 1079-87.

63. Durrant, D.M., B.P. Daniels, and R.S. Klein, *IL-1R1 signaling regulates CXCL12-mediated T cell localization and fate within the central nervous system during West Nile Virus encephalitis.* J Immunol, 2014. **193**(8): p. 4095-106.

64. McCandless, E.E., et al., *CXCR4 antagonism increases T cell trafficking in the central nervous system and improves survival from West Nile virus encephalitis.* Proc Natl Acad Sci U S A, 2008. **105**(32): p. 11270-5.

65. McCandless, E.E., et al., *CXCL12 limits inflammation by localizing mononuclear infiltrates to the perivascular space during experimental autoimmune encephalomyelitis.* J Immunol, 2006. **177**(11): p. 8053-64.

66. Kaul, M., G.A. Garden, and S.A. Lipton, *Pathways to neuronal injury and apoptosis in HIV-associated dementia.* Nature, 2001. **410**(6831): p. 988-94.

67. Sato, M., et al., *Cytokine and cellular inflammatory sequence in enteroviral meningitis.* Pediatrics, 2003. **112**(5): p. 1103-7.

68. Wang, S.M., et al., *Acute chemokine response in the blood and cerebrospinal fluid of children with enterovirus 71-associated brainstem encephalitis.* J Infect Dis, 2008. **198**(7): p. 1002-6.

69. Fukushima, K., A. Ishiguro, and T. Shimbo, *Transient elevation of granulocyte colony-stimulating factor levels in cerebrospinal fluid at the initial stage of aseptic meningitis in children.* Pediatr Res, 1995. **37**(2): p. 160-4.

70. Bardina, S.V., et al., *Differential Roles of Chemokines CCL2 and CCL7 in Monocytosis and Leukocyte Migration during West Nile Virus Infection.* J Immunol, 2015. **195**(9): p. 4306-18.

71. Tabor-Godwin, J.M., et al., *A novel population of myeloid cells responding to coxsackievirus infection assists in the dissemination of virus within the neonatal CNS.* J Neurosci, 2010. **30**(25): p. 8676-91.

72. Rhoades, R.E., et al., *Enterovirus infections of the central nervous system.* Virology, 2011. **411**(2): p. 288-305.

73. Thoelen, I., et al., *Molecular typing and epidemiology of enteroviruses identified from an outbreak of aseptic meningitis in Belgium during the summer of 2000.* J Med Virol, 2003. **70**(3): p. 420-9.

74. Ishiwata, I., et al., *Establishment and characterization of a human malignant choroids plexus papilloma cell line (HIBCPP).* Hum Cell, 2005. **18**(1): p. 67-72.

75. Plager, H. and W. Decher, *A newly-recognized enterovirus isolated from cases of aseptic meningitis.* Am J Hyg, 1963. **77**: p. 26-8.

76. Spandidos, A., et al., *PrimerBank: a resource of human and mouse PCR primer pairs for gene expression detection and quantification.* Nucleic Acids Res, 2010. **38**(Database issue): p. D792-9.

77. Tsubaki, T., et al., *Accumulation of plasma cells expressing CXCR3 in the synovial sublining regions of early rheumatoid arthritis in association with production of Mig/CXCL9 by synovial fibroblasts.* Clin Exp Immunol, 2005. **141**(2): p. 363-71.

78. Dahm, T., et al., *Strain-dependent effects of clinical echovirus 30 outbreak isolates at the blood-CSF barrier.* J Neuroinflammation, 2018. **15**(1): p. 50.

79. Dinner, S., et al., *A Choroid Plexus Epithelial Cell-based Model of the Human Blood-Cerebrospinal Fluid Barrier to Study Bacterial Infection from the Basolateral Side.* J Vis Exp, 2016(111).

80. Neurauter, A., et al., *Cell isolation and expansion using Dynabeads.* Adv Biochem Eng Biotechnol., 2007. **106**: p. 41-73.

81. Lin, Z., et al., *In vivo antigen-driven plasmablast enrichment in combination with antigen-specific cell sorting to facilitate the isolation of rare monoclonal antibodies from human B cells.* Nat Protoc, 2014. **9**(7): p. 1563-77.

82. Lowry, O.H., et al., *Protein measurement with the Folin phenol reagent.* J Biol Chem, 1951. **193**(1): p. 265-75.

83. Millipore, M., *The Power of Biomarker Analysis Multiplex assay tips from the makers of MILLIPLEX MAP*, M. Millipore, Editor. 2014.

84. Leirisalo-Repo, M., *The present knowledge of the inflammatory process and the inflammatory mediators.* Pharmacol Toxicol, 1994. **75 Suppl 2**: p. 1-3.

85. Bleau, C., et al., *Brain Invasion by Mouse Hepatitis Virus Depends on Impairment of Tight Junctions and Beta Interferon Production in Brain Microvascular Endothelial Cells.* J Virol, 2015. **89**(19): p. 9896-908.

86. Volle, R., et al., *Differential permissivity of human cerebrovascular endothelial cells to enterovirus infection and specificities of serotype EV-A71 in crossing an in vitro model of the human blood-brain barrier.* J Gen Virol, 2015. **96**(Pt 7): p. 1682-95.

87. Riabi, S., et al., *Study of Coxsackie B viruses interactions with Coxsackie Adenovirus receptor and Decay-Accelerating Factor using Human CaCo-2 cell line.* J Biomed Sci, 2014. **21**: p. 50.

88. Bergelson, J.M., et al., *Isolation of a common receptor for Coxsackie B viruses and adenoviruses 2 and 5.* Science, 1997. **275**(5304): p. 1320-3.

89. Bergelson, J.M., et al., *Decay-accelerating factor (CD55), a glycosylphosphatidylinositol-anchored complement regulatory protein, is a receptor for several echoviruses.* Proc Natl Acad Sci U S A, 1994. **91**(13): p. 6245-8.

90. Cohen, C.J., et al., *The coxsackievirus and adenovirus receptor is a transmembrane component of the tight junction.* Proc Natl Acad Sci U S A, 2011. **98**(26): p. 15191-6.

91. Coyne, C.B. and J.M. Bergelson, *Virus-induced Abl and Fyn kinase signals permit coxsackievirus entry through epithelial tight junctions.* Cell, 2006. **124**(1): p. 119-31.

92. Van Itallie, C.M., et al., *ZO-1 stabilizes the tight junction solute barrier through coupling to the perijunctional cytoskeleton.* Mol Biol Cell, 2009. **20**(17): p. 3930-40.

93. Yu, D., et al., *MLCK-dependent exchange and actin binding region-dependent anchoring of ZO-1 regulate tight junction barrier function.* Proc Natl Acad Sci U S A, 2010. **107**(18): p. 8237-41.

94. Tan, S., et al., *HIV-1 impairs human retinal pigment epithelial barrier function: possible association with the pathogenesis of HIV-associated retinopathy.* Lab Invest, 2014. **94**(7): p. 777-87.

95. Man, Y., et al., *Loss of epithelial integrity resulting from E-cadherin dysfunction predisposes airway epithelial cells to adenoviral infection.* Am J Respir Cell Mol Biol, 2000. **23**(5): p. 610-7.

96. Tenenbaum, T., et al., *Dexamethasone prevents alteration of tight junction-associated proteins and barrier function in porcine choroid plexus epithelial cells after infection with Streptococcus suis in vitro.* Brain Res, 2008. **1229**: p. 1-17.

97. Haseloff, R.F., et al., *Transmembrane proteins of the tight junctions at the blood-brain barrier: structural and functional aspects.* Semin Cell Dev Biol, 2015. **38**: p. 16-25.

98. Dando, S.J., et al., *Pathogens penetrating the central nervous system: infection pathways and the cellular and molecular mechanisms of invasion.* Clin Microbiol Rev, 2014. **27**(4): p. 691-726.

99. Delorme-Axford, E. and C.B. Coyne, *The actin cytoskeleton as a barrier to virus infection of polarized epithelial cells.* Viruses, 2011. **3**(12): p. 2462-77.

100. Svensson, L., et al., *Symmetric infection of rotavirus on polarized human intestinal epithelial (Caco-2) cells.* J Virol, 1991. **65**(8): p. 4190-7.

101. Tiwari, V., et al., *Role for nectin-1 in herpes simplex virus 1 entry and spread in human retinal pigment epithelial cells.* FEBS J, 2008. **275**(21): p. 5272-85.

102. Bruce, E.A., P. Digard, and A.D. Stuart, *The Rab11 pathway is required for influenza A virus budding and filament formation.* J Virol, 2010. **84**(12): p. 5848-59.

103. Lakadamyali, M., et al., *Visualizing infection of individual influenza viruses.* Proc Natl Acad Sci U S A, 2003. **100**(16): p. 9280-5.

104. Obert, G., I. Peiffer, and A.L. Servin, *Rotavirus-induced structural and functional alterations in tight junctions of polarized intestinal Caco-2 cell monolayers.* J Virol, 2000. **74**(10): p. 4645-51.

105. Savarin, C., et al., *Monocytes regulate T cell migration through the glia limitans during acute viral encephalitis.* J Virol, 2010. **84**(10): p. 4878-88.

106. Guyon, A., *CXCL12 chemokine and its receptors as major players in the interactions between immune and nervous systems.* Front Cell Neurosci, 2014. **8**: p. 65.

107. Ransohoff, R.M. and B. Engelhardt, *The anatomical and cellular basis of immune surveillance in the central nervous system.* Nat Rev Immunol, 2012. **12**(9): p. 623-35.

108. Man, S., et al., *CXCL12-induced monocyte-endothelial interactions promote lymphocyte transmigration across an in vitro blood-brain barrier.* Sci Transl Med, 2012. **4**(119): p. 119ra14.

109. Muller, W.A., *Transendothelial migration: unifying principles from the endothelial perspective.* Immunol Rev, 2016. **273**(1): p. 61-75.

110. Winger, R.C., J.E. Koblinski, and W.A. Muller, *Pathway of leukocyte transendothelial migration across an in vitro human blood brain barrier model.* Faseb Journal, 2013. **27**(1).

111. Abadier, M., et al., *Cell surface levels of endothelial ICAM-1 influence the transcellular or paracellular T-cell diapedesis across the blood-brain barrier.* Eur J Immunol, 2015. **45**(4): p. 1043-58.

112. Yang, L., et al., *ICAM-1 regulates neutrophil adhesion and transcellular migration of TNF-alpha-activated vascular endothelium under flow.* Blood, 2005. **106**(2): p. 584-92.

113. Martinelli, R., et al., *Probing the biomechanical contribution of the endothelium to lymphocyte migration: diapedesis by the path of least resistance.* J Cell Sci, 2014. **127**(Pt 17): p. 3720-34.

114. Mamdouh, Z., A. Mikhailov, and W.A. Muller, *Transcellular migration of leukocytes is mediated by the endothelial lateral border recycling compartment.* J Exp Med, 2009. **206**(12): p. 2795-808.

115. Kolaczkowska, E. and P. Kubes, *Neutrophil recruitment and function in health and inflammation.* Nat Rev Immunol, 2013. **13**(3): p. 159-75.

116. Borregaard, N., *Neutrophils, from marrow to microbes.* Immunity, 2010. **33**(5): p. 657-70.

117. Wewer, C., et al., *Transcellular migration of neutrophil granulocytes through the blood-cerebrospinal fluid barrier after infection with Streptococcus suis.* J Neuroinflammation, 2011. **8**: p. 51.

118. Lin, T.Y., et al., *Different proinflammatory reactions in fatal and non-fatal enterovirus 71 infections: implications for early recognition and therapy.* Acta Paediatr, 2002. **91**(6): p. 632-5.

119. Wang, S.M., et al., *Pathogenesis of enterovirus 71 brainstem encephalitis in pediatric patients: roles of cytokines and cellular immune activation in patients with pulmonary edema.* J Infect Dis, 2003. **188**(4): p. 564-70.

120. Wang, S.M., et al., *Cerebrospinal fluid cytokines in enterovirus 71 brain stem encephalitis and echovirus meningitis infections of varying severity.* Clin Microbiol Infect, 2007. **13**(7): p. 677-82.

121. Weng, K.F., et al., *Neural pathogenesis of enterovirus 71 infection.* Microbes Infect, 2010. **12**(7): p. 505-10.

122. Reboldi, A., et al., *C-C chemokine receptor 6-regulated entry of TH-17 cells into the CNS through the choroid plexus is required for the initiation of EAE.* Nat Immunol, 2009. **10**(5): p. 514-23.

123. Cavčić A, et al., *Concentration gradient of CXCL10 and CXCL11 between the cerebrospinal fluid and plasma in children with enteroviral aseptic meningitis.* Eur J Paediatr Neurol, 2011. **6**: p. 502-7.

124. Capitini, C.M., A.A. Chisti, and C.L. Mackall, *Modulating T-cell homeostasis with IL-7: preclinical and clinical studies.* J Intern Med, 2009. **266**(2): p. 141-53.

125. Schwartz, M. and K. Baruch, *The resolution of neuroinflammation in neurodegeneration: leukocyte recruitment via the choroid plexus.* EMBO J, 2014. **33**(1): p. 7-22.

126. Roe, K., et al., *West Nile virus-induced disruption of the blood-brain barrier in mice is characterized by the degradation of the junctional complex proteins and increase in multiple matrix metalloproteinases.* J Gen Virol, 2012. **93**(Pt 6): p. 1193-203.

127. Moser, L.A., M. Carter, and S. Schultz-Cherry, *Astrovirus increases epithelial barrier permeability independently of viral replication.* J Virol, 2007. **81**(21): p. 11937-45.

128. Nazli, A., et al., *Exposure to HIV-1 directly impairs mucosal epithelial barrier integrity allowing microbial translocation.* PLoS Pathog, 2010. **6**(4): p. e1000852.

129. Casas, N. and E. Sunen, *Detection of enteroviruses, hepatitis A virus and rotaviruses in sewage by means of an immunomagnetic capture reverse transcription-PCR assay.* Microbiol Res, 2002. **157**(3): p. 169-75.

130. Molet, L., et al., *Enterovirus infections in hospitals of Ile de France region over 2013.* J Clin Virol, 2016. **74**: p. 37-42.

131. Bailly, J.L., et al., *Genetic diversity of echovirus 30 during a meningitis outbreak, demonstrated by direct molecular typing from cerebrospinal fluid.* J Med Virol, 2002. **68**(4): p. 558-67.

132. Tryfonos, C., et al., *Molecular typing and epidemiology of enteroviruses in Cyprus, 2003-2007.* J Med Microbiol, 2011. **60**(Pt 10): p. 1433-40.

133. Oberste, M.S., et al., *Molecular epidemiology and genetic diversity of echovirus type 30 (E30): genotypes correlate with temporal dynamics of E30 isolation.* J Clin Microbiol, 1999. **37**(12): p. 3928-33.

134. Muckelbauer, J.K. and M.G. Rossmann, *The structure of coxsackievirus B3.* Curr Top Microbiol Immunol, 1997. **223**: p. 191-208.

135. Pan, J., et al., *Specificity of coxsackievirus B3 interaction with human, but not murine, decay-accelerating factor: replacement of a single residue within short consensus repeat 2 prevents virus attachment.* J Virol, 2015. **89**(2): p. 1324-8.

136. Pan, J., et al., *Single amino acid changes in the virus capsid permit coxsackievirus B3 to bind decay-accelerating factor.* J Virol, 2011. **85**(14): p. 7436-43.

137. Smura, T., et al., *Enterovirus strain and type-specific differences in growth kinetics and virus-induced cell destruction in human pancreatic duct epithelial HPDE cells.* Virus Res, 2015. **210**: p. 188-97.

11. Acknowledgments

For the opportunity and support during this research I would like to thank

- Prof. Dr. med. Horst Schroten for the provision of the dissertation topic and the support in the preparation of this thesis.
- Prof. Dr. Hans- Georg Kräusslich to act as a first examiner.
- Prof. Dr. Tobias Tenenbaum and PD Dr. Henriette Rudolph for the support and guidance. Your dedication, ambition and love for science have taught me many valuable lessons for my future.
- Prof. Dr. Christian Schwerk for in depth discussions and perspective on what it takes to be a good scientist.
- Carolin for teaching me everything in the laboratory, providing a helpful hand and always being a shoulder to lean on when things got difficult.
- All my colleagues in the laboratory and especially Julia, Steffi, Marie, Franziska and Alexa for making these years fun. Late nights, fun lunch breaks and above all early mornings were much more exciting and pleasant with such a great team.
- My loving partner Jennie. Without you, your positive energy and your non-stop support, I doubt I would have gone through with the work and finished the dissertation.
- My parents and my brother for believing in me and supporting my choices from the moment I decided to start my B.Sc in England to going to Mannheim to pursue a PhD.
- And last but not least my close friends Fabian and Dennis for being there and helping with everything outside of the scientific world.